NAVAL POSTGRADUATE SCHOOL

MONTEREY, CALIFORNIA

THESIS

CHARACTERIZING THE EFFECTS OF CONVECTION ON THE AFTERNOON-TO-EVENING BOUNDARY LAYER TRANSITION DURING PECAN 2015

by

Geoffry R. Eberle

December 2016

Thesis Advisor: Qing Wang
Second Reader: Wendell Nuss

Approved for public release. Distribution is unlimited.

THIS PAGE INTENTIONALLY LEFT BLANK

REPORT DOCUMENTATION PAGE			*Form Approved OMB No. 0704–0188*

Public reporting burden for this collection of information is estimated to average 1 hour per response, including the time for reviewing instruction, searching existing data sources, gathering and maintaining the data needed, and completing and reviewing the collection of information. Send comments regarding this burden estimate or any other aspect of this collection of information, including suggestions for reducing this burden, to Washington headquarters Services, Directorate for Information Operations and Reports, 1215 Jefferson Davis Highway, Suite 1204, Arlington, VA 22202-4302, and to the Office of Management and Budget, Paperwork Reduction Project (0704-0188) Washington, DC 20503.

1. AGENCY USE ONLY *(Leave blank)*	2. REPORT DATE December 2016	3. REPORT TYPE AND DATES COVERED Master's thesis	
4. TITLE AND SUBTITLE CHARACTERIZING THE EFFECTS OF CONVECTION ON THE AFTERNOON-TO-EVENING BOUNDARY LAYER TRANSITION DURING PECAN 2015			5. FUNDING NUMBERS
6. AUTHOR(S) Geoffry R. Eberle			
7. PERFORMING ORGANIZATION NAME(S) AND ADDRESS(ES) Naval Postgraduate School Monterey, CA 93943-5000			8. PERFORMING ORGANIZATION REPORT NUMBER
9. SPONSORING /MONITORING AGENCY NAME(S) AND ADDRESS(ES) N/A			10. SPONSORING / MONITORING AGENCY REPORT NUMBER
11. SUPPLEMENTARY NOTES The views expressed in this thesis are those of the author and do not reflect the official policy or position of the Department of Defense or the U.S. Government. IRB number: N/A			
12a. DISTRIBUTION / AVAILABILITY STATEMENT Approved for public release. Distribution is unlimited.		12b. DISTRIBUTION CODE	

13. ABSTRACT (maximum 200 words)

The Great Plains exhibits a widely known characteristic transition in the atmospheric boundary layer, from a daytime unstable boundary layer to a nocturnal stable boundary layer near sunset. There remains much to learn about this process through observational data. Impacts of convective weather prior to and during this transitional period is one of the lesser understood subjects. During the Plains Elevated Convection at Night (PECAN) field campaign from June 1 to July 15, 2015, extensive measurements of near surface thermodynamic variables, wind speed and direction, turbulence and scalar perturbations were made outside the city of Greensburg, Kansas. These measurements were made on three towers: a 16-m flux tower, 6-m flux tripod, and a 3-m scaler tripod, giving 17 levels of measurement from 25 cm below the surface to 16 m above. To supplement the tower-based measurements, a Leosphere Doppler LIDAR and a sonic detection and ranging (SODAR) device were used to obtain vertical profiles of mean wind and turbulence up to approximately 250 m and 6000 m, respectively. The primary focus of this thesis is to characterize the transitional period with the presence of convective events. This thesis also used the observed surface fluxes to evaluate the fluxes calculated from the bulk parameterization scheme. The surface layer stability functions in the Coupled Air Ocean Response Experiment (COARE) surface flux algorithm will be used. The surface roughness used in the Navy's Coupled Ocean/Atmosphere Mesoscale Prediction System (COAMPS) model will also be examined.

14. SUBJECT TERMS boundary layer transition afternoon-to-evening transition, field campaign PECAN 2015 convective boundary layer decay, multi-platform surface fluxes COARE COAMPS			15. NUMBER OF PAGES 107
			16. PRICE CODE
17. SECURITY CLASSIFICATION OF REPORT Unclassified	18. SECURITY CLASSIFICATION OF THIS PAGE Unclassified	19. SECURITY CLASSIFICATION OF ABSTRACT Unclassified	20. LIMITATION OF ABSTRACT UU

THIS PAGE INTENTIONALLY LEFT BLANK

CHARACTERIZING THE EFFECTS OF CONVECTION ON THE AFTERNOON-TO-EVENING BOUNDARY LAYER TRANSITION DURING PECAN 2015

Geoffry R. Eberle
Lieutenant, United States Navy
B.S., Western Illinois University, 2009

Submitted in partial fulfillment of the
requirements for the degree of

MASTER OF SCIENCE IN METEOROLOGY AND PHYSICAL OCEANOGRAPHY

from the

NAVAL POSTGRADUATE SCHOOL
December 2016

Approved by: Dr. Qing Wang
                   Thesis Advisor

                   Dr. Wendell Nuss
                   Second Reader

                   Dr. Wendell Nuss
                   Chair, Department of Meteorology

THIS PAGE INTENTIONALLY LEFT BLANK

ABSTRACT

The Great Plains exhibits a widely known characteristic transition in the atmospheric boundary layer, from a daytime unstable boundary layer to a nocturnal stable boundary layer near sunset. There remains much to learn about this process through observational data. Impacts of convective weather prior to and during this transitional period is one of the lesser understood subjects. During the Plains Elevated Convection at Night (PECAN) field campaign from June 1 to July 15, 2015, extensive measurements of near surface thermodynamic variables, wind speed and direction, turbulence and scalar perturbations were made outside the city of Greensburg, Kansas. These measurements were made on three towers: a 16-m flux tower, 6-m flux tripod, and a 3-m scaler tripod, giving 17 levels of measurement from 25 cm below the surface to 16 m above. To supplement the tower-based measurements, a Leosphere Doppler LIDAR and a sonic detection and ranging (SODAR) device were used to obtain vertical profiles of mean wind and turbulence up to approximately 250 m and 6000 m, respectively. The primary focus of this thesis is to characterize the transitional period with the presence of convective events. This thesis also used the observed surface fluxes to evaluate the fluxes calculated from the bulk parameterization scheme. The surface layer stability functions in the Coupled Air Ocean Response Experiment (COARE) surface flux algorithm will be used. The surface roughness used in the Navy's Coupled Ocean/Atmosphere Mesoscale Prediction System (COAMPS) model will also be examined.

THIS PAGE INTENTIONALLY LEFT BLANK

TABLE OF CONTENTS

THIS PAGE INTENTIONALLY LEFT BLANK

LIST OF FIGURES

THIS PAGE INTENTIONALLY LEFT BLANK

LIST OF TABLES

THIS PAGE INTENTIONALLY LEFT BLANK

LIST OF ACRONYMS AND ABBREVIATIONS

ABL	atmospheric boundary layer
AET	afternoon-to-evening transition
BLLAST	boundary layer late afternoon and sunset turbulence
CBL	convective boundary layer
COAMPS	coupled ocean/atmospheric mesoscale prediction system
COARE	coupled ocean air response experiment
EET	early evening transition
EM	electromagnetic
EO	electro-optical
FP2	fixed PISA sight #2
LHF	latent heat flux
LIDAR	light detection and ranging device
LLJ	low-level jet
MF	momentum flux
PECAN	plains elevated convection at night
PISA	PECAN integrated sounding array
SHF	sensible heat flux
SODAR	sonic detection and ranging device
TDA	tactical decision aid
TKE	turbulent kinetic energy
UMBC	University of Maryland, Baltimore County

THIS PAGE INTENTIONALLY LEFT BLANK

ACKNOWLEDGMENTS

THIS PAGE INTENTIONALLY LEFT BLANK

I.   INTRODUCTION

The atmospheric boundary layer (ABL) overland undergoes substantial diurnal variations with a nocturnal stable boundary layer transitioning to a well-developed daytime convective boundary layer after sunrise, as the surface heating generates significant turbulence mixing. The daytime boundary layer is dominated by thermally buoyant eddies, resulting from sensible and latent heat fluxes. There is a similar transition in the afternoon, when the convectively unstable boundary layer transitions to the stable nocturnal boundary layer (Stull 1988; Garratt 1992). The stable boundary layer is much shallower and typically topped by a low-level jet. This cycle is illustrated in Figure 1. The boundary layer afternoon-to-evening transition is referred to as AET. This transition has been the focal point of recent research in an attempt to characterize the physical processes occurring during this transition. It was found that the AET is best observed under clear skies and light winds (Acevedo and Fitzjarrald 2001). These conditions allow for maximum radiative cooling at the surface. Various AET signatures have been observed and often occur in an inconsistent order and can vary in time of occurrence, location and by day. The surface characteristics have been well documented by Bonin (2013), Grimsdell and Angevine (2002), Acevedo and Fitzjarrald (2001), Bodine et al. (2009), Lothon et al. (2014) and Wingo and Knupp (2014), which will be discussed in the next chapter.
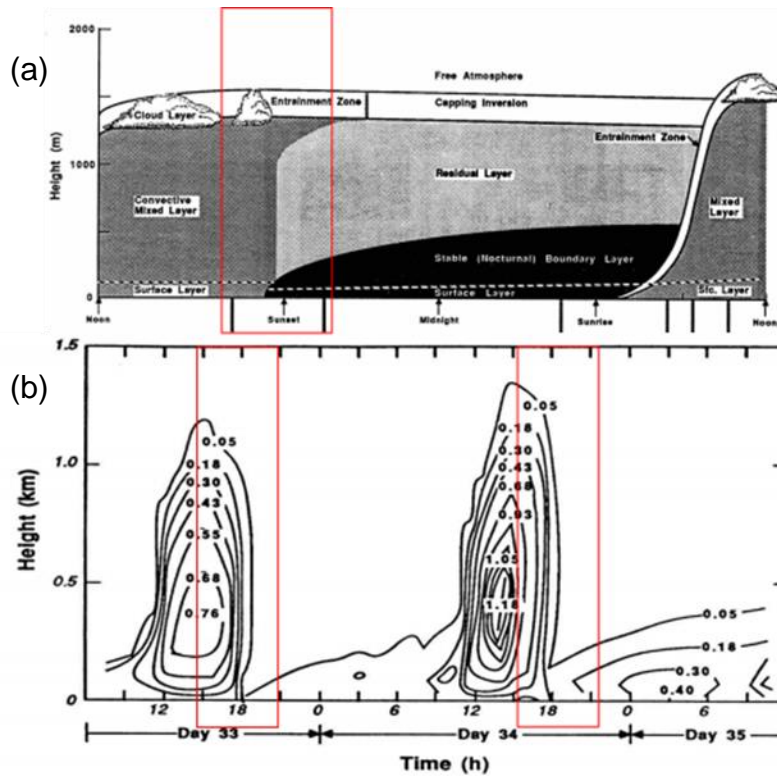
(a) Boundary layer diurnal evolution; (b) Modeled TKE in m^2 s^(-2). The transitional periods of interests to this study are highlighted in red.

Figure 1. Boundary Layer Evolution and TKE. Adapted from Stull (1988).

Convective storms occur quite frequently in the late afternoon to the early evenings over many moisture-rich regions of the world. Such deep convective activities result in significant changes to the entire column of the atmosphere, including the boundary layer, the surface, and the subsurface due to strong vertical mixing, cloud coverage, and most importantly, heavy precipitations (Kessler 1983; Boutle et al. 2009). Undoubtedly, the occurrence of deep convection may change the surface layer energy balance and turbulent mixing. If such convection occurs during the normal time frame of transition from convective boundary layer to stable boundary layer, i.e., AET, it may introduce "abnormal" variability to the atmospheric state variable and surface properties and hence, change the transition processes. This effect of convection on the transitional period is much less understood, and will be the focus of this thesis.

The data used for these analyses was obtained during a large-scale, multi institution field campaign known as Plains Elevated Convection at Night (PECAN). The effects that clouds, precipitation, wind events and any combination of these factors, have on the transition is investigated in an attempt to characterize common features between the convective events and how these features differ from non-convective transitional events. The impact of the convective events on AET will be clear from such comparisons.

Bettering our understanding of the AET during both calm and convectively disturbed events is critical to military operations. The atmospheric boundary layers play a critical role modifying the propagation path and intensity of electromagnetic (EM) and electro-optical (EO) energy. A common phenomenon for the EM frequency is ducting, while for EO energy is scintillation. The boundary layer vertical profiles of temperature/humidity can lead to greatly extended or very limited ranges for communication or radar systems. Boundary layer turbulence also impacts the effectiveness of directed energy weapons and image detection. For all these atmospheric effects on EM/EO propagation, the impact of a stable boundary layer is substantially different from that of the convective boundary layers. It is thus important to identify the characteristics of the change in boundary layer regimes. By increasing our understanding of the transitional period and how it is affected by convection, rain and clouds, better parameterizations and processes can be built into the forecast models and tactical decision aids. The results will yield better prediction and potentially tactical exploitation of the atmosphere, leading to increased radar detection and communication ranges.

Another practical application of this thesis is the evaluation of the surface flux parametrization schemes specifically with the Navy's Coupled Ocean/Atmospheric Mesoscale Prediction System (COAMPS). Currently COAMPS uses a bulk parametrization scheme known as Coupled Ocean Air Response Experiment (COARE) v3.0 to parametrize the surface fluxes within the boundary layer. COAMPS plays a vital role in initializing the tactical decision

aides (TDA) used across the fleet. By comparing observed fluxes with those that COARE produces, improvements can be made to make this algorithm a more accurate representation of the physical environment

This thesis is structured as follows; in Chapter II, a summary of previous work on the AET is provided, including a clear definition of the transition period and procedures to identify convective events. In Chapter III, the experiment setup and instrumentation relevant to this thesis work will be discussed. Chapter IV contains a discussion of the methods employed to process and analyze the data as well as results and discussion. Summary and conclusions will be presented in Chapter V.

II.   BACKGROUND LITERATURE REVIEW AND DEFINITIONS

A.   PREVIOUS RESEARCH ON AET

The planetary boundary layer has a transitional period in the afternoon, from the fully developed, well-mixed, convective boundary layer to the nocturnal, stably stratified boundary layer. This transition has been defined by different ways in the research. Wingo and Knupp (2014) defined this transitional period as "3 hours prior to and 2 hours after sunset" based on using a sunset relative timeframe to examine the AET signature. Busse and Knupp (2012) use a convention that was previously used by Caughey et al. (1979) and several others (e.g., Grant 1997, Mahrt 1981, and Beare et al. 2006) that defined this transitional period as "the onset of negative surface heat flux." This definition is based on the idea that once the surface heat flux has become negative, the stable surface layer has started to develop, and other processes such as radiation, advection and wind shear become more important to the decay of turbulence and the stabilization of the boundary layer.

Previous studies have characterized this transition in a couple different ways. Acevedo and Fitzjarrald (2001) defined the AET (their work used the term EET) as "under clear skies, surface state variables (temperature, specific humidity 'q', and mean wind) often exhibit larger variations in the first 1 to 2 hours after sunset than during the rest of the night. This period of enhanced changes at the surface is the early evening transition (EET) and results from the decay of turbulent activity." In Acevedo and Fitzjarrald's study, three categories of the transition were defined: transition nights, non-transition nights, and partial transition nights. Acevedo and Fitzjarrald also noted that the transition occurred "when large-scale subsidence keeps skies clear and weak winds prevail," which allows for radiative cooling and turbulence to decay. They also noted that the presence of the cloud layers reduced radiative cooling and thus effected the transition. Acevedo and Fitzjarrald also determined that strong winds were also present on nights when transitions did not occur. The role of the strong wind was

to generate turbulence by wind shear to prevent the rapid decay of turbulence and thus inhibited the transition. The cloud and wind shear effects will be examined in more depth in this thesis, as these factors, with the addition of precipitation, are all associated with convective events. Previous research has led us to believe that a definitive transition will be affected by these factors.

Wingo and Knupp (2014) examined AET on nights with no clouds and characterized the evolution using a combination of a 915-MHz Doppler wind profiler (915DWP), a 12-channel microwave profiling radiometer (MPR), a Vaisala laser ceilometer, and a Doppler wind LIDAR. They found that the mean of velocity variance $(\overline{(U'^2)})$ and temperature showed a systematic decrease typically starting at 145 minutes before sunset with a shaper decline as sunset approached. By 30 minutes after sunset, the mean velocity variance remains relatively constant. Their study also showed a temperature inversion forming approximately 20 minutes prior to sunset indicated by the difference of mean temperature at 2 and 10 m (T_2-T_{10}).Wingo and Knupp noted specific signatures which include an abrupt decrease in turbulent quantities, combined with a decrease in wind speed, temperature variance and vertical temperature gradient (2014). One key result of this study was it was also determined that not all events displayed the same order of transition signatures and some signatures were not presented at all in some events. Figure 2 shows the evolution of the surface parameters, horizontal wind, temperature (at 2 and 10 meters) and vertical velocities, this study will compare results and determine the key differences between the evolution during a convectively disturbed boundary layer and the clear sky transition that Wingo and Knupp examined. My research looked to confirm these observations of AET on similar conditions as well as compare my results to the AET of convectively disturbed events.
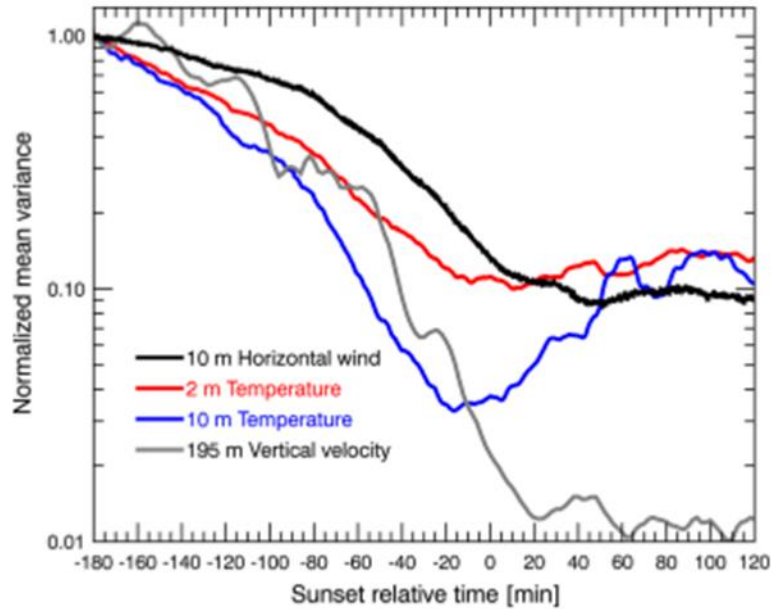
Each curve represents the mean value of all available cases, normalized by the value at 3 h prior to sunset. Surface data used the horizontal wind and both temperature curves from the 140 AET events, while the vertical velocity curve is comprised of the 30 cases with DWL observations. Figure and caption taken from Wingo and Knupp (2014).

Figure 2. Comparison of Normalized Variances on a Logarithmic Scale.

Grimsdell (2001) focused on characterizing the AET of the boundary layer by utilizing a 915 MHz profiler, laser ceilometer and surface meteorological station. Grimsdell also used radiosondes to obtain vertical profiles of temperature, specific humidity (q), wind speed and wind direction, launched at 1200 local standard time (LST) with additional launches at 0900, 1030 and 1330 LST on days when well-mixed boundary layers were expected to form. Sensible, latent and momentum fluxes were determined using a deployable flux portable automated mesonet (PAM) station from National Center of Atmospheric Research. Grimsdell (2001) found that "the decay of the convective boundary layer (CBL) during the afternoon failed to show a single characteristic shape." Instead, it was noted that there were a variety of patterns and shapes used to describe the decay of the CBL, and thus describe the AET. He also found that the start time for the transition varies each day.

7

The time at which the transition begins is generally assumed to be around an hour before sunset, but we found that start times could be much earlier. We estimated the time at which the transition began for each categorized day and found a wide range of start times, with the transition sometimes beginning early in the afternoon. (Grimsdell 2001)

Bonin (2013) examined the AET, referred to as early-evening transition (EET) in his paper, by using small unmanned aerial systems and mesonets to examine temperature, humidity, and pressure, as well as surface latent and sensible heat flux to characterize the transition. In this study, 5 days of data were determined to have observed the EET with 2 days selected for additional analysis. The first case had light winds and became progressively weaker throughout the evening. The conditions were ideal for a pronounced EET, evidenced by the sharp increase in moisture and decrease in temperature. The second case was similar to the first one, except that there was significant cool and moist air advection in place during the time of the flights (Bonin 2013).

From June 14 to July 8, 2011, a large field campaign took place in southern France to examine the AET. This campaign was called the Boundary-Layer Late Afternoon and Sunset Turbulence (BLLAST) and consisted of a large suite of instruments to include flux towers, tethered balloons, and meteorological stations. "The boundary layer, from the free earth's surface to the free troposphere, was probed during the day with intensive periods over the transition" (Lothon et al. 2014). During this field campaign the atmospheric boundary layer to include the transition, and the free atmosphere above were intensively sampled. One key point noted during this study is that during the "afternoon transition, the surface buoyancy flux decreases to zero, and the influence of other competing processes such as radiation, advection, entrainment, or wind shear become relatively more important" (Lothon et al. 2014). This study observed the transition and characterized different aspects of the boundary layer such as surface temperature and moisture, solar irradiance, sensible/latent heat fluxes, as well as TKE. It was noted that TKE decayed in two different regimes: an initial slow decay, followed by an abrupt decay of the

remaining TKE. These regimes were first introduced by Nadeau et al. (2011). It was also noted that the abrupt decay occurred when the surface flux decreased at a maximum rate (Lothon et al. 2014).

The COARE bulk parametrization scheme was first described in Fairall et al. (1996) and has become one of the most used parametrization schemes in the air-sea interaction community. This scheme was initially created in 1996 and is now updated to the third version. These updates include being able to handle higher wind speeds, increased global applicability, and improvements to the stability function built into the model (Fairall et al. 2003). Also improvements in the update relevant to this thesis include changing the latent heat flux to use vapor pressure as opposed to mixing ratio and changing the Von Karman constant to 0.4 (Fairall et al. 2003). In this thesis, we will use the COARE algorithm, modified to be used over land, to estimate surface fluxes from the mean measurements. The validity of the surface roughness length used in COAMPS for the site FP2 will be examined. The adequacy of the COARE scheme under the convective events to be discussed in this thesis will be examined as well.

B.   DEFINITIONS

As mentioned previously, this thesis will define the AET as 3 hours prior to and 2 hours after sunset, following Wingo and Knupp (2014). While it was noted in other work that this transition may occur earlier or later, it is generally agreed upon that the transition happens before sunset. Our data set includes the full day of measurements from the tower and tripod, as well as vertical profiles taken at regular intervals throughout the day. This data was supplemented with intensive vertical profiles of the lowest 200 meters measured with the tethersonde system. This study initially defined convective events as thunderstorm events that occurred within 30 miles of Greensburg, KS, before sunset. With these definitions, each case was divided into specific events to include cloud cover, precipitation, and a combination of these conditions. To determine cloud cover,

9

the ceilometer was utilized We only considered low clouds defined as those clouds with base heights lower than 1000 meters. To determine precipitation events at FP2, the measurements from the Vaisala WT on the 16-m tower was used. This data was available after June 14, 2016. If a convective event occurred after sunset, it was not included, due to the transitional time period having already occurred.

This research intends to examine similar characteristics under the less than ideal cases that Bonin (2013) describes in his work. Methods from the literature described earlier are used to characterize the transition on nights with more complicated atmospheric forcing. These "less than ideal" cases have not been examined in the past, yet happen quite frequently in the atmosphere to warrant an in-depth study.

III.   EXPERIMENT LOCATION AND INSTRUMENTATION

A.   EXPERIMENT LOCATION

This thesis focuses on the AET during late spring and early summer. The data collected to examine this phenomenon was obtained during a large scale, multi institution field campaign known as Plains Elevated Convection at Night (PECAN). PECAN took place over the central plains, primarily focusing on Kansas, during the months of June 1-July 15, 2015. PECAN was a multi-agency project designed to advance the understanding of continental nocturnal precipitation during the warm season. This project focused on nocturnal convection in conditions of the central United States plains states with a stable boundary layer, a nocturnal low-level jet and the largest convective available potential energy located above the stable boundary layer. There was an additional emphasis focusing on enhanced understanding of nocturnal convection initiation, mesoscale convective systems, bores, and the development of the nocturnal low-level jet. This thesis research fits in to the later, as the nocturnal boundary layer and the low-level jet are related. Three aircraft were used as well as a large array of fixed and mobile ground instruments were deployed across Kansas. The data used in this thesis was collected primarily at one of the fixed PECAN Integrated Sounding Array (PISA) site # 2 (FP2) located at Greensburg, KS. Figure 3 shows the location of the PECAN data collection sites.
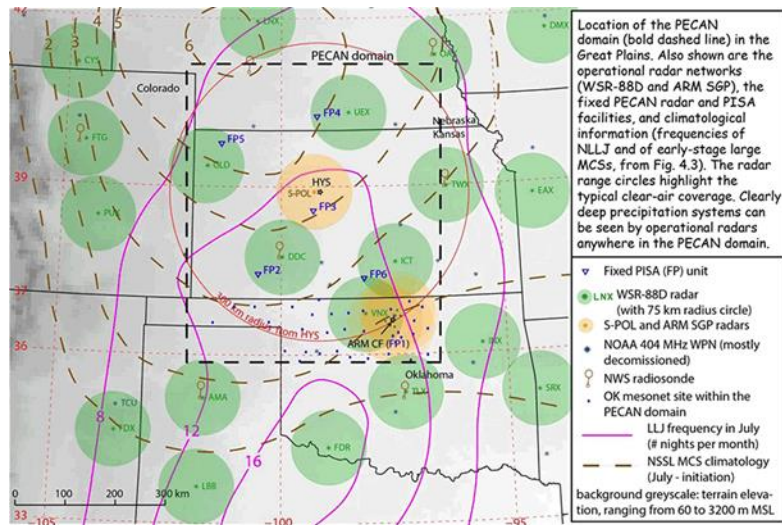
Figure 3. Domain for PECAN Measurement Campaign (National Severe Storms Laboratory, 2015).

The NPS measurement site was part of fixed PISA site number two, or FP2, located in Greensburg, KS. Co-located at FP2 was a team from the University of Maryland, Baltimore County (UMBC). Our site was situated approximately 45 miles east of the Dodge City, KS National Weather Service station (KDDC).
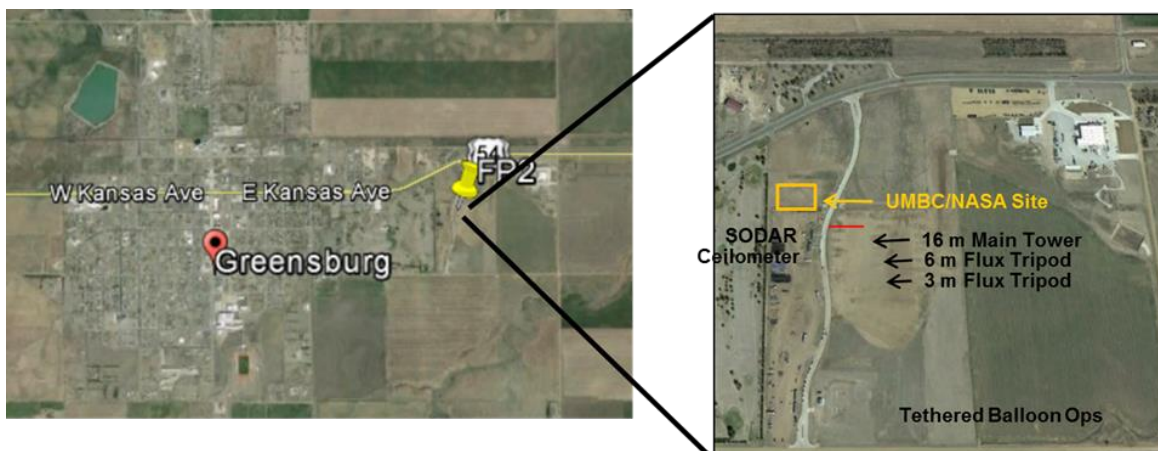
Location of FP2 relative to Greensburg, KS. Also shows the location of instruments at FP2.

Figure 4. FP2 Location and Instrument Locations.

B.   EXPERIMENT INSTRUMENTATION

The location chosen is a uniformly flat field located east of Greensburg, KS as depicted in Figure 4. The terrain was a grassy field, with crops located in the adjacent fields approximately 400 meters to the east and 1500 meters to the south. NPS measurements at FP2 were taken from a 16-m flux tower, a 6-m tripod flux tower, a smaller 3-m scalar and radiation tripod tower, a sonic detection and ranging (SODAR) device, a ceilometer, a tethered balloon system with Anasphere tethersondes, and radiosonde weather balloon launches, some of which are seen in Figure 5. Additionally, rawinsonde launch data and Doppler LIDAR data collected by the UMBC team were also used for this study, as well as radar archives from the Iowa State meteorology website.
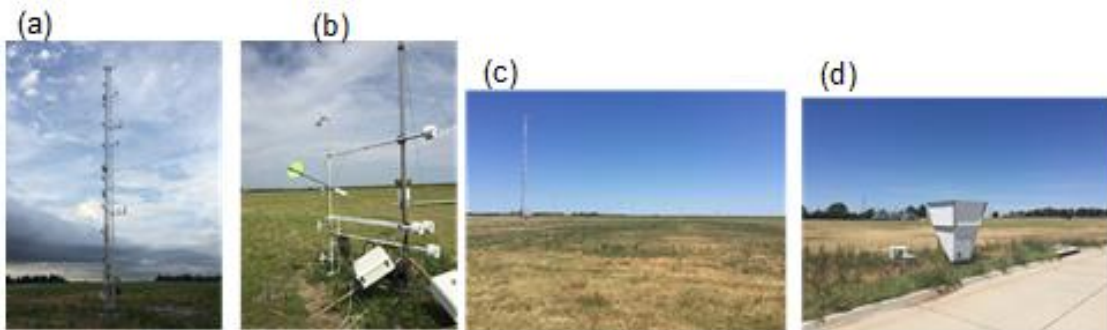
From left to right (a) 16-m Flux tower, (b) 3-m scaler tripod, (c) the setup of the 16-m tower, 6-m,and 3-m tripods, and (d) mini SODAR.

Figure 5. Instruments Located at FP2.

In Table 1 is a brief summary of the instrumentation used at FP2. The rest of this chapter will include a more in-depth description of each instrument, as well as any limiting and amplifying information will be discussed.

Table 1. Summary of Instrumentation Used at FP2.

Instruments	Variables Measured	Levels Measured (m)	Dates Available (2015)
16-meter tower	latent/sensible/ momentum flux	2.83, 5.66, 11.32 and 16	June 14 – July 15
	temperature/specific humidity	0.86, 1.63, 2.82, 4.21, 5.64, 7.47, 9.65, 11.32, 12.72, 14.48, and 15.98	June 14 – July 15
	u/v/w wind component	2.83, 5.66, 11.32 and 16	June 14 – July 15
6-meter tripod	latent/sensible/ momentum Flux	2.83 and 5.66	June 4 – July 15
	u/v/w wind components	2.83 and 5.66	June 4 – July 15
Mini SODAR	TKE/u/v/w wind component	15-250 meters with 5m vertical resolution	June 1 – July 15
Tether Balloon System	temperature/specific humidity/wind speed/wind direction	10- approx. 400 meters	June 25, June 28, June 29, July 2, July 4
Ceilometer	Cloud base height	Up to 7500 meters	June 1 – July 15
LIDAR	u/v/w wind components	Vertical scan up to 1500 meters	June 2-July 14
	u/v/w wind components	Radial scans up to 500 meters	June 2-July 15

At the experiment sight, a 16-meter tower was erected. Turbulent momentum, latent heat and sensible heat flux were measured at four levels; 2.83, 5.66, 11.32 and 16 meters. The lower two levels of flux were obtained by using a CSI CSAT3 3-D sonic anemometer, while the top level fluxes were obtained by using a CSI IRAGASON; both of which measured U,V,W wind components as well as sonic temperature. The high rate data collections for fluxes were made at a 20 Hz rate. Mean wind, temperature, relative humidity and pressure were measured at two levels, 10 and 14 meters with Visalia WXT520 weather stations. Twelve additional levels of temperature and relative humidity

14

probes with naturally ventilated radiation shields were placed at 0.86, 1.63, 2.82, 4.21, 5.64, 7.47, 9.65, 11.32, 12.72, 14.48, and 15.98 meters. The WXT520 and other temperature and relative humidity probes sampled at 1 Hz with averages also saved at 10 second, 1 minute and 10-minute increments. Tower data was collected from June 14 to July 15; however, there are short time periods when no data is available due to power outage and/or data recording issues.

The flux tripod was 5.66 meters tall and was instrumented at two levels, one in the middle of the tower at 2.83 meters and one at the top. The lower level had a Campbell Scientific CSAT3 anemometer and a LI-COR 7500 Open Path Infrared Gas Analyzer to measure high-rate 3-D winds and water vapor and CO_2 concentrations. The top level had a Campbell Scientific IRGASON that is an integrated sonic anemometer and infrared gas analyzer with both sampling volumes collocated. Both levels had Rotronic HC2-S3 probes to measure mean air temperature and relative humidity. Barometric pressures at each level were measured with internal IRGASON and LI-7500 barometers. Data was collected at 50 Hz with a Campbell Scientific CR3000 micro logger and time synchronized with a Garmin GPS16X-HVS GPS receiver. Data was collected from the flux tripod from June 4 to July 15, 2015 with some periods of data gap due to power loss or other technical issues.

Additionally, at FP2, an ASC Model 4000 MiniSODAR was used. The miniSODAR is a high-frequency Doppler SODAR system that was designed to measure the atmospheric wind profile from 15 meters to 150/200 meters (data is often available to 250 meters) in 5-meter increments. "The SODAR measured wind speed through Doppler frequency shift, a shift in the received frequency with respect to the transmitted frequency, which is directly related to the radial motion of the echo volume with respect to the miniSODAR acoustic antenna" (Atmospheric Systems Corporation 2016). Data was collected from the sodar from June 1 to July 15, with some periods of data gap due to technical issues with the sensor.

Vertical profiles of temperature, relative humidity, and wind were collected with a tethersonde system from ground level to 300–450 meters. During the PECAN experiment, we utilized a 16 cubic meter aerostat balloon. Two different instruments were utilized to collect data, initially the Anasphere SmartTether Version 8 and later with the addition of an iMET-1-AXBN radiosonde. Both were attached to the tether at approximately five meters below the balloon. The Anasphere SmartTether measured temperature, relative humidity, pressure, wind speed and direction, and GPS location. The wind speeds are measured with either a pitot tube or cup and vane system. The iMET radiosonde measured only the thermodynamic properties and GPS location. Measurements were wirelessly transmitted from the sensor module to their respective receivers. The iMET rawinsonde was added due to the slow time response of the temperature and relative humidity in the Anasphere SmartTether. In the field data analyses indicated that the SmartTether was not capable of capturing the vertical gradients in the sample profile for the speed of sensor ascent/descent. However, the wind direction and speed did not exhibit these slow responses and are valid for use. The iMET-1-AXBN radiosonde was designed to sample the vertical profiles at a balloon ascent speed of 3–6 m/s, comparable or slightly faster than the tethered balloon ascent speed controlled by the winch.

To determine if clouds were present, a Vaisala CL31 laser ceilometer was used. This ceilometer has five-meter vertical resolution, with measurements up to 7500 meters. "The CL31 employs a pulsed diode laser LIDAR (light detection and ranging). The ceilometer uses the backscatter of light to determine the height of the cloud base as well as vertical visibility" (Vaisala 2015). The cloud-based height will be utilized in this thesis. The data was recorded in one-minute time interval over the course of the campaign. The raw data from the ceilometer was processed and saved in netcdf format. Data is available from the ceilometer from June 1 to July 15, with minor interruptions due to power outages.

Adjacent to our location, the UMBC team also collected sounding data for the FP2 site. This thesis utilized their radiosondes data to compare vertical

profiles, as well as obtain vertical profiles above the limit of our tethered balloon system. Soundings were collected from May 31 to July 16, 2015. The UMBC soundings have a 1-second temporal resolution and sampled the standard thermodynamic properties as well as wind speed and direction.

Wind speed and vertical velocity profiles were measured through a deeper layer using a Leosphere 200s scanning wind LIDAR, a commercially manufactured coherent Doppler LIDAR from the UMBC location. The instrument produces line-of-sight wind speeds derived from the Doppler frequency shift in backscattered photons off of atmospheric aerosols. Multiple scan modes were used in the LIDAR operation. The Range Height Indicator (RHI) scan mode uses five elevation angles at 45°, 20°, 10°, 7.5^o, and 5°, each has a different vertical range, resolution, and blind zone. The range resolution of RHI scan at 45° was used in this thesis work. Its vertical resolution was 50 meters with a maximum height of 6000 meters and a 100-meter blind zone. To derive vertical velocity, the vertical stare mode was used. This mode was done for 300 seconds before switching to the RHI scan mode. This yields an iteration of five minutes of vertical stare, then conical scans recording every second. The LIDAR was recording continuously over the course of 24 hours from June 2 to July 15. There were minor outages due to power losses.

THIS PAGE INTENTIONALLY LEFT BLANK

IV.   DATA ANALYSES AND RESULTS

A.   DATA PROCESSING

The PECAN data was measured at two different sampling rates. At the flux sampling levels on the 16-m tower, (2.83, 5.66, 11.32 and 16 meters), wind, virtual temperature, and water vapor density were sampled at 20 Hz intended for turbulence characterization. For the rest of the main tower and the 3-m scalar tripod levels, the original data was sampled at 1 Hz. These original measurements went through extensive data quality control to remove apparently erroneous data. Further data processing was made to obtain 20-minute averages of mean temperature, humidity, and wind as well as turbulence fluxes. Kinematic flux calculation was done using the 20 Hz data with the eddy correlation method. To obtain momentum, sensible, and latent heat fluxes, air density, heat capacity under constant pressure, and latent heat were multiplied to the respective kinematic fluxes. All the mean variables were averaged over the same data sections as for the fluxes for analyses.

B.   CASE SELECTION

This thesis uses data measured from the 16-m flux tower, the 3-m scaler tripod, and the Leosphere wind LIDAR as the main data source. The rest of the instruments in chapter III were used to provide supporting information such as cloud cover and precipitation as needed. Specifically, the thermodynamic variables temperature, specific humidity, wind speed and wind direction are examined for their temporal variations for a 24-hour period that cover the event of interest. This information was supplemented with vertical profiles centered on convective events of interest. Similarly, the temporal variations of momentum, sensible and latent heat fluxes were examined. Vertical profiles of the fluxes were not examined due to the limited level of measurements. The time period of the entire dataset is from June 1 to July 14, 2015 while the 16-m tower only

started data collection on June 14, 2015, due the extended amount of work associated with setting up and instrumenting a tall tower.

To identify cloud coverage as a result of convection, the ceilometer measurements of the cloud base were used. We chose to evaluate the effects of low-level cloud defined as those with cloud base height less than 1000 m. Two independent precipitation measurements were made on the 16-m main tower and the 3-m scalar tripod. The measurement by the Vaisala WXT520 weather station on the main tower was used to define the time periods affected by precipitation since data from the scalar tripod do not appear reasonable.

The cases were initially selected by using archived nearby radar and satellite data. This yielded 17 days where there was convection or low level clouds near FP2. The ceilometer and precipitation measurements confirmed the initial selection. These cases were grouped into three categories for further analysis to include precipitation events, low-level clouds and an "others" group which includes the days with impact of convection where the precipitation and cloud categories do not apply. One of the events in the "others" group is the passing of the convective outflow boundaries. Further analyses focused on days after June 14, when surface flux data at FP2 became available. This yielded 12 cases in the three above-mentioned categories summarized in Table 2. On days where there are either multiple precipitation events or events that have both precipitation and cloud events, each event was analyzed separately.

Table 2. Observed Cases with Convection Related Events.

Date	Precipitation	Low-Level Clouds	Other
June 06		X	
June 07	X		
June 10			
June 11	X	X	
June 12		X	
June 14	X	X	
June 22			X
June 25	X		
June 28			X
June 29			X
July 02	X		
July 03	X	X	
July 06	X	X	
July 13		X	

The next subsection will examine the effects of each convective case on the surface layer properties. Convective events including precipitation will first be explored. Then cases that only included cloud cover from adjacent convective events will be analyzed. Finally, case days that met the initial criteria, however lack direct precipitation or cloud cover events will be examined. Although the focus of this thesis is on AET and how convective events affect the AET, we will also evaluate the effects of convection at other times of the day on the boundary layer turbulence and thermodynamics.

C.   CASE ANALYSIS

There are a total of seven precipitation events on 5 days, 4 low-level cloud cases, and 2 cases in the "other" category to be discussed in this chapter. Each case will include vertical profiles of potential temperature and specific humidity from the 16-meter tower and the mean wind and vertical velocity variance from the Leosphere LIDAR in a deeper layer. The LIDAR profiles of the variance in vertical velocity are used as a proxy for turbulence. Only cases that occurred after June 14, 2015, will be analyzed in detail as the measurements from the 16-

meter tower are available after this date. Each event is examined at how the event of interest impacts the lower boundary layer.

This thesis also examined the general characteristics of the AET without potential influence of convection. The many cases identified show rather consistent results, which are also consistent with AET transitions depicted in previous literature discussed in chapter II. We will use one of these "noneventful" days (June 23, 2015) as a reference, which will be referred to as the "ideal" transition case.

The figures used in this chapter are consistent throughout this chapter. Each case begins with a discussion of the key observations and comparisons. The focus of the discussions is on mean wind and thermodynamic variables in the surface layer, surface fluxes and TKE, surface layer mean thermodynamic profiles, and the boundary layer mean wind profiles as seen by the Leosphere LIDAR. Each subsection will include a time series plot between 1500–1200 UTC of the mean variables (temperature, specific humidity, wind speed, and wind direction) as well as surface fluxes (momentum, sensible heat and latent heat flux) and TKE. To augment the discussion, vertical profiles of the relevant variables from time periods of interest are shown. These time periods are selected as the following. The first profile (in red) is 30 minutes prior to each convective period of interest. This is followed by two profiles during the event (blue and cyan). Finally, one profile 30 minutes after the event has ended is shown in green. Additional figures are also shown in time-height contour plots to illustrate the temporal evolution using data from 3 hours before to 3 hours after each event.

1. Ideal AET Transition

The case on June 23, 2015, is an example of a typical ideal transition case and is used for comparison for the follow on cases and to determine how the convective events affect the boundary layer. Figure 6 shows steady decrease in temperature couple with an increase in specific humidity before sunset. The

different lines of each subplot are indicated in Table 3. The decrease in temperature is a result of reduction in surface heating from downward solar radiation (not shown). The increase in water vapor was also identified in the work by Bonin (2011). At the transition time, decreases in TKE and surface fluxes are also seen during this period, consistent with results in Wingo and Knupp (2014) where abrupt decreases in TKE and near surface wind speed were observed during the onset of the transition. It is also observed during the ideal cases, that surface sensible heat fluxes became negative approximately 1 hour before sunset, denoting the onset of the stable surface layer. The timing is consistent with the low-level mean wind reaching a minimum. Following the onset of the stable surface layer, all fluxes quickly reach their nighttime values and remain steady until the end of the designated transition period.
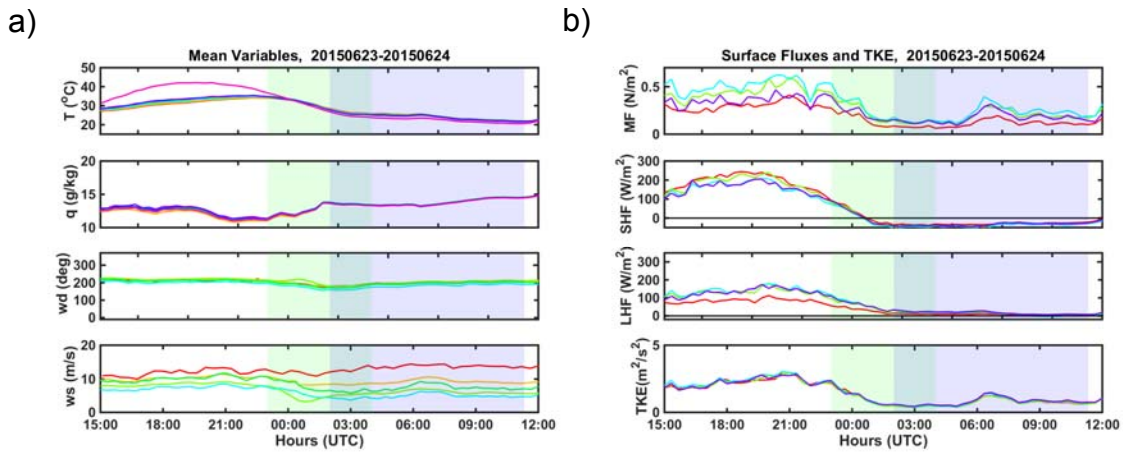
a)   b)

The temporal variations of a) observed mean temperature (T), specific humidity (q), wind direction (wd) and wind speed (ws) and b) observed fluxes during June 23 and 24, 2015. The green shading denotes the transitional period and the blue shading covers the night period defined between sunset and sunrise. The different lines in each subplot are indicated in Table 3.

Figure 6. Temporal variations of Mean Variables, Surface Fluxes and TKE June 23 and 24, 2015.

Table 3.　Height (m) of Measurements.

	Height in meters
T/q	16, 10, 5.6, 2.82, 2.4, 0.86, 0.6, skin
Ws/Wd	Avg. of 425-600, 50, 25, 16, 3
Fluxes	16, 11.32, 5.66, 2.83

The evolution of the mean wind diverges at the beginning of the transition period. The mean wind between 425 and 600 m increases while the lower layers below 50 m showed gradual decrease in wind speed until sunset. Wind direction, however, shows the same veering at all levels. This decrease of the near surface wind is likely the cause of decreases in all surface fluxes, especially momentum flux, although the reduction in the air-land temperature difference also contributes to reduction of sensible and latent heat fluxes. Flux divergence is high during the day in the convective boundary layer as shown by the differences among different levels, and becomes reduced after the onset of the transition, especially in the upper levels of the tower.

The vertical profiles and time series contour plots in Figures 7 and 8 show the temporal evolution and the onset of the transition. In both figures, a clear transition from an unstable to stable thermal gradient is observed by the shifting from a negative to positive slope of potential temperature in Figure 7. It can also be noted that the increase in near surface moisture occurs as well as the decay in low-level wind speeds, while a low level jet develops above the boundary layer. These features are all consistent with previous research showing the temporal evolution of the ideal AET.
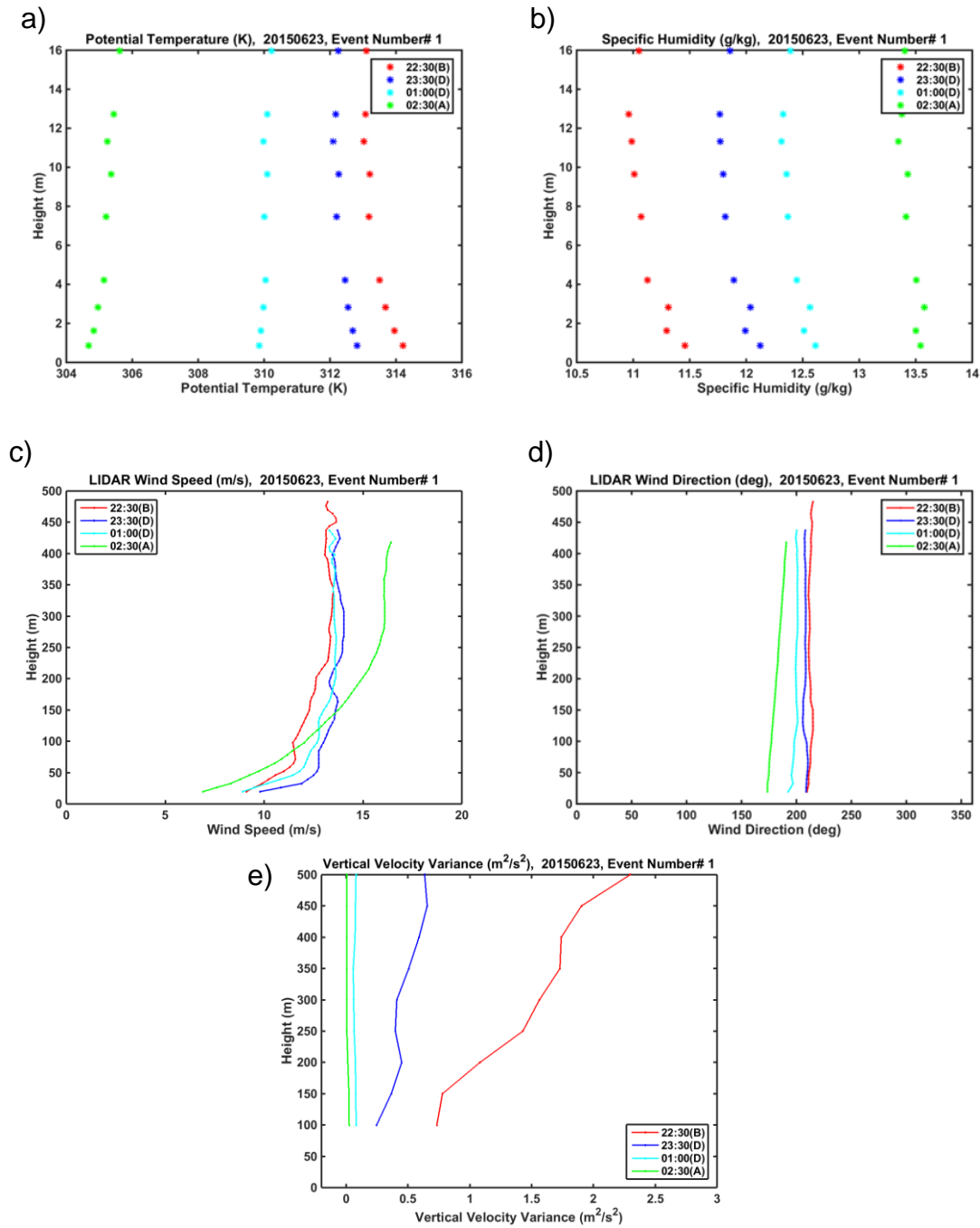
Measured vertical profiles before (B), during (D), and after (A) the transition. Parameters include a) potential temperature, b) specific humidity, c) wind direction, d) wind speed, and e) variance of vertical velocity. The potential temperature and specific humidity are from the 16-m tower. The wind speed, wind direction, and vertical velocity variance in a deeper layer are from the wind LIDAR

Figure 7. Observed Surface Layer Profiles on June 23 and 24, 2015.
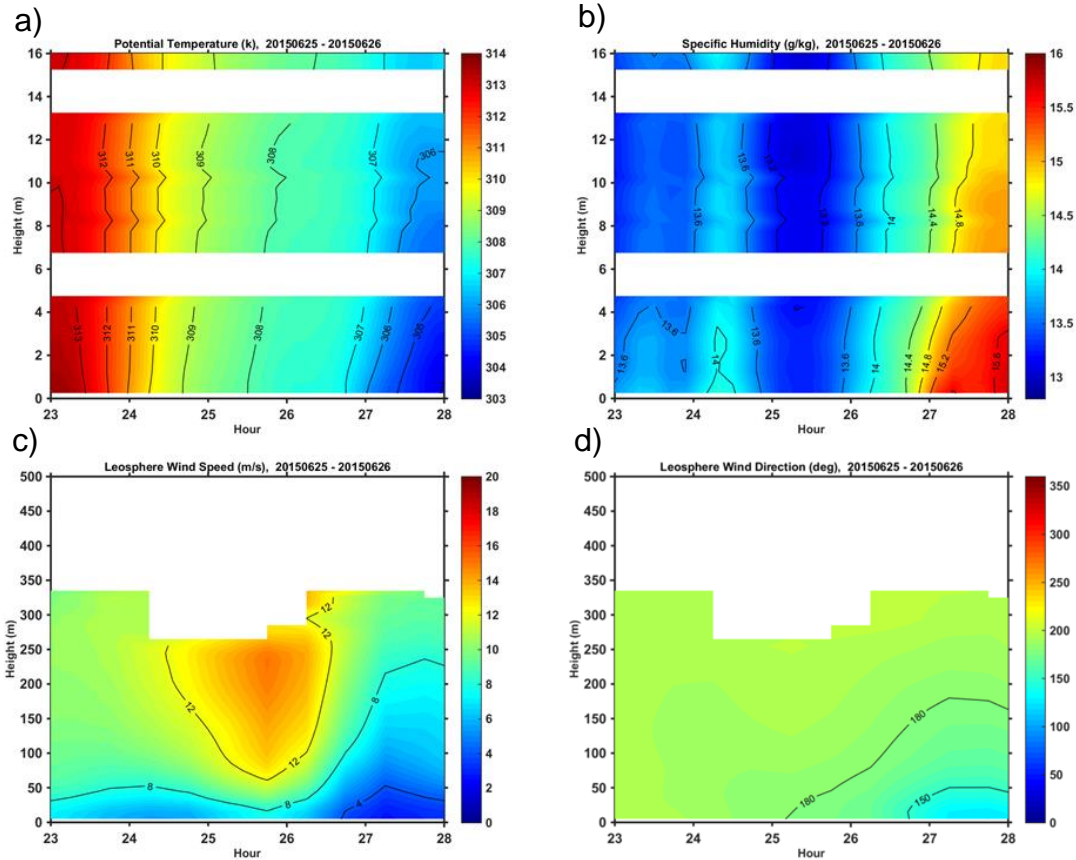
25

Time-height variations of (a) potential temperature (b) specific humidity from the 16-m tower and (c) wind speed and (d) wind direction from the LIDAR.

Figure 8. Time-Height Variations on June 23 and 24, 2015.

2.   Effects of Precipitation Events on the Boundary Layer

Convective events involving precipitation have an impact on the boundary layer and the evolution of the AET. Five cases will be examined here, which took place on June 14, 25, July 2, 3, and 6. Each case varies slightly, to include timing on which precipitation occurred at FP2 which has varying impacts on the boundary layer and the evolution of the AET.

a.   *June 14, 2015*

Two separate convective events occurred involving precipitation over FP2 on June 14, 2015. Event 1 took place between 1750–1842 UTC, approximately 4 hours

prior to the transition period, while the second took place during the transition, from 0115–0300 UTC as denoted by the red vertical dash lines in Figure 9.
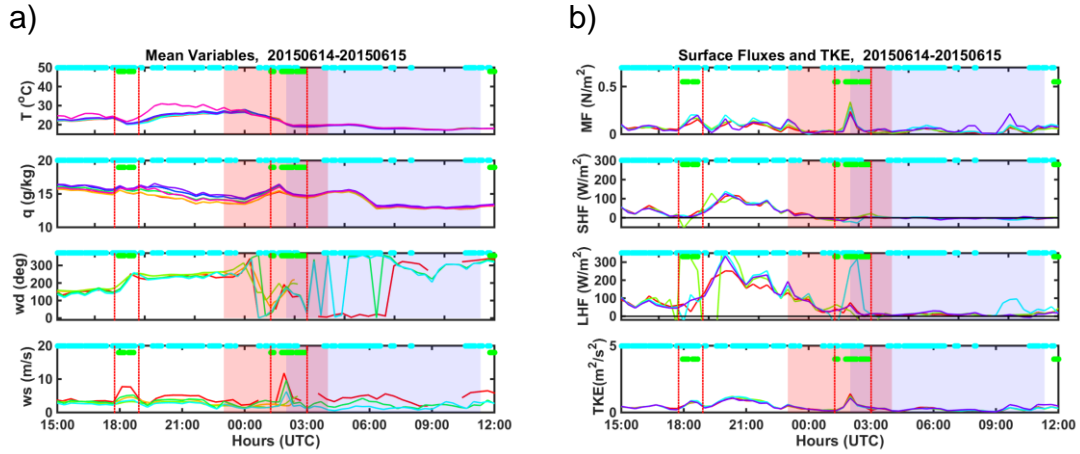
a)

b)

The temporal variations of a) observed mean temperature (T), specific humidity (q), wind direction (wd) and wind speed (ws) and b) observed fluxes during June 14 and 15, 2015. The red shading denotes the transitional period and the blue shading covers the night period defined between sunset and sunrise. The different lines in each subplot are indicated in Table 3.

Figure 9. Temporal Variations of Mean Variables, Surface Fluxes and TKE June14 and 15, 2015.

Measurements on this day allow us to examine how precipitating convective events affect the boundary layer and whether any residual effects of a recent event may impact the AET. The time series in Figure 9 show some interesting features that are different from the ideal case. Both TKE and surface momentum flux display a local peak during each event, this is likely caused by the increase of winds throughout the boundary layer. Such increase of winds is likely attributed to the inflow and outflow of the convective system as it moves through FP2. While the second event occurred during the transition, it should be noted that some features from the ideal transition still occurred. These include the steady decline of temperature, although overall magnitude was reduced, and the increase of moisture that occurred near sunset.

Figures 10 and 11 examine how the convective event impacts the lower boundary layer. In both events, the convective precipitation stabilizes the lower boundary layer, as depicted by the potential temperature profiles changing from

27

unstable to a neutral gradient. This stabilization was only a temporary effect, and within 30 minutes after the first event, the lower boundary layer regressed to an unstable condition. This was found to be consistent throughout cases where the event ended during the daytime hours.
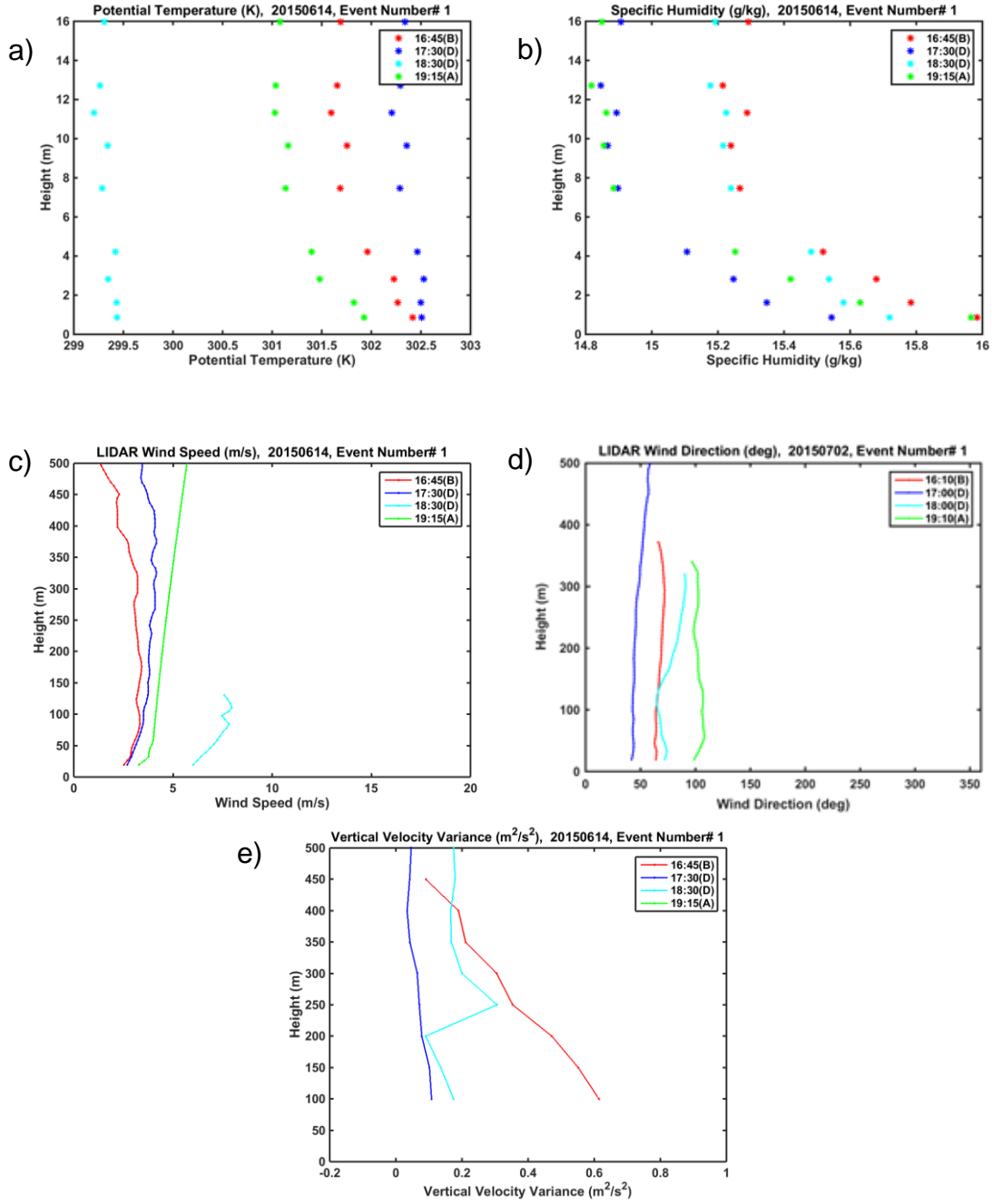
Measured vertical profiles before (B), during (D), and after (A) the first precipitation event. Parameters include a) potential temperature, b) specific humidity, c) wind direction ,d) wind speed, and e) variance of vertical velocity. The potential temperature and specific humidity are from the 16-m tower. The wind speed, wind direction, and vertical velocity variance in a deeper layer are from the wind LIDAR.

Figure 10.   Observed Surface Layer Profiles on Event 1, June 14 and 15, 2015.
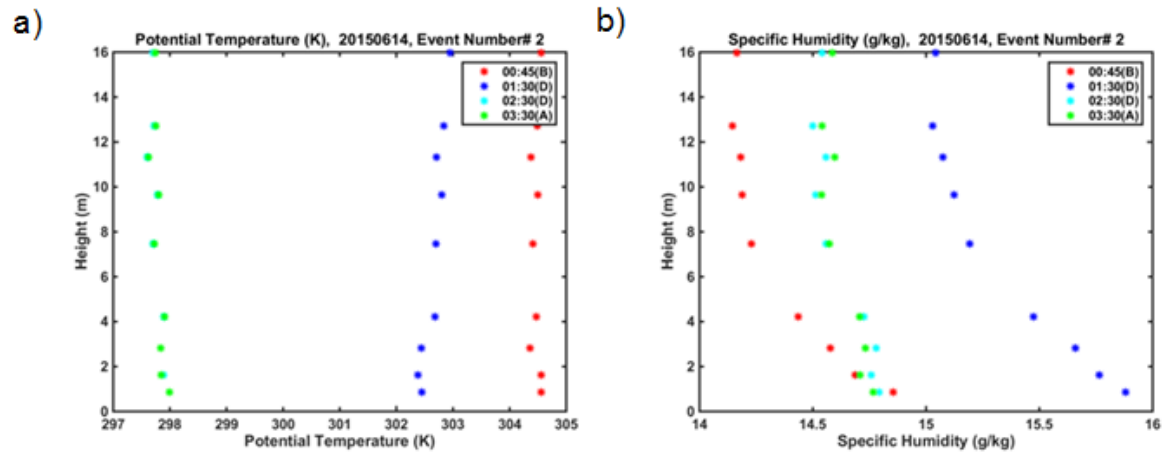
(a) Measured vertical profiles before (B), during (D), and after (A) the second precipitation event. Parameters include a) potential temperature and b) specific humidity from the 16-m tower.

Figure 11.　Observed Surface Layer Profiles on Event 2, June 14 and 15, 2015.
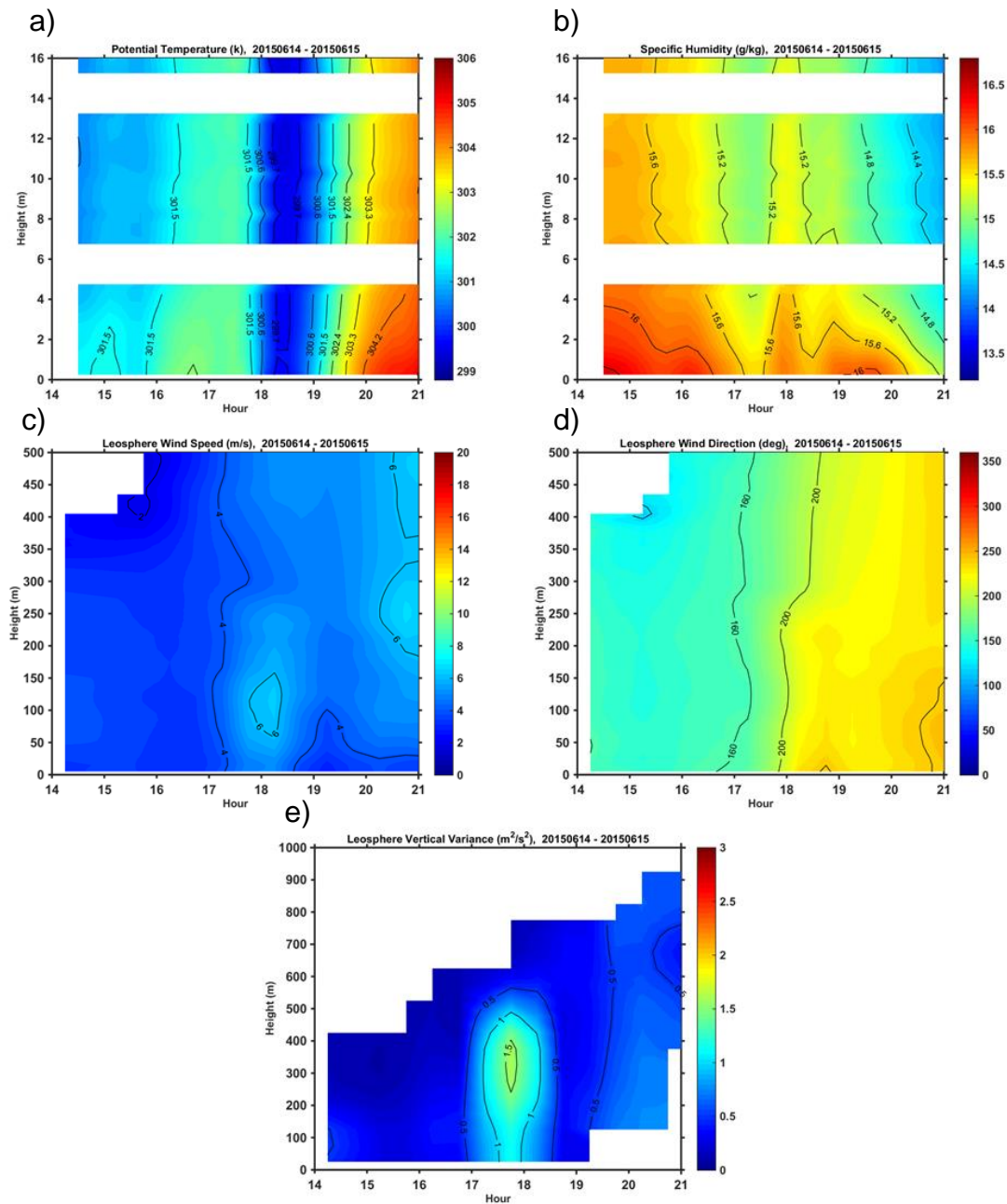
Time-height variations from event 1 on June 14 and 15 of (a) potential temperature (b) specific humidity from the 16-m tower and (c) wind speed, (d) wind direction and (e) variance of vertical velocity from the LIDAR.

Figure 12.   Time-Height Variations on Event 1, June14 and 15, 2015.
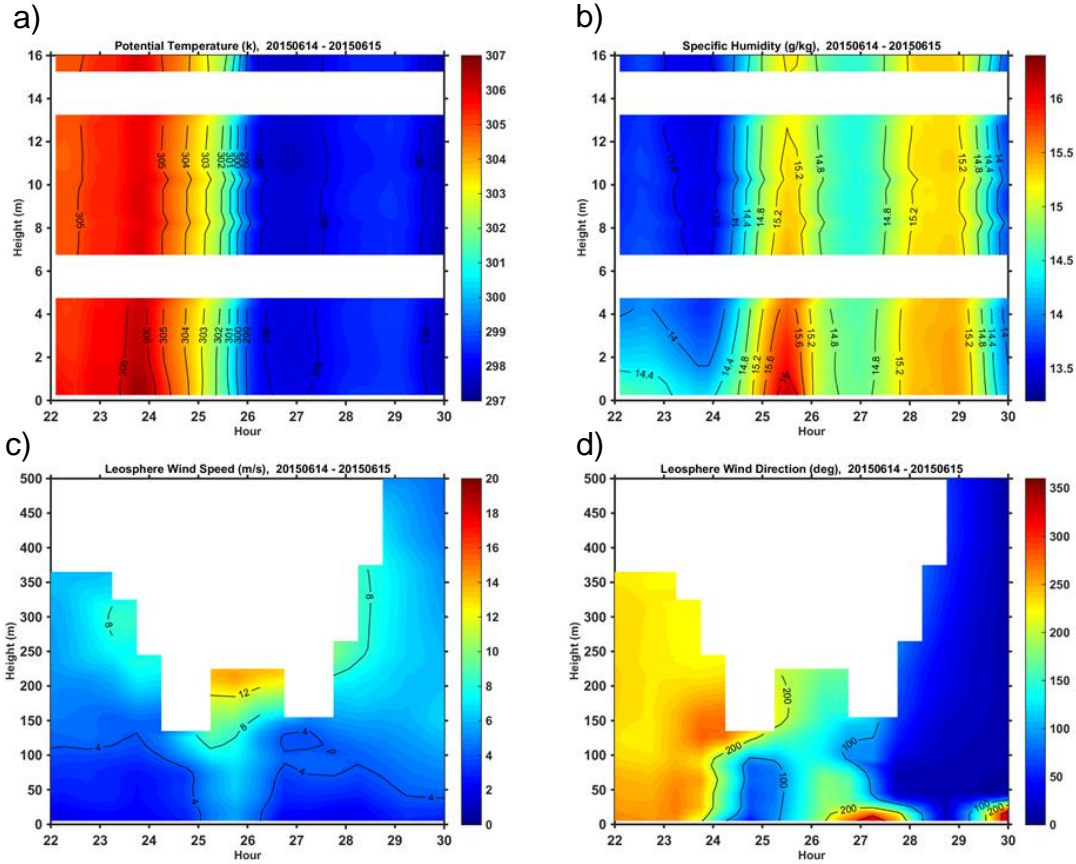
(a) Time-height variations from event 2 on June 14 and 15 of (a) potential temperature (b) specific humidity from the 16-m tower and (c) wind speed and (d) wind direction from the LIDAR.

Figure 13.   Time-Height Variations on Event 2, June 14 and 15, 2015.

Figures 12 and 13 depict the temporal variations of the various variables for events 1 and 2, respectively for an extended period. Here, the features noted in the vertical profiles can be more readily seen including the slight increase in wind speed, the veering of the mean wind at all levels below 500 meters and above (not shown), and the enhancement of the vertical velocity variance. Also of note is the rapid decrease in temperature at the onset of the precipitation event that reached the coldest temperature in the middle of the event one. The drying of the surface layer before event two followed by an increase in moisture, particularly in the lowest layers toward the end of the precipitation event can also be clearly identified in Figure 12. This increase in moisture may be attributed to the transport of moisture due to convergence in the outflow boundary, which we

are not able to verify from our dataset. Figure 13 shows similar results as in Figure 12, except some low-level directional wind shear is also observed. Clear and distinct wind shifts can be seen during the second event that coincides with the increase of TKE during this event. This shear is apparent in the lowest 200m of the boundary layer.

b.   June 25, 2015

June 25 is a case where precipitation moves over FP2 after the onset of the transition and occurred during sunset. This timing is similar to July 6 to be discussed later in this chapter. The precipitation occurred between 0200–0300 UTC.

The time series shown in Figure 14 depicts a lot of similarities between this case and the ideal transition discussed earlier in this chapter, a result that the event occurred after the onset of the transition. After the beginning of the event, differences between this case and the ideal case became apparent. Although TKE decayed during the transition, there was a measurable increase in both TKE and momentum flux during the precipitation event. These spikes can be attributed to both the speed and directional shear throughout the boundary layer that generated turbulence mixing and TKE. The precipitation event also occurred at sunset, at the same time specific humidity would be expected to increase in an ideal transition. This near sunset spike in moisture is delayed until after the precipitation event ended, resulting in almost a 2 hour delay in the onset of the moisture increase.
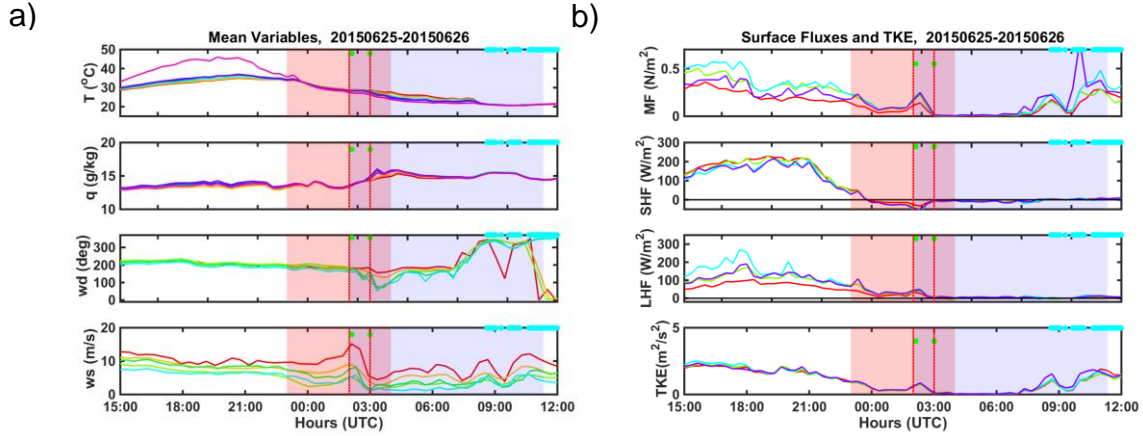
a)

b)

The temporal variations of a) observed mean temperature (T), specific humidity (q), wind direction (wd) and wind speed (ws) and b) observed fluxes during June 25 and 26, 2015. The red shading denotes the transitional period and the blue shading covers the night period defined between sunset and sunrise. The different lines in each subplot are indicated in Table 3.

Figure 14.   Temporal Variations of Mean Variables, Surface Fluxes and TKE June 25 and 26, 2015.

Consistent with the other cases, the precipitation event contributed to an increase in the stability in the lower boundary layer. This can be seen in both the vertical profiles of the event in Figure 15 and the time-height contour plot in Figure 16. Also consistent with this case is the decrease in surface winds after the precipitation ended. This evolution of wind again is likely associated with outflow front of the convective system, and occurs before the end of the precipitation. At the end of the precipitation, the winds are noticeably reduced throughout the lowest 300 meters.
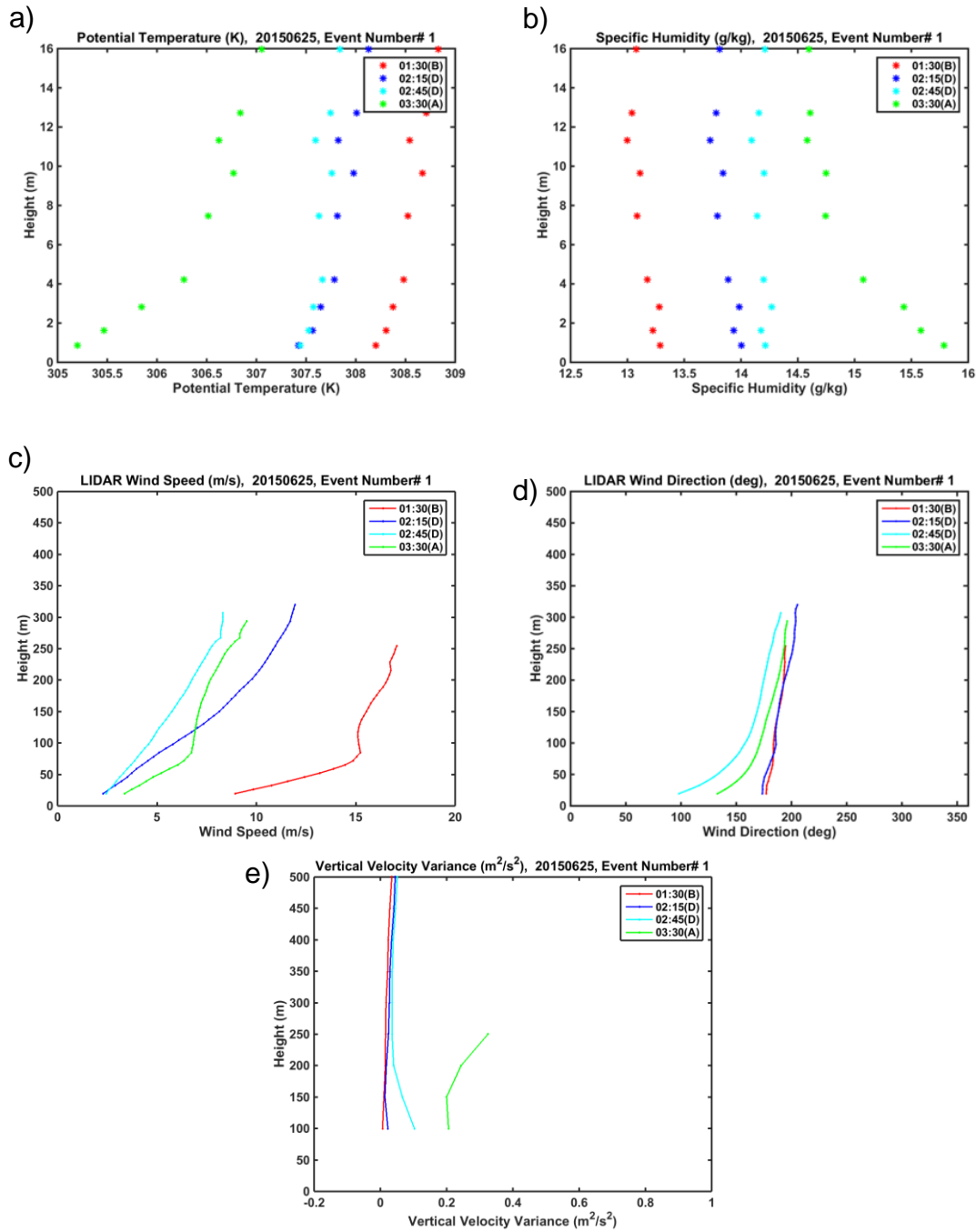
Measured vertical profiles before (B), during (D), and after (A) the first precipitation event. Parameters include a) potential temperature, b) specific humidity, c) wind direction, d) wind speed, and e) variance of vertical velocity. The potential temperature and specific humidity are from the 16-m tower. The wind speed, wind direction, and vertical velocity variance in a deeper layer are from the wind LIDAR.

Figure 15.   Observed Surface Layer Profiles on June 25 and 26, 2015.
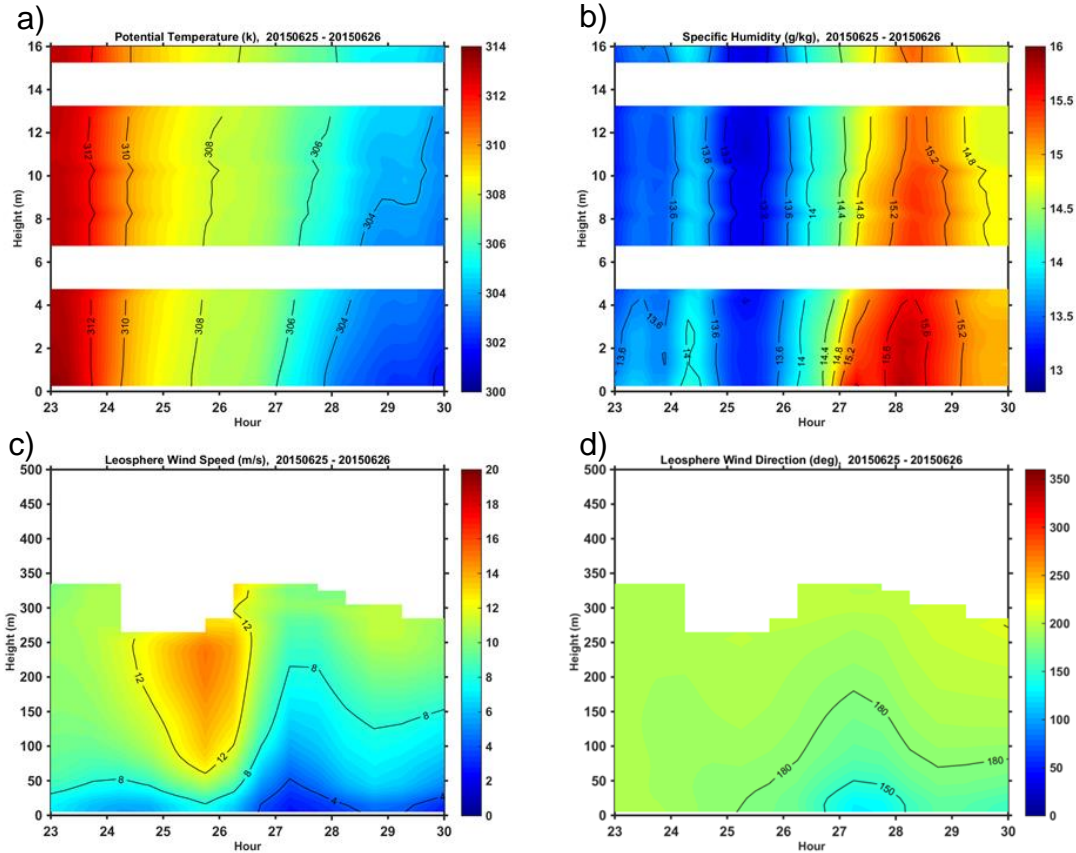
Time-height variations from June 25 and 26, of (a) potential temperature (b) specific humidity from the 16-m tower and (c) wind speed and (d) wind direction from the LIDAR.

Figure 16.   Time-Height Variations on June 25 and 26, 2015.

c.   *July 2, 2015*

Similar to the June 14 case, there were also two separate convective events on the afternoon of July 2, both prior to the onset of the AET. The first event took place between 1640–1840 UTC and the second occurred from 2000–2200 UTC.

Figure 17 shows that sensible and latent heat flux was substantially reduced during the convective events, which was also consistent with other convective days. After the end of the second precipitation event and before the onset of the transition, the surface fluxes recovered slightly to form a temporal variation that was similar to those that occurred during the ideal transition.

36

However, the magnitude of the surface fluxes and TKE at the onset of the transition was greatly reduced. Apparently, the reduction of buoyancy and the lack of wind shear resulted in weaker turbulence field. In this case, the temperature actually increased during the transition relative to the cooled air as a result of the precipitation event, before decreasing after sunset.
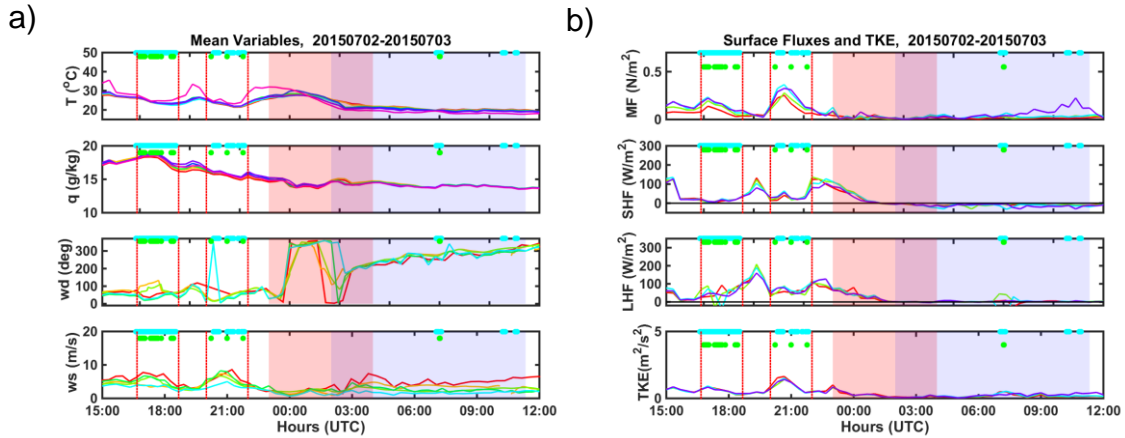
a)

b)

The temporal variations of a) observed mean temperature (T), specific humidity (q), wind direction (wd) and wind speed (ws) and b) observed fluxes during July 02 and 03, 2015. The red shading denotes the transitional period and the blue shading covers the night period defined between sunset and sunrise. The different lines in each subplot are indicated in Table 3.

Figure 17.   Temporal Variations of Mean Variables, Surface Fluxes and TKE July 02 and 03, 2015.

This case is similar to the June 14 case in several ways. The events acted to stabilize the lower boundary layer as seen in changes in the gradient in the profiles of potential temperature in Figure 18. As in the first event on June 14, once the convective event cleared at FP2, the boundary layer quickly recovered to the unstable stratification. The near surface moisture gradient was also increased during both events, again likely attributed to the moisture convergence as the outflow front passed over FP2.

37
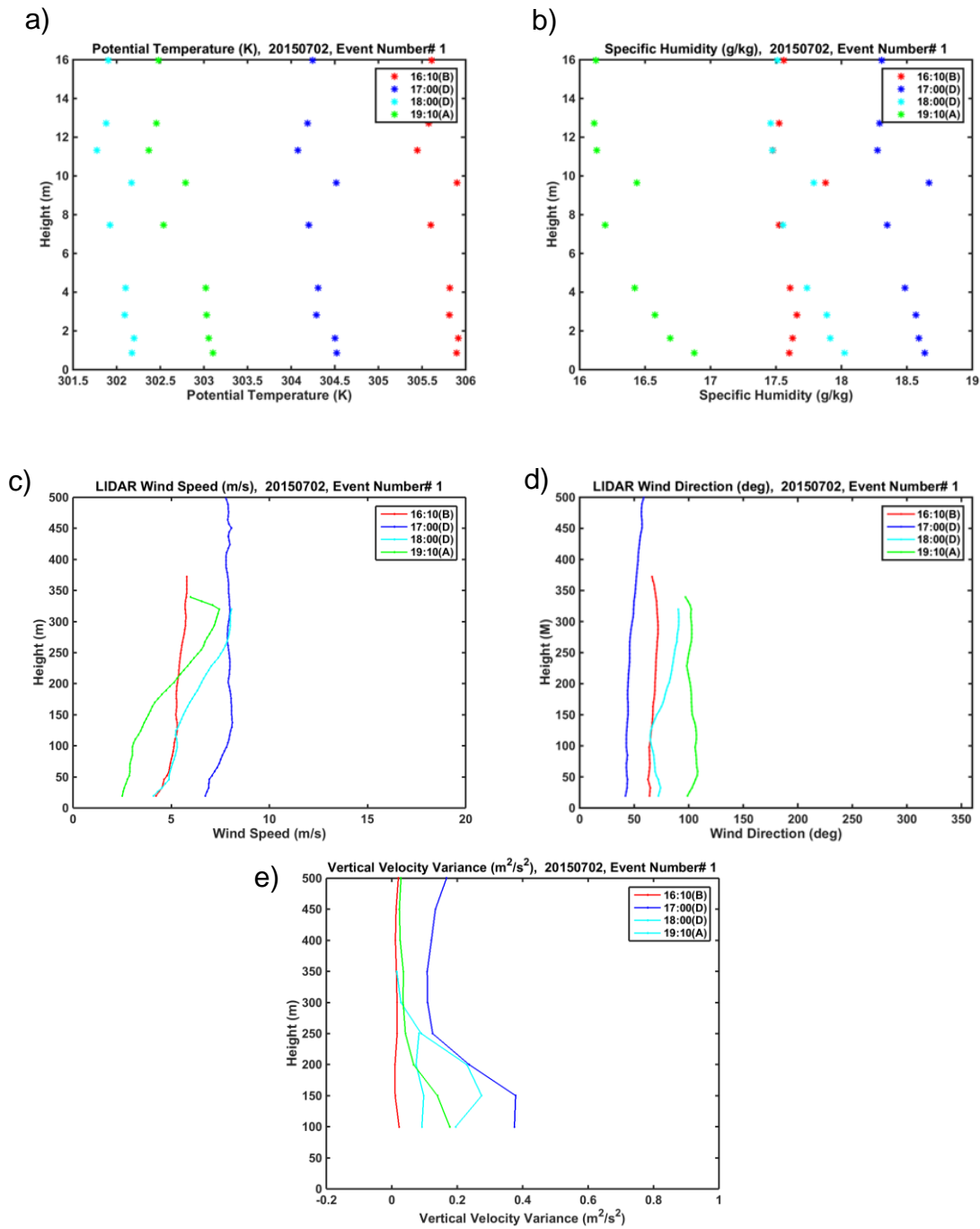
Measured vertical profiles from event 1 before (B), during (D), and after (A) the first precipitation event. Parameters include a) potential temperature, b) specific humidity, c) wind direction, d) wind speed, and e) variance of vertical velocity. The potential temperature and specific humidity are from the 16-m tower. The wind speed, wind direction, and vertical velocity variance in a deeper layer are from the wind LIDAR.

Figure 18.   Observed Surface Layer Profiles From Event 1 on July 02 and 03, 2015.
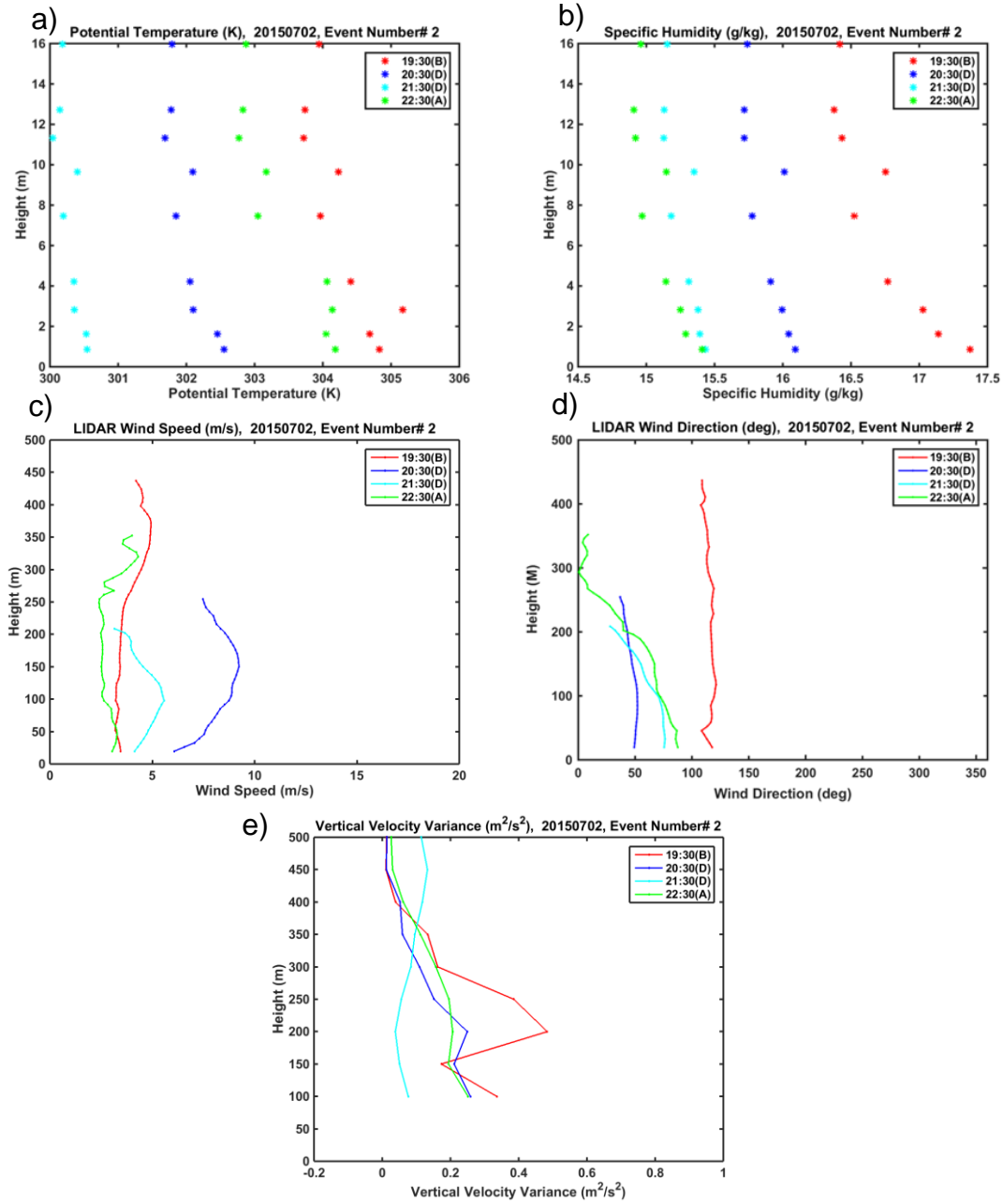
Measured vertical profiles from event 2 before (B), during (D), and after (A) the first precipitation event. Parameters include a) potential temperature, b) specific humidity, c) wind direction, d) wind speed, and e) variance of vertical velocity. The potential temperature and specific humidity are from the 16-m tower. The wind speed, wind direction, and vertical velocity variance in a deeper layer are from the wind LIDAR.

Figure 19.   Observed Surface Layer Profiles From Event 2 on July 02 and 03, 2015.
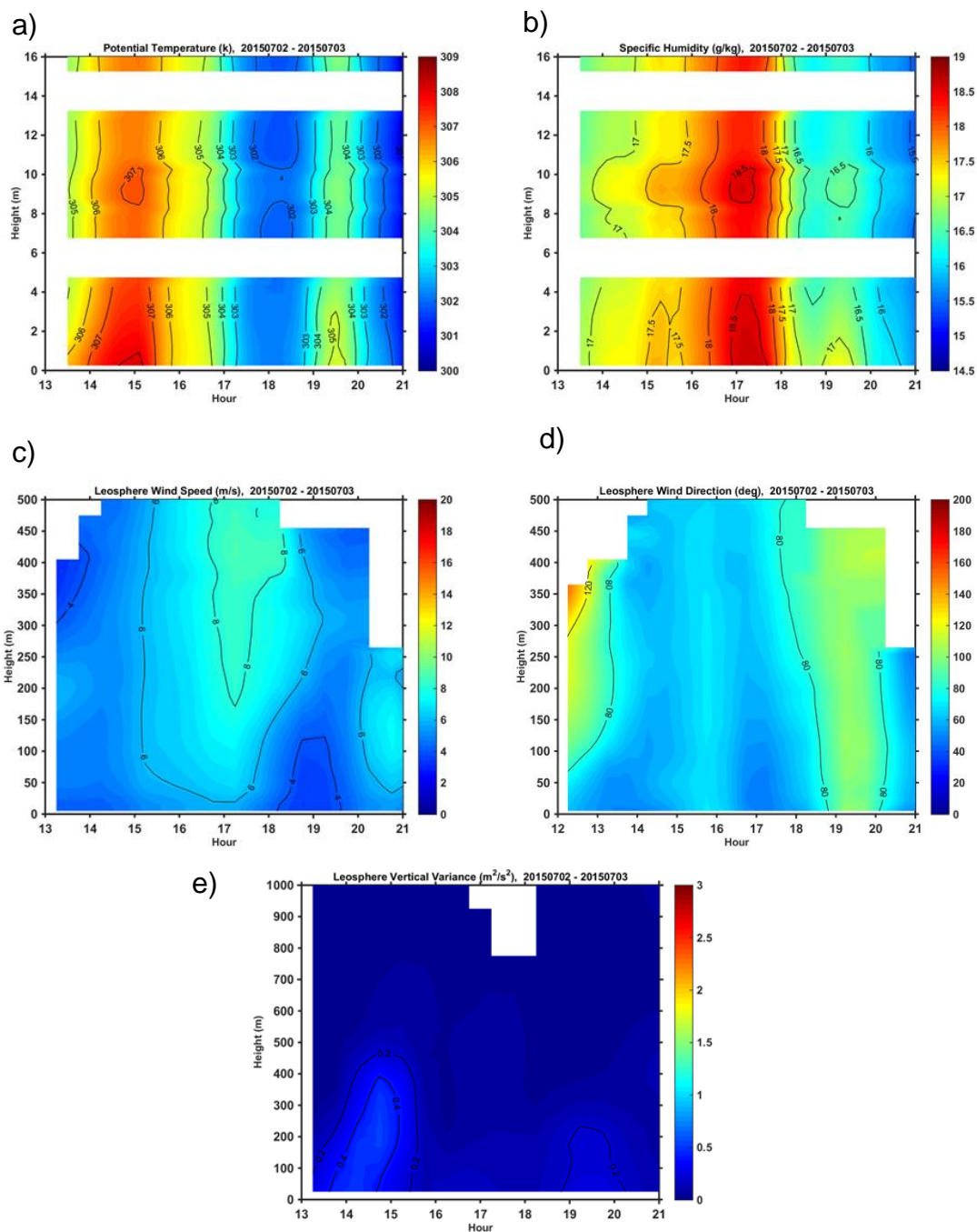
Time-height variations from event 1 on July 02 and 03, of (a) potential temperature (b) specific humidity from the 16-m tower and (c) wind speed, (d) wind direction, and (e) variance of vertical velocity from the LIDAR.

Figure 20.   Time-Height Variations Event 1 on July 02 and 03, 2015.
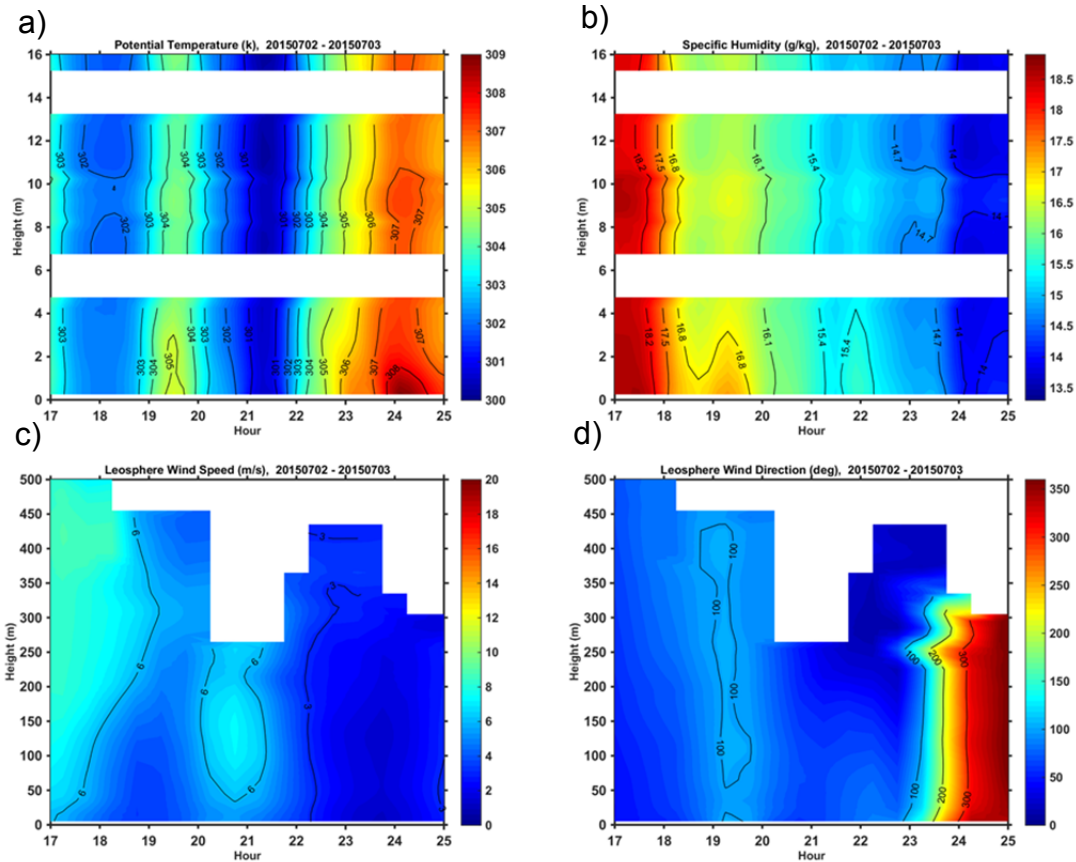
(a) Time-height variations from event 2 on July 02 and 03, of (a) potential temperature (b) specific humidity from the 16-m tower and (c) wind speed and (d) wind direction from the LIDAR.

Figure 21.   Time-Height Variations Event 2 on July 02 and 03, 2015.

d.   July 3, 2015

July 3 precipitation case is similar to the first events on June 14 and July 2, in that the precipitation affected FP2 very early in the day. Unlike those previous two cases, there was not a second event later on closer to the onset of the transition. This allows a different perspective to explore the lasting effects of a precipitation event and the impact on the transition. This event occurred at about midday and ended approximately 3 hours and 15 minutes prior to the onset of the transition.

The precipitation event on July 3 occurred at around 1500 local time when the boundary layer temperature was the warmest and surface fluxes are at their maximum. The impact of the precipitation event can be observed in some variables. For example, TKE decreased during the event and reached a local minimum soon after the event ended. However, the recovery of the surface layer and the boundary layer was quick and there was a long lead time to the start of the transition. Hence, the event had little impacts on the AET. It is worth noting that the impact of this convective event is different from other cases. The precipitation did not reduce the surface layer temperature or increase the surface layer moisture.

Unlike the previous cases, the precipitation did not contribute to any stabilizing effects to the boundary layer. Instead, the ABL remained unstable as seen in Figure 23 indicated by the persistent negative potential temperature gradient. This response associated with the background boundary layer condition since the precipitation occurred at the time of maximum surface heating in the early afternoon. Figure 24 shows clearly the unstable potential temperature gradient with increasing warming during this part of the day, as well as the large variance of vertical velocity between ~100-700 m above the surface. There is a slight decrease of wind speed during the event. However, any changes introduced by the short-lived precipitation event were quickly mixed out by the strong turbulence from surface forcing and the boundary layer recovered quickly after the event.
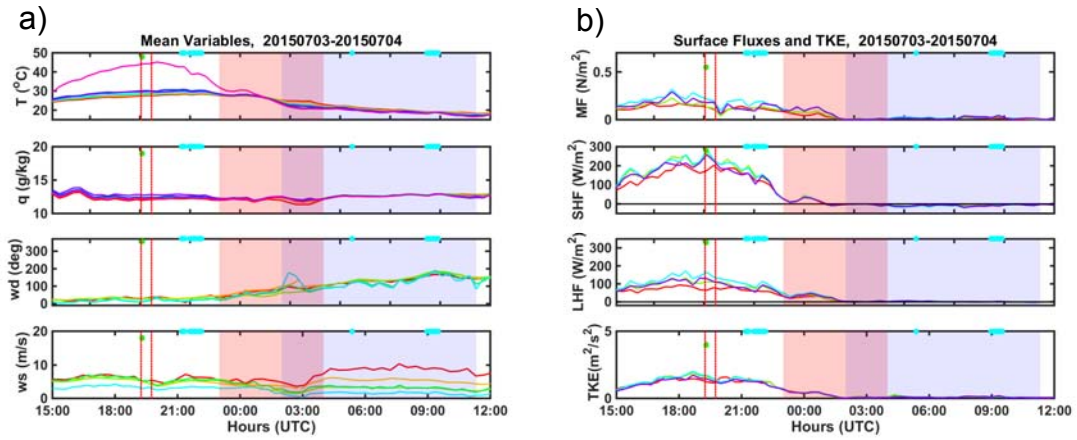
The temporal variations of a) observed mean temperature (T), specific humidity (q), wind direction (wd) and wind speed (ws) and b) observed fluxes during July 03 and 04, 2015. The red shading denotes the transitional period and the blue shading covers the night period defined between sunset and sunrise. The different lines in each subplot are indicated in Table 3.

Figure 22.   Temporal Variations of Mean Variables, Surface Fluxes and TKE July 03 and 04, 2015.
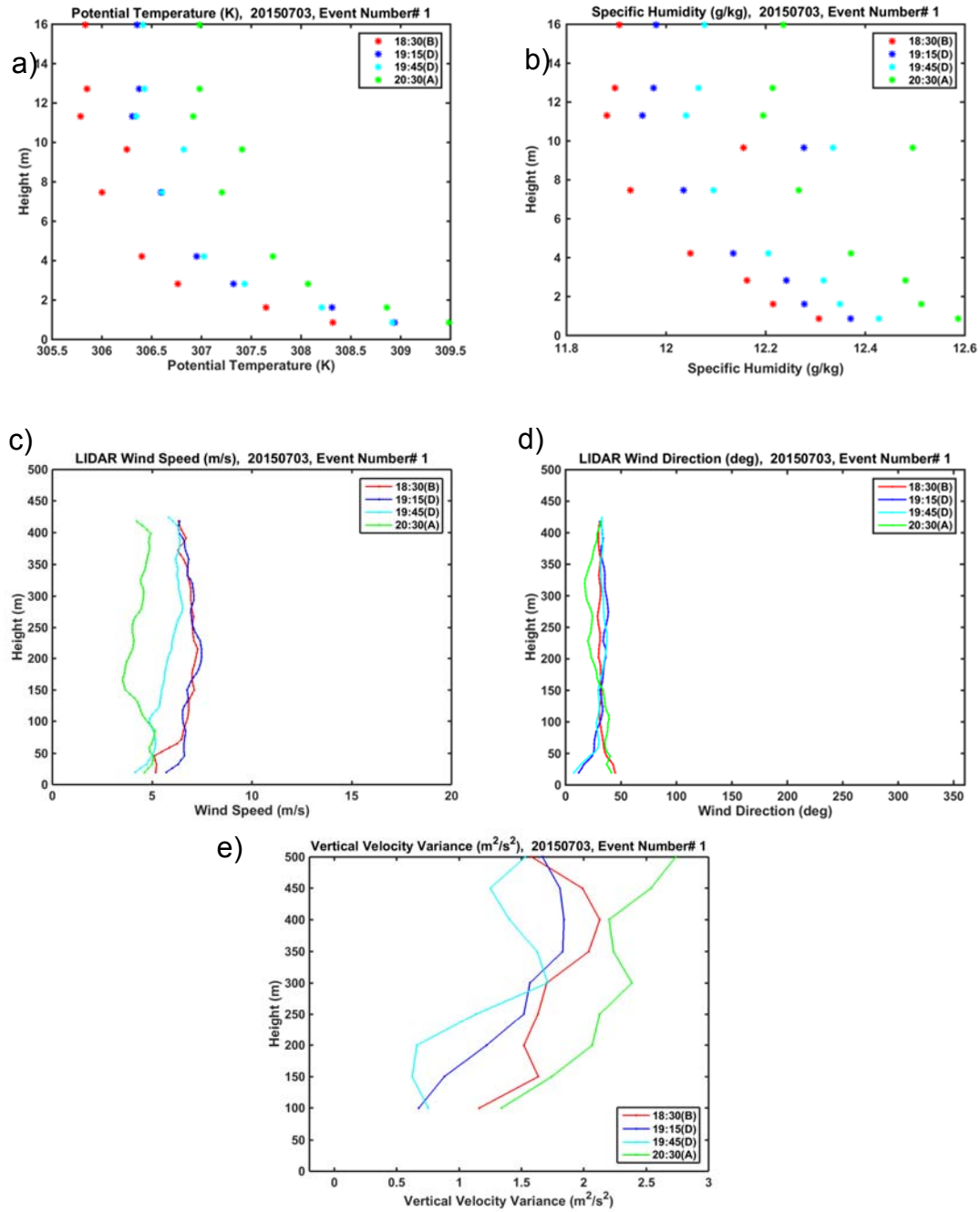
43

Measured vertical profiles from before (B), during (D), and after (A) the first precipitation event. Parameters include a) potential temperature, b) specific humidity, c) wind direction, d) wind speed, and e) variance of vertical velocity. The potential temperature and specific humidity are from the 16-m tower. The wind speed, wind direction, and vertical velocity variance in a deeper layer are from the wind LIDAR.

Figure 23.   Observed Surface Layer Profiles on July03 and 04, 2015.
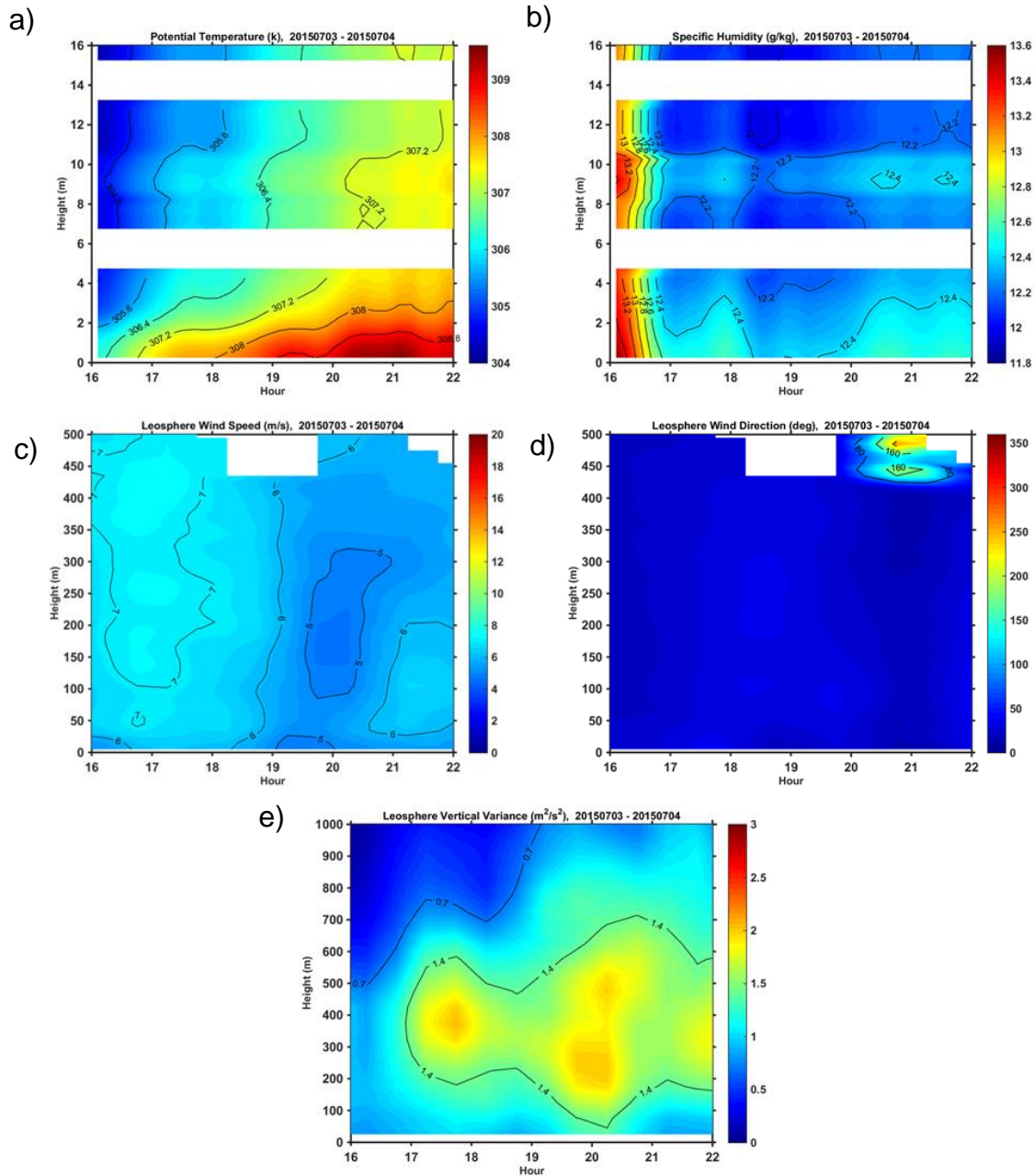
Time-height variations of (a) potential temperature, (b) specific humidity from the 16-m tower and (c) wind speed, (d) wind direction, and (e) variance of vertical velocity from the LIDAR.

Figure 24.   Time-Height Variations on July 03 and 04, 2015.

e.   *July 6, 2015*

The precipitation event of interest on July 6, 2015 occurs after the transition has already begun, from 0025–0045 UTC as highlighted in Figure 25.

This case allows us to examine how the onset of precipitation can impact the ongoing AET. The July 6 case is also unique due to the fact that there was low-level cloud cover for the majority of the day as denoted by the blue dots on the top of Figure 25. The presence of low-level clouds makes it hard to draw clear conclusions as to the specific effects caused by the precipitation. However, by comparing with the other precipitation cases discussed earlier, some characteristics continue to be observed during this event. Although small in magnitude, the decrease in temperature and increase in moisture are still observed and shown in Figure 25 although no apparent changes occurred in the wind. The impact on sensible and latent heat flux during the precipitation event was also observed with a decrease in sensible heat flux to the negative range and an increase in latent heat flux, which is consistent with those seen in a previous case on June 25 seen in Figure 14.
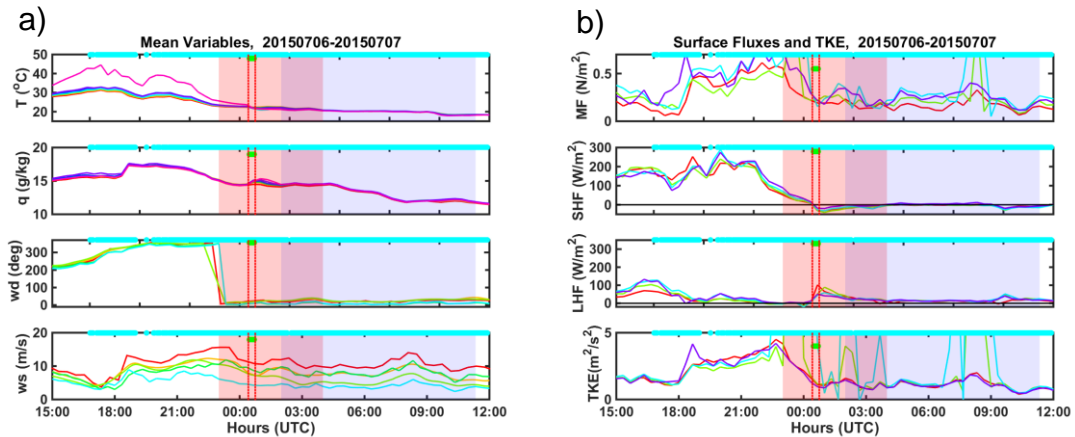

The temporal variations of a) observed mean temperature (T), specific humidity (q), wind direction (wd) and wind speed (ws) and b) observed fluxes during July 06 and 07, 2015. The red shading denotes the transitional period and the blue shading covers the night period defined between sunset and sunrise. The different lines in each subplot are indicated in Table 3.

Figure 25.   Temporal Variations of Mean Variables, Surface Fluxes and TKE July 06 and 07, 2015.

Potential temperature shown in Figure 26 depicts the evolution of the surface layer during the transition from unstable surface layer at 0030 UTC to

46

stable surface layer 0055 UTC. The specific humidity also shows slight moistening accompanied with the transition. Such transition is expected in the ideal case as discussed in Figure 6. However, in this case, the temporal variation above 6 m is less significant compared to the ideal case within the 1.5-hour period shown in the figure. Figure 27 shows a better time evolution associated with the event. Here, we can see that the cooling and overall drying due to the ongoing afternoon-to-evening transition. The precipitation event indeed introduced short-lived further cooling and slight moistening, both effects are likely insignificant because of the small magnitude. Meanwhile, the LIDAR measurements clearly indicated enhancement of the vertical velocity variance during the passing of the convective precipitation together with temporary reduction in wind speed, both occurred in the lowest 500 m of the boundary layer.
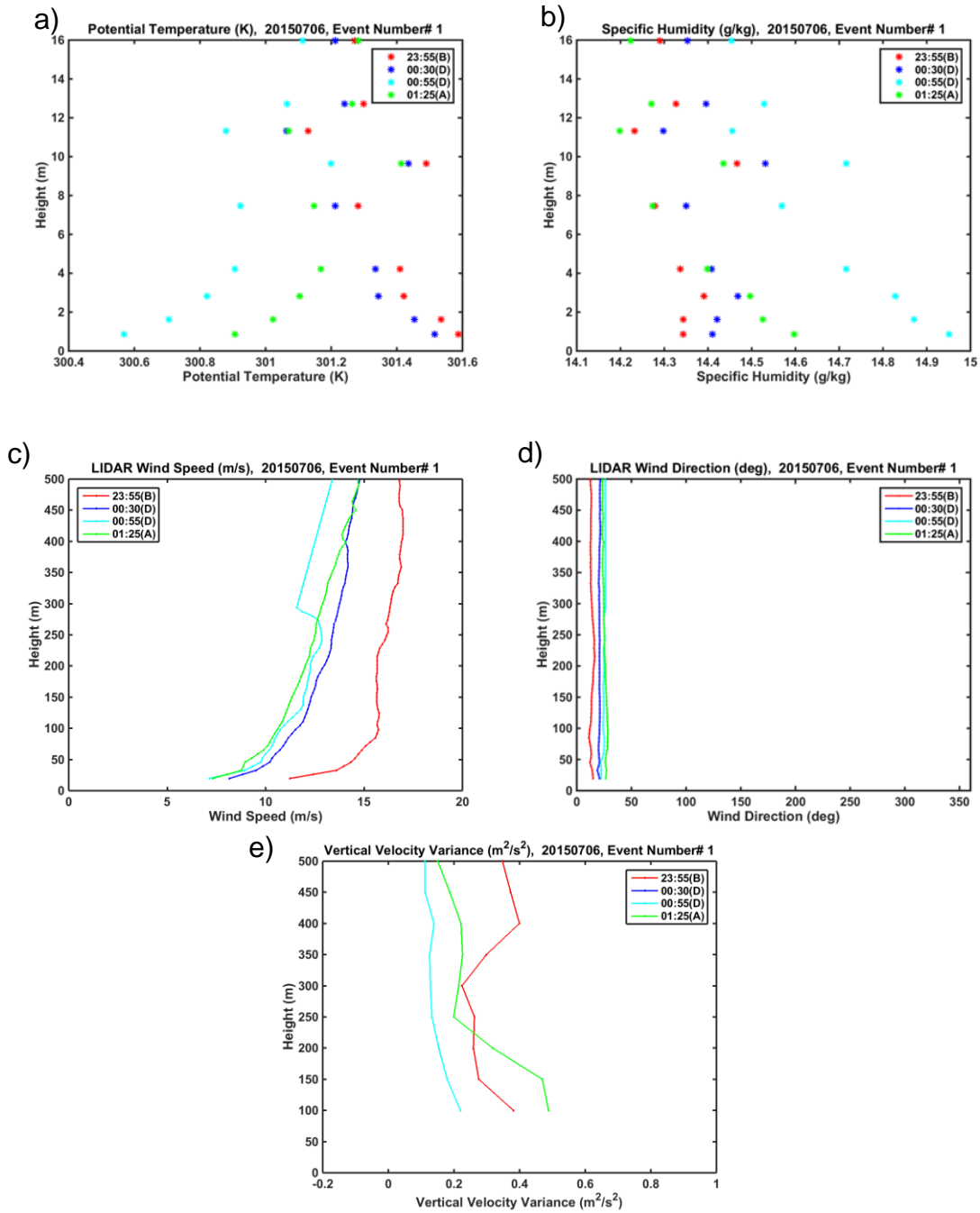
Measured vertical profiles from before (B), during (D), and after (A) the first precipitation event. Parameters include a) potential temperature, b) specific humidity, c) wind direction, d) wind speed, and e) variance of vertical velocity. The potential temperature and specific humidity are from the 16-m tower. The wind speed, wind direction, and vertical velocity variance in a deeper layer are from the wind LIDAR.

Figure 26.   Observed Surface Layer Profiles on July 06 and 07, 2015.
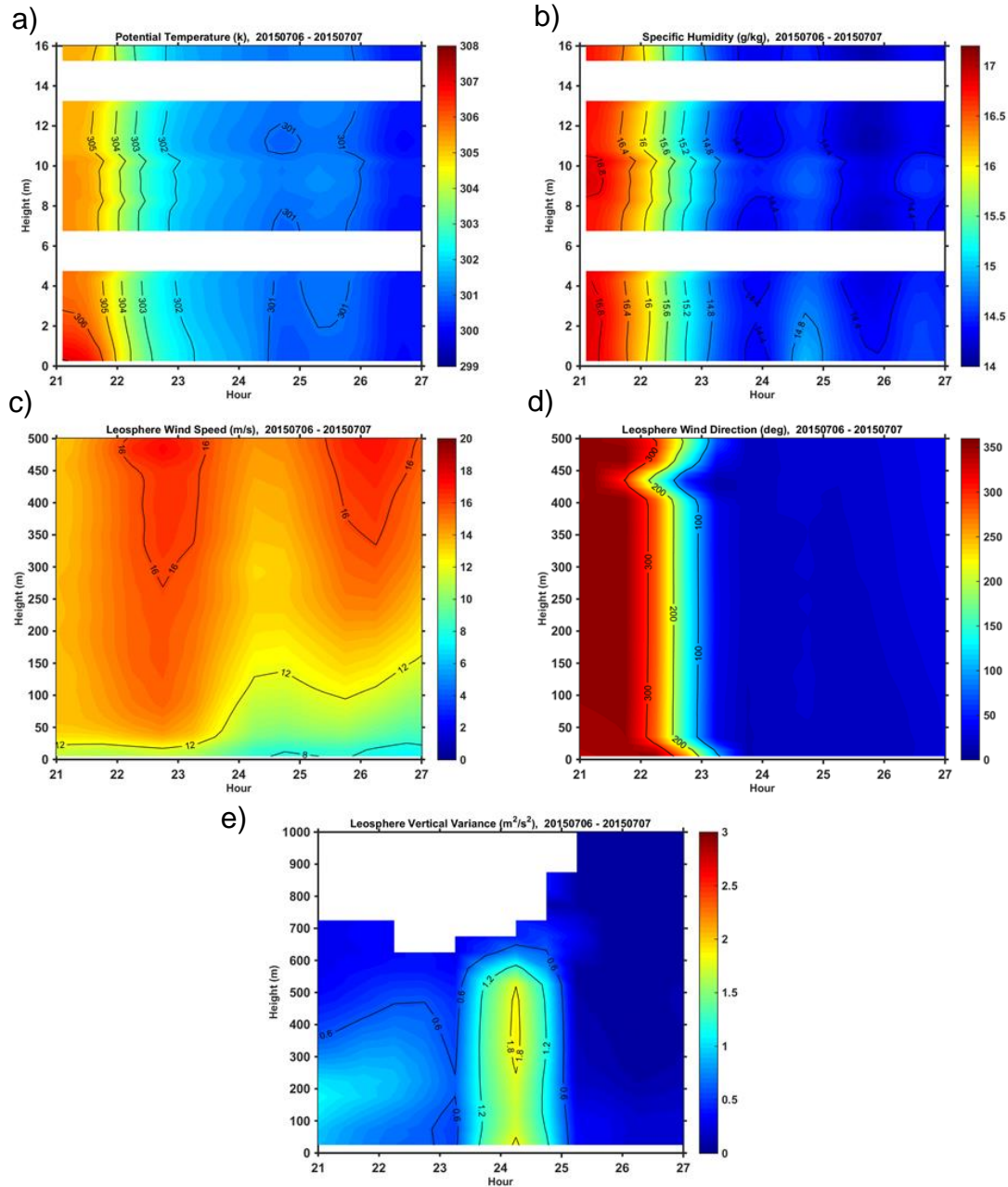
(a) Time-height variations of (a) potential temperature, (b) specific humidity from the 16-m tower and (c) wind speed, (d) wind direction, and (e) variance of vertical velocity from the LIDAR.

Figure 27.   Time-Height Variations on July 06 and 07, 2015.

f.   *Summary on Effects of Precipitation Events*

This chapter has examined a total of 7 precipitation events and their impact on boundary layer and surface layer wind, thermodynamic, and

49

turbulence structure. Whenever possible, their impact on AET was discussed. It is sufficient to say that each event is unique in some way depending on the specifics of the convective storm that generated the precipitation such as its intensity, area coverage, distance to the FP2 location, direction where the storm moves, etc. Due to the limited number of cases we observed for this study, we cannot further categorize based on these storm characteristics. Nevertheless, the observed boundary layer response to the precipitation events still shows some common characteristics. Table 4 summarizes the major properties of all events discussed in this chapter. It is clear from this table that most precipitation events resulted in cooling and moistening of the surface layer and increases in wind speed and turbulence. The events on July 3 and July 6, 2015 were both short-lived events compared to others. The event on July 3 also occurred during the warmest time of the day with strong surface buoyancy forcing.

Table 4. Summary of the Impact of Precipitation Events on Characteristics of the Boundary Layer.

Day (mmdd)	Time (UTC)	WS $\uparrow$	WD $\nearrow$ (V) or $\nwarrow$ (B)	$w^2\uparrow$	$T\downarrow$	$q\uparrow$	Flux $\uparrow$	TKE $\uparrow$
0614	1730	Yes	V	Yes	Yes	Yes	M,S	Yes
0614	0130	Yes	V	Yes	Yes	Yes	M,S,L	Yes
0625	0215	Yes	B	No	Yes	Yes	M,S,L	Yes
0702	1700	Yes	V	No	Yes	Yes	M	Yes
0702	2030	Yes	B	Yes	Yes	---	M	Yes
0703	1915	No	---	Yes	No	No	---	---
0707	0030	No	---	Yes	Yes	Yes	S,L	---

Here, the symbols $\uparrow$, $\downarrow$, $\nearrow$, and $\nwarrow$ denote 'increasing', 'decreasing', 'wind veering', and 'wind backing', respectively. 'M', 'S', and 'L' denote momentum flux, sensible heat flux, and latent heat flux, respectively.

3.   Effects of Cloud Cover Events on the Boundary Layer

The 4 cases discussed below are days in which clouds were associated with nearby convective activities. The impacts of these clouds on the boundary layer and AET will be examined. These cloud cover events occurred on June 14,

and July 3, 6, and 13, 2015. The first 3 days also had clouds with precipitation, which were discussed in the previous section of this chapter. The time periods selected here are cloud-only events.

a. June 14, 2015

June 14 was under persistent cloud cover almost for the entire day with two precipitation events discussed in the previous section. We particularly focus on the low-level clouds covered period between 1930 and 2030 UTC. Precipitation occurred before and after this time period, both precipitation events were discussed earlier. The time period selected for discussion overlaps the onset of the transition, which allows for a comparison of how clouds impact the transition. Figure 28 shows the temporal variations of all key variables for the two-day period. In comparison with Figure 6, it can be seen that the characteristics associated with the ideal transition were not observed. Notably temperature increases during the early transition period. This is likely due to the reduction of net outgoing infrared radiation due to the low-level clouds. Also notable are the greatly reduced sensible heat flux compared to the ideal conditions in Figure 6 (~200 Wm^{-2} vs 100 Wm^{-2} at about 2000 UTC), resulted from the less heated surface under clouds. The moisture flux, on the other hand, significantly increased to about 300 Wm^{-2}, an increase of nearly 100 Wm^{-2} from the ideal condition shown in Figure 6. It should be kept in mind, though, that these changes in surface fluxes may also be a result of other factors, such as wet surfaces from the previous rain event. We also notice that the negative sensible heat flux is very small in magnitude at the onset of the thermal stability change about 1 hour before sunset, clearly an indication of cloud cover reducing net infrared radiation loss. By the end of the clouds period of interest, the momentum flux, sensible heat flux and TKE remain approximately constant through the transition until the next precipitation period described in the previous section. The evolution of specific humidity exhibits similar characteristics as in the ideal transition around sunset.

51
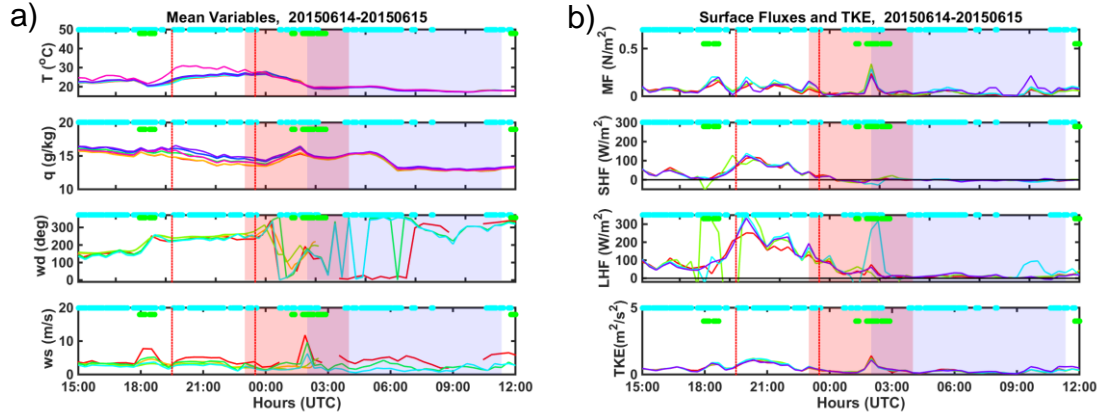
(a) The temporal variations of a) observed mean temperature (T), specific humidity (q), wind direction (wd) and wind speed (ws) and b) observed fluxes during June 14 and 15, 2015. The red shading denotes the transitional period and the blue shading covers the night period defined between sunset and sunrise. The different lines in each subplot are indicated in Table 3.

Figure 28.   Temporal Variations of Mean Variables, Surface Fluxes and TKE June 14 and 15, 2015.

Figure 29 depicts the evolution of the boundary layer under clouds using the time-height contour plots. The time period between two precipitation events experienced gradual wind direction veering until 0000 UTC with warming and significant drying at the same time. It is difficult to relate this variability to the presence of clouds itself. However, the evolution and movement of the convective system that brought the cloud and rain events should be the reason resulting in these changes.
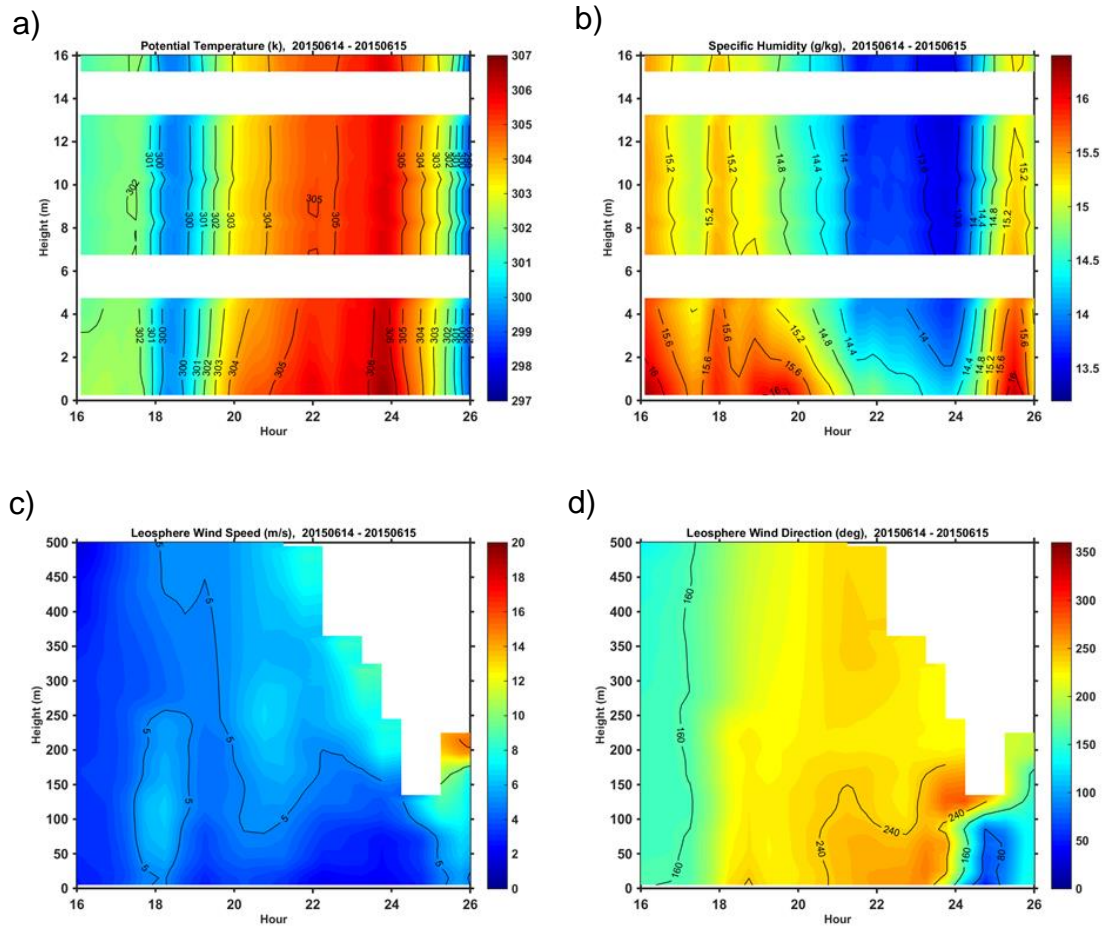
Time-height variations of (a) potential temperature, (b) specific humidity from the 16-m tower and (c) wind speed, and (d) wind direction from the LIDAR.

Figure 29.   Time-Height Variations on June 14 and 15, 2015.

b.   July 3, 2015

The convective low-cloud period of interest on July 3 was from 2100–2215 UTC. The proximity of this scenario to the onset of the transition allows an evaluation on how the transitional evolution is impacted by the presence of clouds before the transition. As with the case of June 14 discussed earlier in this section, the onset of the decline in temperature is delayed by 90 minutes from the presumed beginning of the transition. There is a similar delay in the decrease in low-level winds. Unlike in the ideal transition case as shown in Figure 6, the mean 425–600 m boundary layer wind (magenta line in wind speed plot) also decreases in synch with the surface layer wind after an initial increase around the

time when the surface layer became stable seen in the temperature plot in Figure 30. Enhancement of the boundary layer wind in all levels started at 0300 UTC on July 4, 2015, well into the nighttime. In comparison, the development of the LLJ started immediately after the surface layer stability became stable in the ideal transition case. Sensible and latent heat flux are reduced during the cloud cover period, although these evolutions appear to be consistent with the trend before the cloud event suggesting that they may be part of the "normal" diurnal variation. Similar to the case on June 14, the effects from the cloud cover was short-lived and have diminished after sunset, which can be seen in the time series plot of the observed mean thermodynamic variables, wind speed and direction, surface fluxes and TKE in Figure 30.
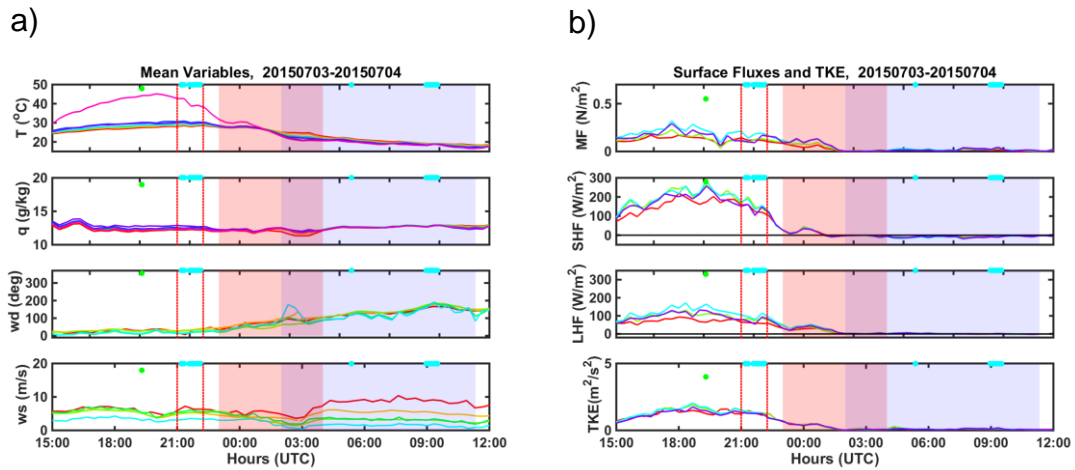
The temporal variations of a) observed mean temperature (T), specific humidity (q), wind direction (wd) and wind speed (ws) and b) observed fluxes during July 03 and 04, 2015. The red shading denotes the transitional period and the blue shading covers the night period defined between sunset and sunrise. The different lines in each subplot are indicated in Table 3.

Figure 30.   Temporal Variations of Mean Variables, Surface Fluxes and TKE July 03 and 04, 2015.

The effect of the low clouds in this case is likely in the delay of the expected decrease of the temperature. The downward infrared radiation from the low-level clouds reduced the net radiation loss from the surface and hence helps keep the lower atmosphere warmer, and specifically in this case delays the onset

of the expected transitional cooling from taking place. This confirms results from previous research that cloud cover can prevent a rapid transition from occurring.

It is worth emphasizing that the events of cloud cover are normally associated with some type of convection system. The example shown here is no exception. Figure 30 shows precipitation was identified at around 2000 UTC before the cloud event. The vertical velocity variance in Figure 31 shows the enhanced w variance started before 1800 UTC, and was particularly strong around 2000 UTC. The large w^2 variance in Figure 31 hence should be the diurnal flux variation modulated by the convective event. During the cloud event between 2100–2200 UTC, there is a slight increase in wind speed in the boundary layer while the surface layer is warmer and moister as seen in the 16-m tower measurements above ~ 4m.
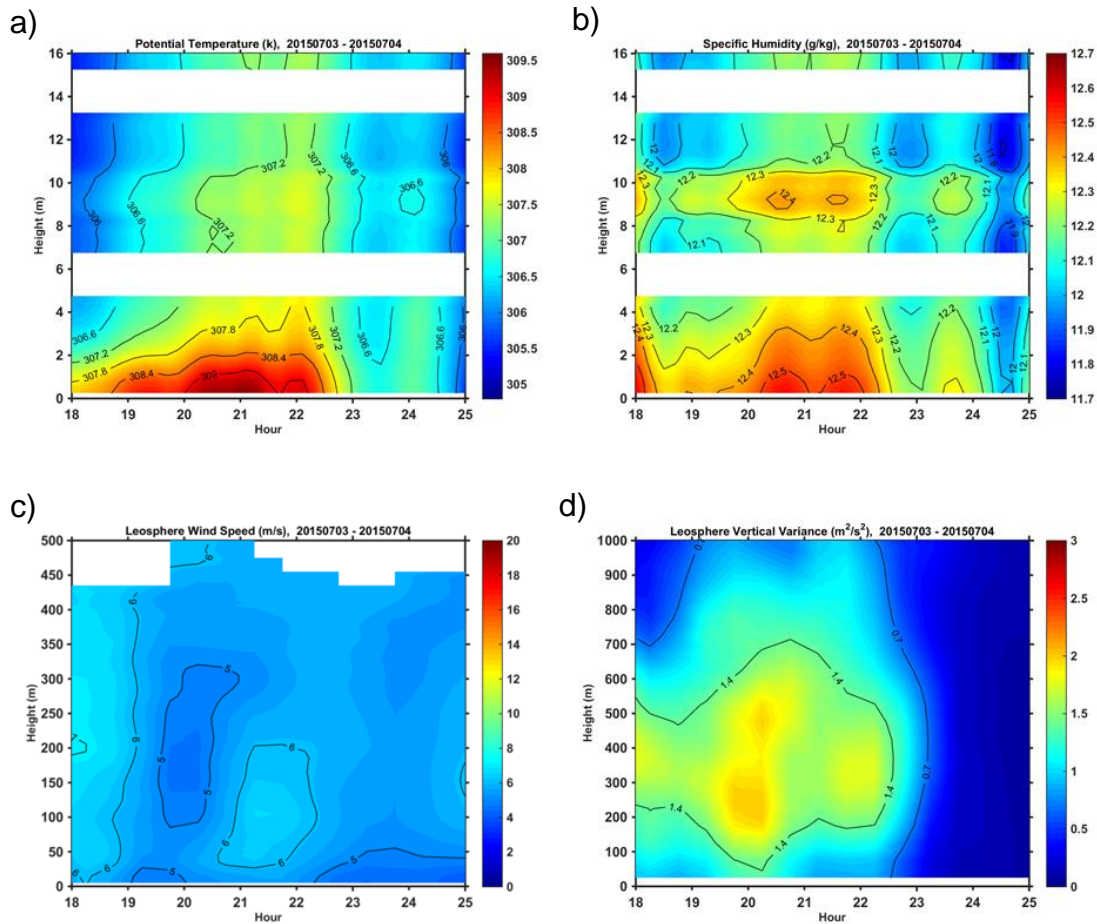
Time-height variations of (a) potential temperature, (b) specific humidity from the 16-m tower and (c) wind speed, and (d) variance of vertical velocity from the LIDAR.

Figure 31.   Time-Height Variations on July 03 and 04, 2015.

c.   July 6, 2015

July 6, 2015 was under low clouds over the course of the day with a 1-hour break from 1900–2000 UTC. The initial 2.5 hour of cloud coverage introduced the most significant changes to the boundary layer as depicted in both Figures 32 and 33. The decrease in surface temperature around local noon corresponding to the onset of the cloud cover is apparently a result of the clouds. This period is also shown to have wind veering gradually from westerly to northerly while wind speed decreased slightly at the beginning and increased rapidly after 1800 UTC. Surface layer moisture seemed to sync up with the wind

speed. The evolution describe above is best seen in the time-height contour plots shown in Figure 33 which suggests a strong warm convective updraft passed over FP2 as indicated by the w^2 profiles. The w^2 variation also reveals enhanced turbulence levels behind the updraft with small magnitude in the undulations. The updraft occurred between 1530 and 1730 UTC corresponding to a wind speed local minimum and the wind direction veering from southwesterly to northerly, consistent with convergence of the low-level wind. The updraft is thus likely the outflow front. This updraft has a very sharp boundary with the air behind being much more moist and colder.

The temporal variations of a) observed mean temperature (T), specific humidity (q), wind direction (wd) and wind speed (ws) and b) observed fluxes during July 06 and 07, 2015. The red shading denotes the transitional period and the blue shading covers the night period defined between sunset and sunrise. The different lines in each subplot are indicated in Table 3.

Figure 32.   Temporal Variations of Mean Variables, Surface Fluxes and TKE July 06 and 07, 2015.
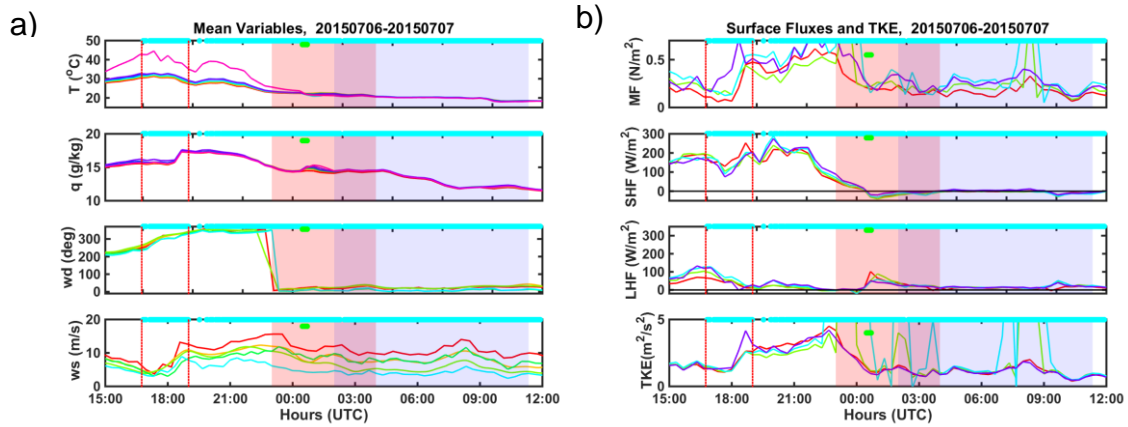
Time-height variations of (a) potential temperature, (b) specific humidity from the 16-m tower and (c) wind speed, (d) wind direction, and (e) variance of vertical velocity from the LIDAR.

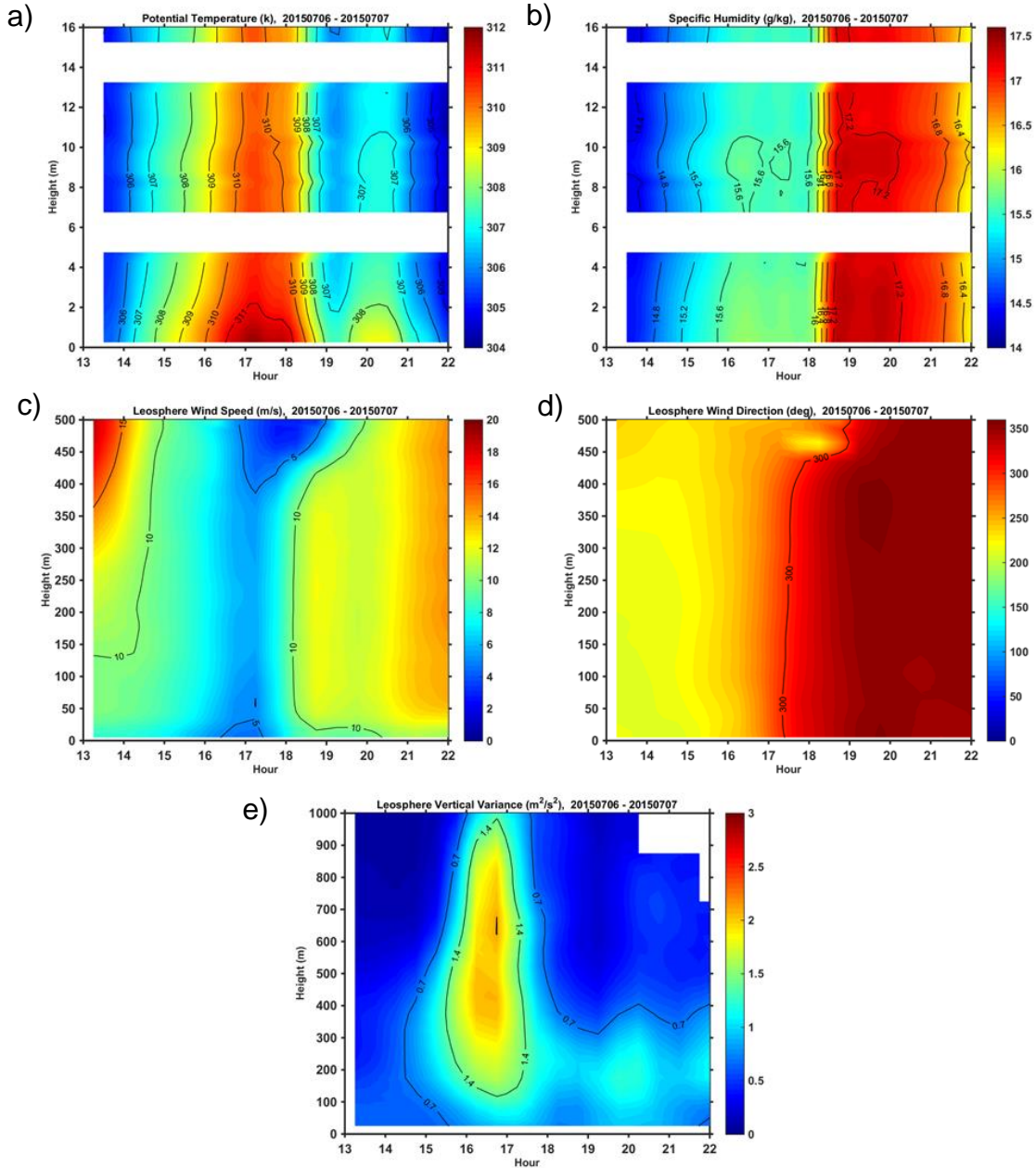Figure 33.   Time-Height Variations on July 06 and 07, 2015.

d.   *July 13, 2015*

On July 13, FP2 was affected by cloud clover associated with a nearby complex of thunderstorms to the southwest of FP2. These clouds were overhead

from 0055–0140 UTC and occurred after the start of the expected transitional period. Comparing Figure 34 to 6, the differences in both the surface flux and mean surface observations are evident. There was a very sharp increase in specific humidity, and a spike in latent heat flux not present in the ideal case. The impact of the thunderstorm complex that arrived at FP2 around 2330 UTC was a sudden increase of wind speed, veering of wind direction, and a sudden increase of water vapor. This continues until 0600 UTC the next day when the wind is back to northerly and the air at FP2 has become drier. The cloud cover however is only seen during a short period as depicted be the dash lines in Figure 34. The present of this cloud patch introduced further moisture increase, signaling the arrival of a more moist section of the thunderstorm. The changes in temperature and water vapor likely contributed to a temporary enhancement of sensible and latent heat fluxes, while increases in the surface momentum flux and TKE are not apparent. Figure 35 shows a strong updraft and turbulence at the onset of the cloud cover that filled the lowest 400 m of the boundary layer. The development of a low-level jet can be seen on the wind speed contour plot. This LLJ centered at about 250 m above the ground and reached its peak value at around 0130 UTC. The LIDAR wind speed does not show significant wind increase at the surface level associated with the wind maximum at 250 m, except the initial increase around 0000 UTC. This is consistent with the low-level wind observation in Figure 34. This is a case where the AET is heavily disturbed by the passing convection. We do observe that the onset of the nocturnal stable boundary layer is not changed seen Figure 34 with temperature specifically.

The temporal variations of a) observed mean temperature (T), specific humidity (q), wind direction (wd) and wind speed (ws) and b) observed fluxes during July 13 and 14, 2015. The red shading denotes the transitional period and the blue shading covers the night period defined between sunset and sunrise. The different lines in each subplot are indicated in Table 3.

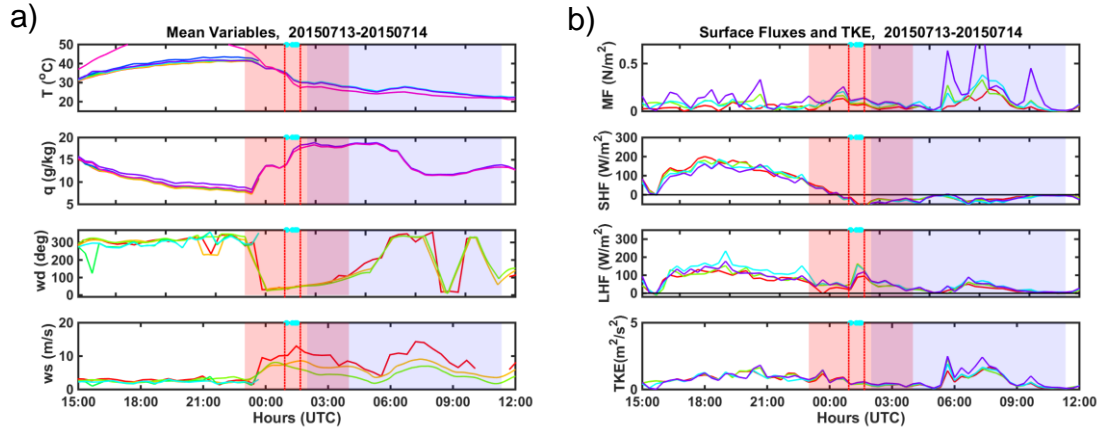Figure 34.   Temporal Variations of Mean Variables, Surface Fluxes and TKE July 13 and 14, 2015.

Time-height variations of (a) wind speed, (b) wind direction, and (c) variance of vertical velocity from the LIDAR.

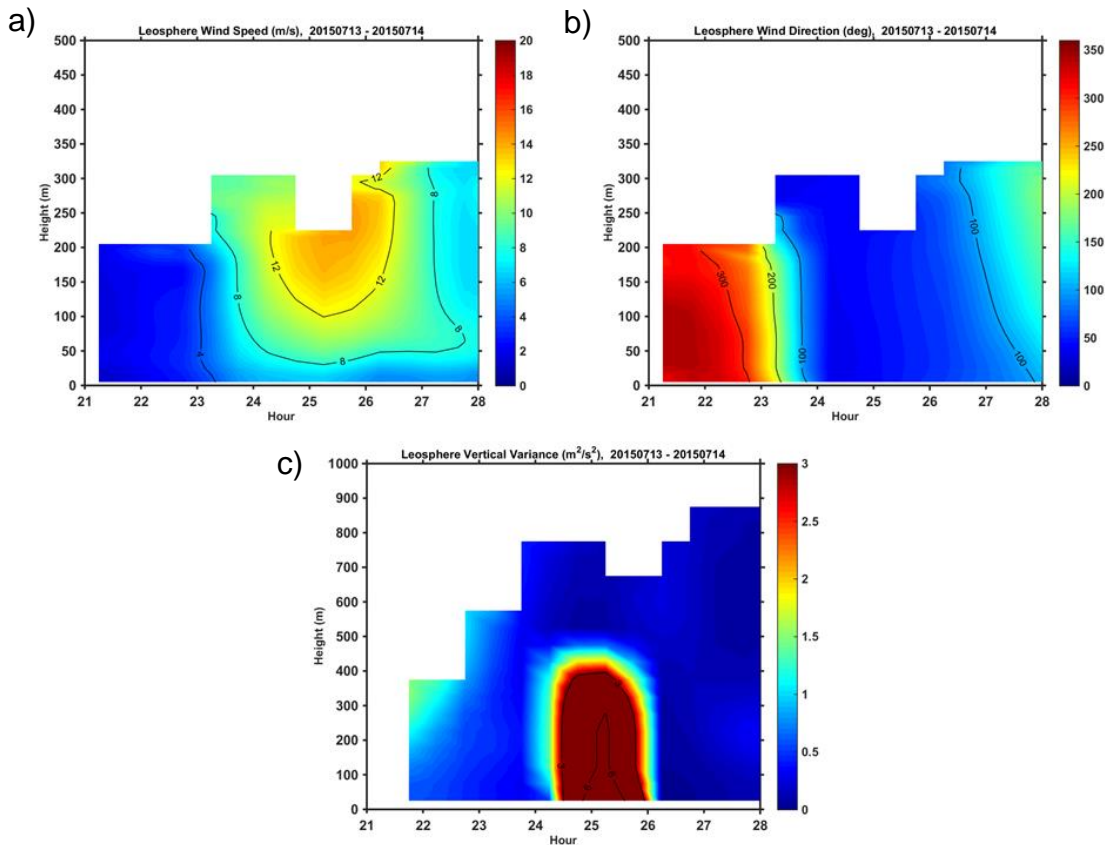Figure 35.   Time-Height Variations on July 13 and 14, 2015.

4.   Other Convective Events

There are two cases, on June 28 and 29, 2015, that met the initial criteria of convection within 30 nautical miles of FP2, yet lacked either of the criteria used to identify the previous two groups. These two cases are examined in this section. Although no precipitation or clouds directly affected FP2, nearby convective features played a role in boundary layer processes and was measured at FP2. The impacts of each case on the AET will be discussed.

a.   June 28, 2015

On June 28, 2015, a complex of thunderstorms was observed to the west of FP2. This case is unique in that the convection was nearly stationary and

neither clouds nor precipitation from the convective event passed over FP2, however the storm outflow boundary remained overhead for an extended period of time, as the thunderstorms and the associated outflow boundary at the surface were stationary. The time period of interest was from 2200–0000 UTC of the next day and is annotated by the red box in Figure 36. This boundary passed through FP2 shortly after sunset and is evident in the mean surface observations. A second period just after 0200 UTC is associated with the storm passage and is also of interest in this case. After the arrival of the outflow boundary, the boundary acted to inhibit the AET. This is observed in all features on Figure 36. Typical features are observed to include an increase in moisture just before a wind shift and slightly increased winds. These changes in wind speed and direction aid in the production of TKE through increased vertical shear observed just after the boundary passage.
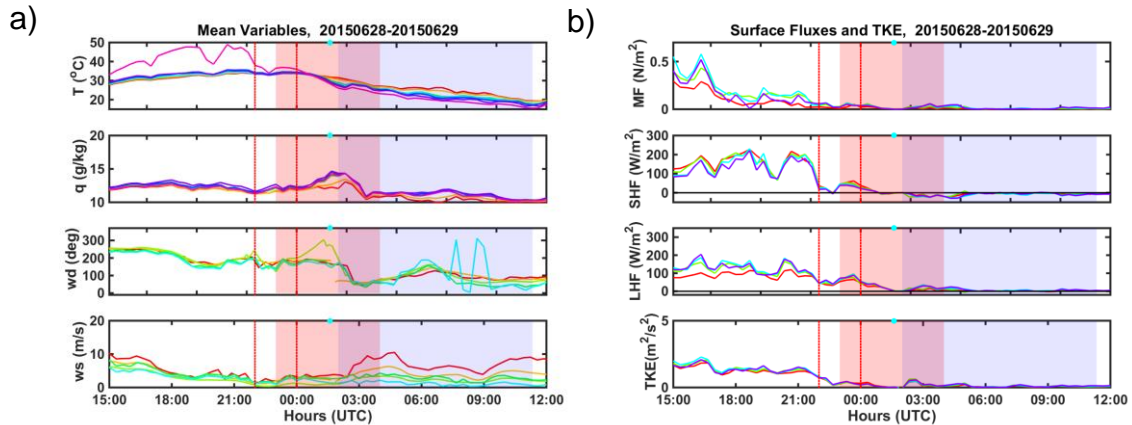
a)   b)

The temporal variations of a) observed mean temperature (T), specific humidity (q), wind direction (wd) and wind speed (ws) and b) observed fluxes during June28 and 29, 2015. The red shading denotes the transitional period and the blue shading covers the night period defined between sunset and sunrise. The different lines in each subplot are indicated in Table 3.

Figure 36.   Temporal Variations of Mean Variables, Surface Fluxes and TKE June 28 and 29, 2015.

Temporal variations seen in Figure 37 are centered on the event from 2200–0000 UTC; however, the frontal passage can be seen on the contour plot

involving a longer time period. Figure 37 show some of the features that are consistent with the precipitation cases although precipitation did not occur at FP2 in this case. Namely, the nearby convection stabilized the surface layer as depicted by the easing of the negative gradient in potential temperature. Also consistent is the increase in the near surface moisture and the moisture gradient. This is likely due to the moisture convergence in the outflow. Wind shift and increase with height is also reduced as the convection dissipates, also likely a result of the outflow and the associated mixing as evident in vertical velocity variance in Figure 38. The stabilization is also evident as the daytime turbulence dissipated as depicted by vertical velocity variance. Figure 38 depicts these features as well as the onset of the boundary passage at time 26–27. The drastic increase in moisture and decrease in temperature is readily evident as is the wind shift and increase in winds in the lowest 250 meters.
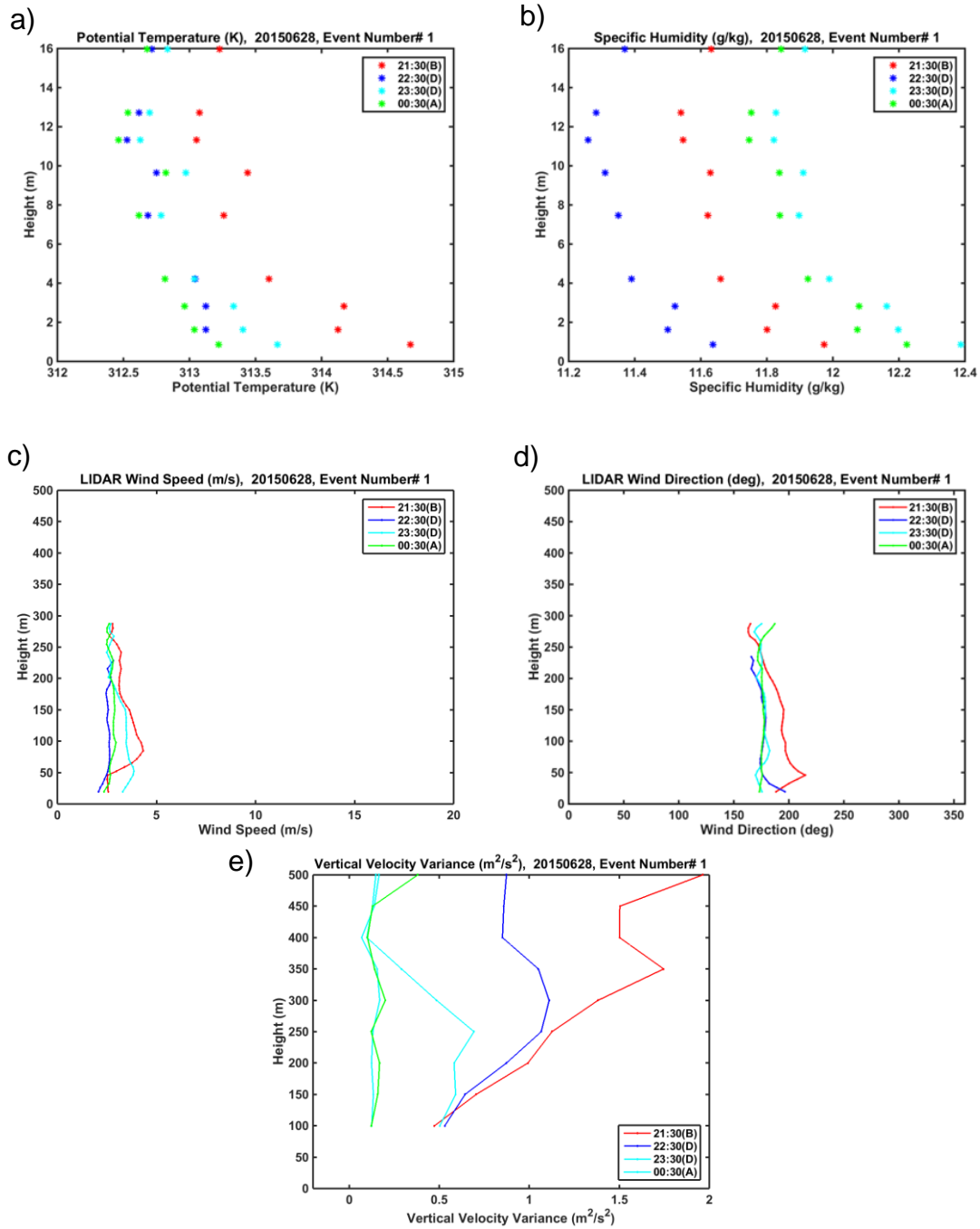
Measured vertical profiles from before (B), during (D), and after (A) the first precipitation event. Parameters include a) potential temperature, b) specific humidity, c) wind direction, d) wind speed, and e) variance of vertical velocity. The potential temperature and specific humidity are from the 16-m tower. The wind speed, wind direction, and vertical velocity variance in a deeper layer are from the wind LIDAR.

Figure 37.   Observed Surface Layer Profiles on June 28 and 29, 2015.
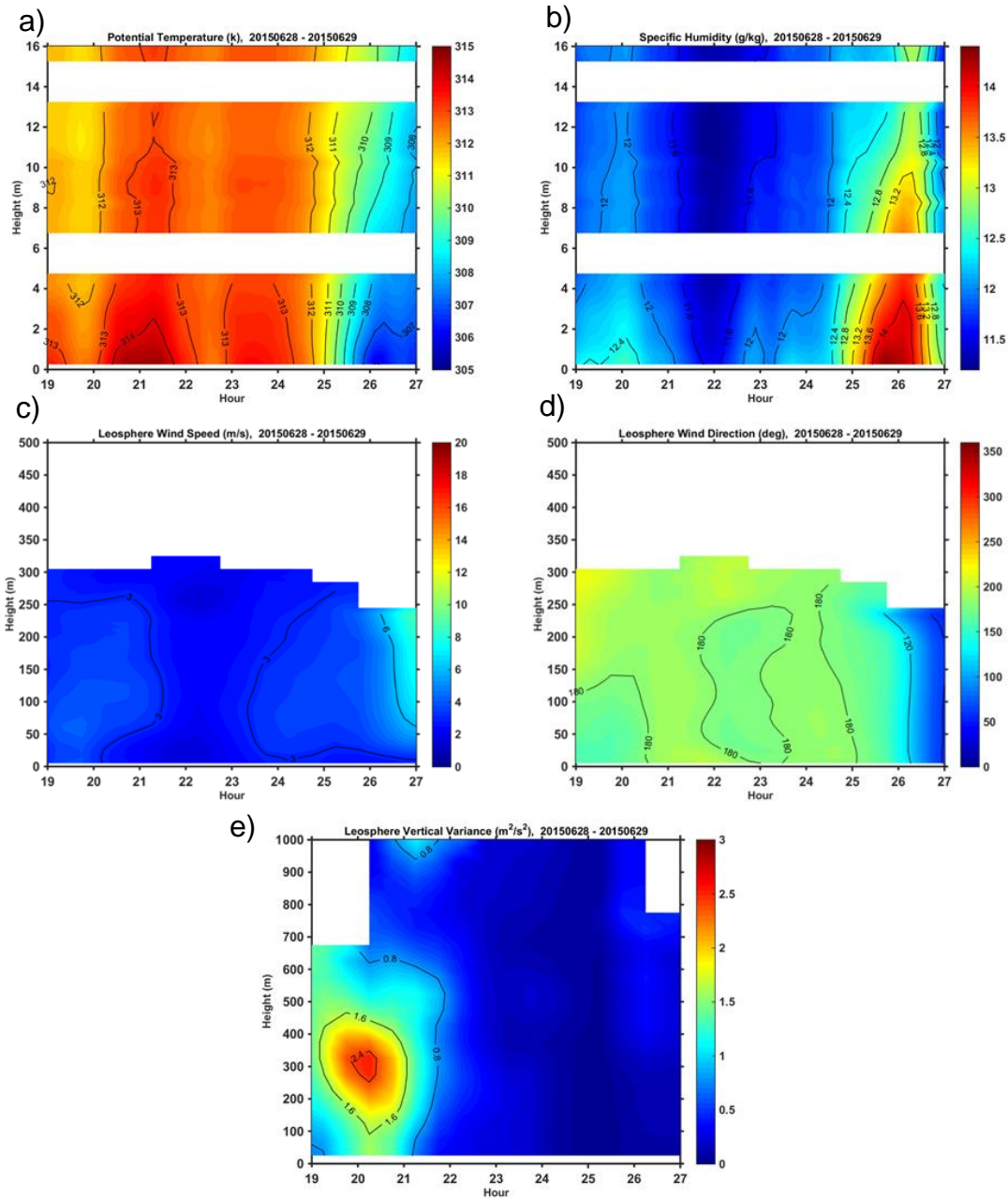
Time-height variations of (a) potential temperature, (b) specific humidity from the 16-m tower and (c) wind speed, (d) wind direction, and (e) variance of vertical velocity from the LIDAR.

Figure 38.   Time-Height Variations on June 28 and 29, 2015.

b.   June 29, 2015

The case of June 29 involved an outflow boundary passing over FP2 at 0200 UTC. This outflow boundary originated from a convective thunderstorm that

was to the west of FP2, but outside of the 30nm in which this thesis defined as nearby convection. The passage of the outflow boundary was observed both on radar and with the instruments at FP2.

Figure 39 shows the passage of the boundary with a solid red line. This boundary passed through after the onset of the transition. Prior to the boundary passage, there were relatively calm conditions seen at FP2. Despite these calm conditions, not all of the transition characteristics one would expect to observe during an ideal transition took place. There was a noticeable decrease in the temperature that is expected as part of the diurnal variation. There was also the pronounced increase in surface moisture at sunset. However, due to the timing of the outflow boundary passage, this increase cannot be solely attributed to the AET alone. This case differs from the ideal transition in the observed surface flux and winds. The pronounced decrease in surface winds does not occur at the transition onset. During an ideal transition as seen in Figure 6 there is a noticeable almost sine-like decay of both sensible and latent heat flux. This is not observed in the latent heat flux during this case. As the outflow boundary passes, it causes a sudden increase in winds, which contributes to an increase in both TKE from the shear generation, as well as an increase in momentum flux. This increase in TKE and momentum flux changes were not observed during ideal AET scenarios.
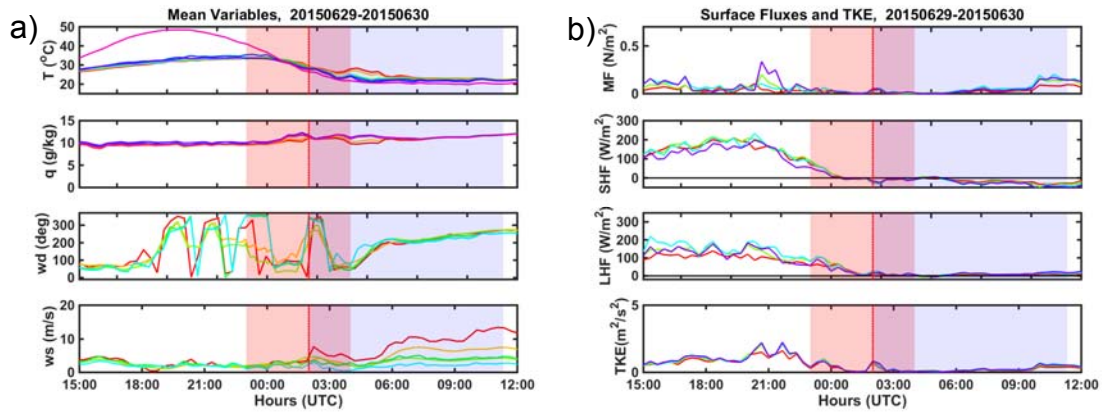
The temporal variations of a) observed mean temperature (T), specific humidity (q), wind direction (wd) and wind speed (ws) and b) observed fluxes during June 29 and 30, 2015. The red shading denotes the transitional period and the blue shading covers the night period defined between sunset and sunrise. The different lines in each subplot are indicated in Table 3.

Figure 39.   Temporal Variations of Mean Variables, Surface Fluxes and TKE June 29 and 30, 2015.

Figures 40 and 41 depict the vertical profile of the surface observations during the passage of the outflow boundary. The passage of the boundary cools the near surface temperature, increases both the near surface moisture, and near surface moisture gradient. The lower level wind shift and increasing winds with height is also readily apparent. The contour plot in Figure 41 allows for easy observation of both the pre- and post- outflow passage, which occurs at hour 26. The wind peaks at around 100 m with shear in the lowest 40 meters as well as the increase in near surface moisture both immediately before and after the outflow boundary. Slight enhancement of vertical velocity variance was also observed at the time of the outflow passage.
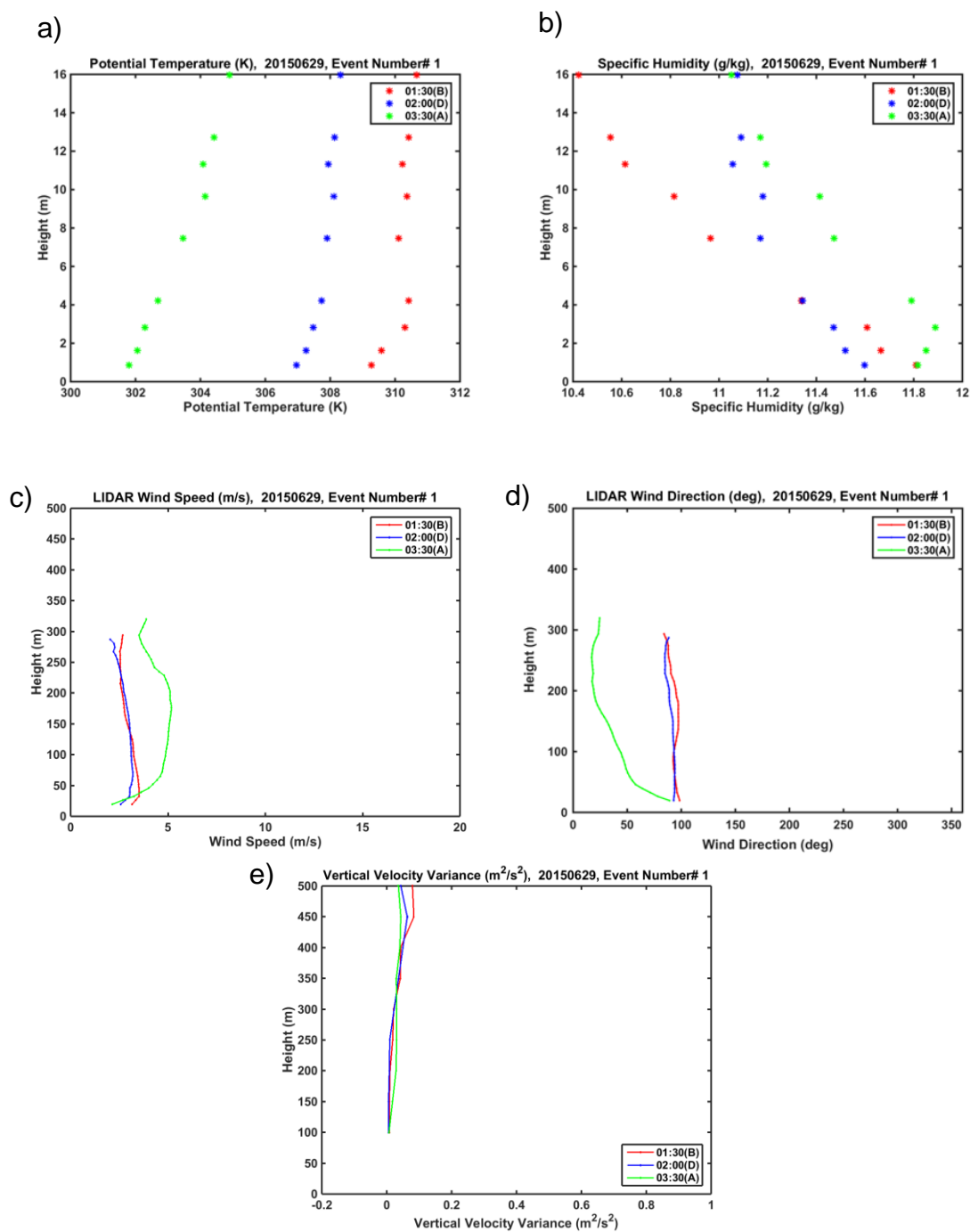
Measured vertical profiles from before (B), during (D), and after (A) the first precipitation event. Parameters include a) potential temperature, b) specific humidity, c) wind direction, d) wind speed, and e) variance of vertical velocity. The potential temperature and specific humidity are from the 16-m tower. The wind speed, wind direction, and vertical velocity variance in a deeper layer are from the wind LIDAR.

Figure 40.   Observed Surface Layer Profiles on June 29 and 30, 2015.
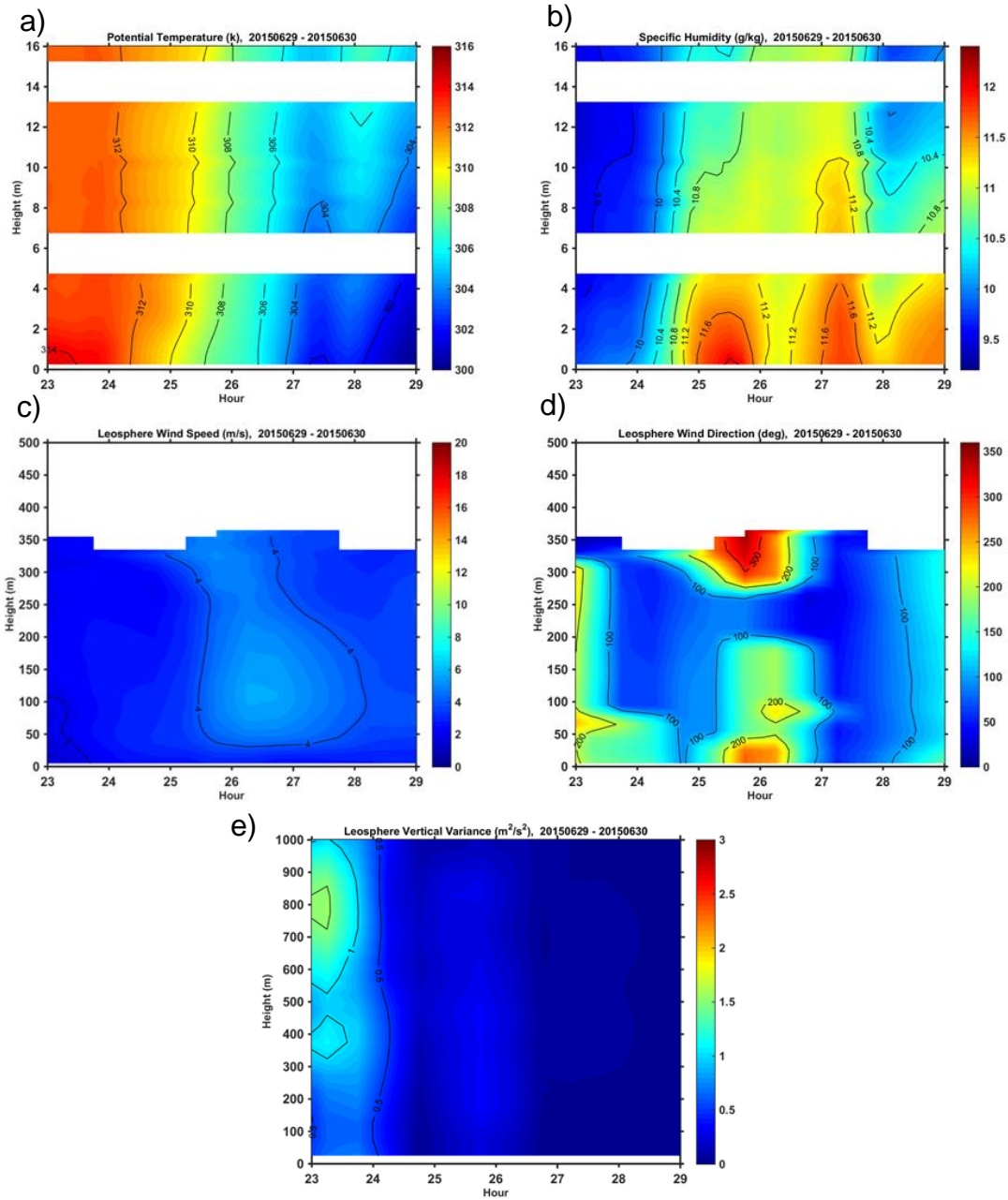
Time-height variations of (a) potential temperature, (b) specific humidity from the 16-m tower and (c) wind speed, (d) wind direction, and (e) variance of vertical velocity from the LIDAR.

Figure 41.   Time-Height Variations on June 29 and 30, 2015.

D.   COARE BULK FLUX PARAMETRIZATIONS

As discussed in chapter II, the COARE surface flux parametrization is the state-of-art surface flux schemes in mesoscale models and is used in the Navy's

69

COAMPS model. This subsection examines how well the modified parametrization scheme handles the surface fluxes during convective precipitation and cloud events. To examine this, the observed momentum, sensible and latent heat flux were compared to the COARE outputs of the same flux parameters.

The COARE algorithm requires inputs of mean wind speed, temperature, relative humidity and pressure at a single or multiple levels. For over the water applications, sea surface temperature is also a required input while surface specific humidity is obtained by assuming 98% saturation at the salt water surface. In this case, the mean wind was measured at 11.5 m above ground level (AGL), other variables were from measurements at 9.65 m AGL.

1. Obtaining Surface Roughness

For COARE to be used on land, we modified the original algorithm to use a constant surface roughness that is an input variable. For the FP2 site in Kansas, we searched for the climatological surface roughness height used in the Navy's COAMPS model for the latitude and longitude of FP2 and in the month of June/July. The climatological roughness height was found to be 0.25m. This is the mean surface roughness for an area of 1 km on the side near FP2 as the climatological data has a horizontal grid resolution of 1 km. This roughness was found to generate a very large momentum flux representing significant overestimate of this quantity when we compare the COARE calculated momentum flux with the momentum flux directly calculated from the high-rate sampled data using the eddy correlation method observed in Figure 42a.

a)
Observed MF vs COARE MF

b)
Observed MF vs COARE Calculated z_0 MF
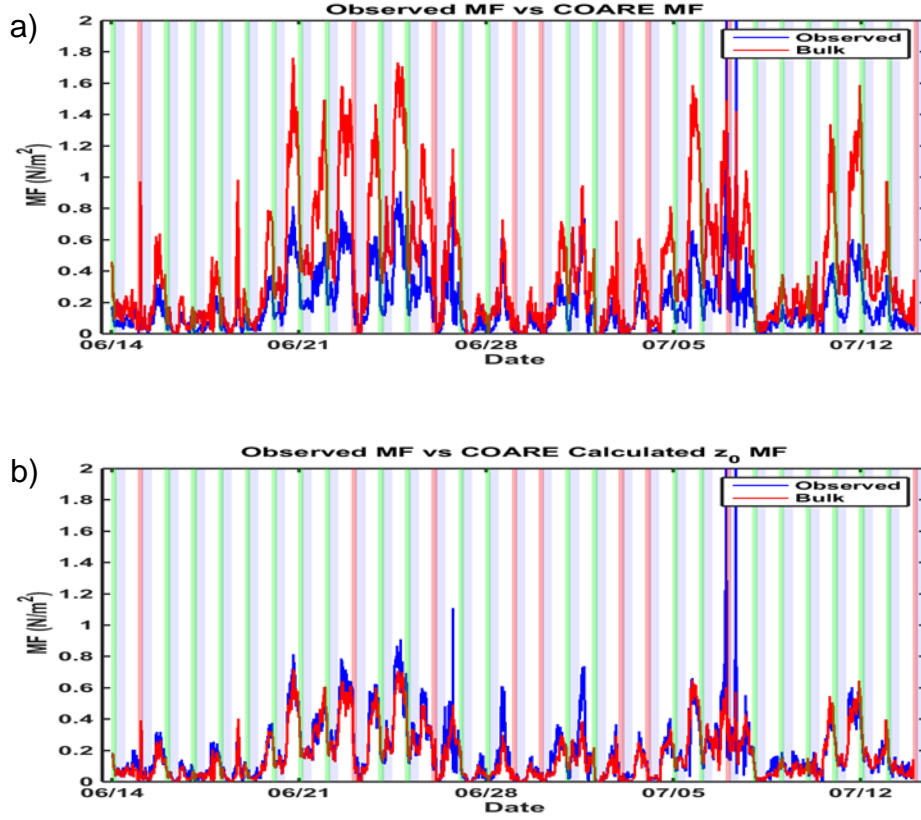
A comparison of momentum flux calculated using the climatological mean roughness value of 0.25m for FP2 in the summer with those derived from high-rate measurements of wind components; b) same as in a) except using a roughness length value of 0.05 m derived from observations. The green shading denotes non-convective event transitions, while the red shading represents transitions with days in which convective events occurred.

Figure 42.   Comparison of Momentum Flux with Surface Roughness Parameter Calculated.

To identify a reasonable surface roughness length at FP2 for the time period of measurements, we used the observations of the fluxes and the mean quantities to calculate z_0 based on Monin-Obukhov Similarity Theory (MOST). The following outlines the method used in this thesis.

By definition the frictional velocity u_* can be calculated based on Equation (1).

$$u_*{}^2 = -\overline{w'u'} \qquad (1)$$

71

From Equation (1), u_* is derived by taking the square root of the surface stress and divided by air density.

$$L = -\frac{u_*^3}{k\frac{g}{\theta}\overline{w'\theta'}} \qquad (2)$$

The Monin-Obukhov length scale, L is then calculated using u_*, the Von-Karman constant, k=0.4, and the calculated flux of potential temperature (θ), both were directly derived from the measurements at FP2. The next step of the derivation is depicted in Equation (3) using the mean wind equation.

$$U(z_s) = -\frac{u_*}{k}\ln\left[\frac{z_s}{z_0} - \psi_m\left(\frac{z_s}{L}\right)\right] \qquad (3)$$

where z_s is a reference level where mean wind measurements were made (z_s=11.5 m). The term, $\psi_m\left(\frac{z_s}{L}\right)$, is the integrated form of the empirical stability function, representing the stability correction. From Equation (3), z_0 can be expressed in Equation (4). Using the measured values of the mean wind and fluxes, mean surface roughness at FP2 during the measurement period was found to be 0.05 m. This is only 20% of the climatological value used in COAMPS.

$$z_0 = \frac{z_s}{\exp\left(-\frac{kU(z_s)}{u_*}\right) + \psi_m\left(\frac{z_s}{L}\right)} \qquad (4)$$

The z_0 of 0.05 m derived from the measurements was used as input to COARE over the course of the experiment during June 14-July 15, 2005 and the corrected COARE momentum flux is shown in Figure 42b. After this correction, Figure 42b shows much more realistic outputs by the COARE algorithm. It can be seen that during the day the momentum flux is consistently under forecast, however the error in this is rather small, particularly in comparison to Figure 42a. The rest of this chapter will used the adjusted z_0 values when using the COARE parameterization scheme.

Surface temperature is another variable as input to COARE scheme. In PECAN, we measured soil temperature at three depths: 5, 10 and 25 cm below the surface. We also used the irradiance measurements from a downward

looking infrared radiometer and derived surface temperature by assuming that the surface is a blackbody. For calculating the surface flux, we used a mean soil temperature that was computed as the average temperature from the four temperature values at the surface, and at 5, 10 and 25 cm below the surface.

Soil moisture was measured at two levels, 10 and 25 cm below the surface. Unfortunately, no calibration was made to this sensor. Hence the variability is likely more realistic than the absolute values. Initial moisture flux calculation using the uncorrected soil moisture showed a consistent bias in the output latent heat flux. We tested different values of a "bias" in soil moisture. An adjustment of the soil moisture by 0.25 seems to yield the most reasonable overall LHF. It is believed this is likely the bias of the sensor and this correction was used in the subsequent calculations.

Finally, the roughness for temperature (z_{0T}) and specific humidity (z_{oq}) in COARE were also modified to be consistent with COAMPS. Both of these scalar roughness length were set to 0.1 of the momentum roughness length (z_o).

2. COARE Evaluations

Figure 43 shows the comparison of the resultant SHF and LHF in comparison with the measurement derived respective fluxes. In general, COARE SHF and LHF compare reasonably well although there is clear underestimates in the midday and night for the magnitude of the sensible heat fluxes. The latent heat flux comparison does not show constant bias. The comparisons are best seen in the scatter plots in Figure 44. The momentum flux seems to compare the best among all three fluxes where the data points are centered around the 1:1 line. The sensible heat flux shows the trend well except with a nonlinear bias. In the stable regime, COARE results underestimate the magnitude of the negative SHF. In the unstable regime, it also underestimates the magnitude of SHF. The small amount of data near the thermally neutral condition seems to compare the best. Although the general trend of the comparison for LHF seems reasonable, there is significant scattering in the scatter plot. In general, the large observed

LHF, mostly occurs in the early afternoon and tends to be overestimated by COARE, while the smaller fluxes tend to be underestimated. Future work may examine this result in a more systematic analysis.

a)

b)
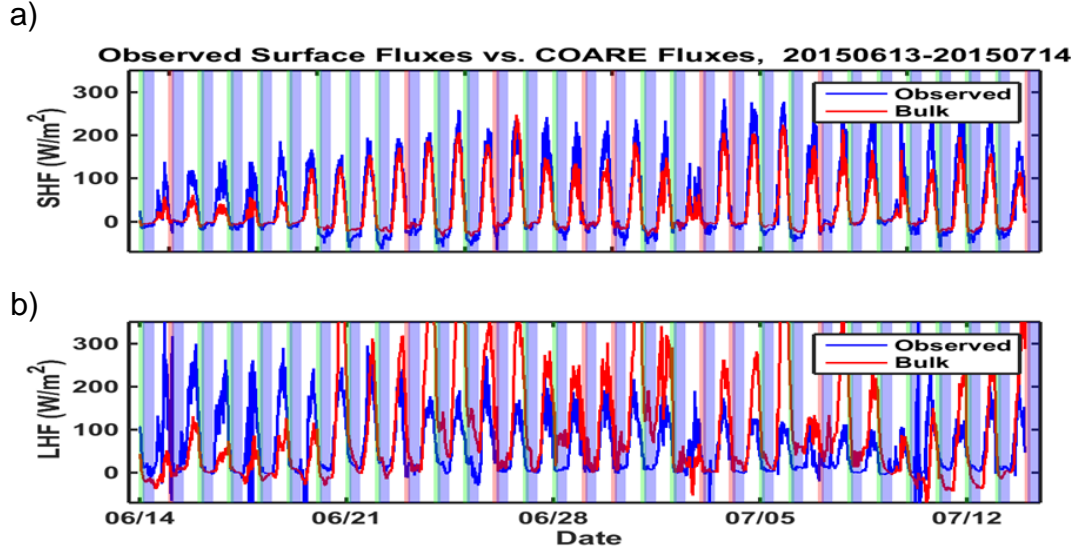
A comparison of a) sensible heat flux and b) latent heat flux evaluated against the COARE algorithm from June 14 - July 15, 2015. The solid blue line is the observed flux as measured by FP2. The red solid line is the output of the COARE algorithm. The shaded blue areas denote overnight periods; the red shaded areas are transitions on days convective events occurred, while the green shaded areas are non-convective transition time periods.

Figure 43.   Observed Surface Fluxes Evaluated Against COARE Fluxes.

Figure 43 shows the comparison of the resultant SHF and LHF in comparison with the measurement derived respective fluxes. In general, COARE SHF and LHF compare reasonably well although there is clear underestimates in the midday and night for the magnitude of the sensible heat fluxes. The latent heat flux comparison does not show constant bias. The comparisons are best seen in the scatter plots in Figure 44. The momentum flux seems to compare the best among all three fluxes where the data points are centered around the 1:1 line. The sensible heat flux shows the trend well except with a nonlinear bias. In the stable regime, COARE results underestimate the magnitude of the negative SHF. In the unstable regime, it also underestimates the magnitude of SHF. The small amount of data near the thermally neutral condition seems to compare the

74

best. Although the general trend of the comparison for LHF seems reasonable, there is significant scattering in the scatter plot. In general, the large observed LHF, mostly occurs in the early afternoon and tends to be overestimated by COARE, while the smaller fluxes tend to be underestimated. Future work may examine this result in a more systematic analysis.
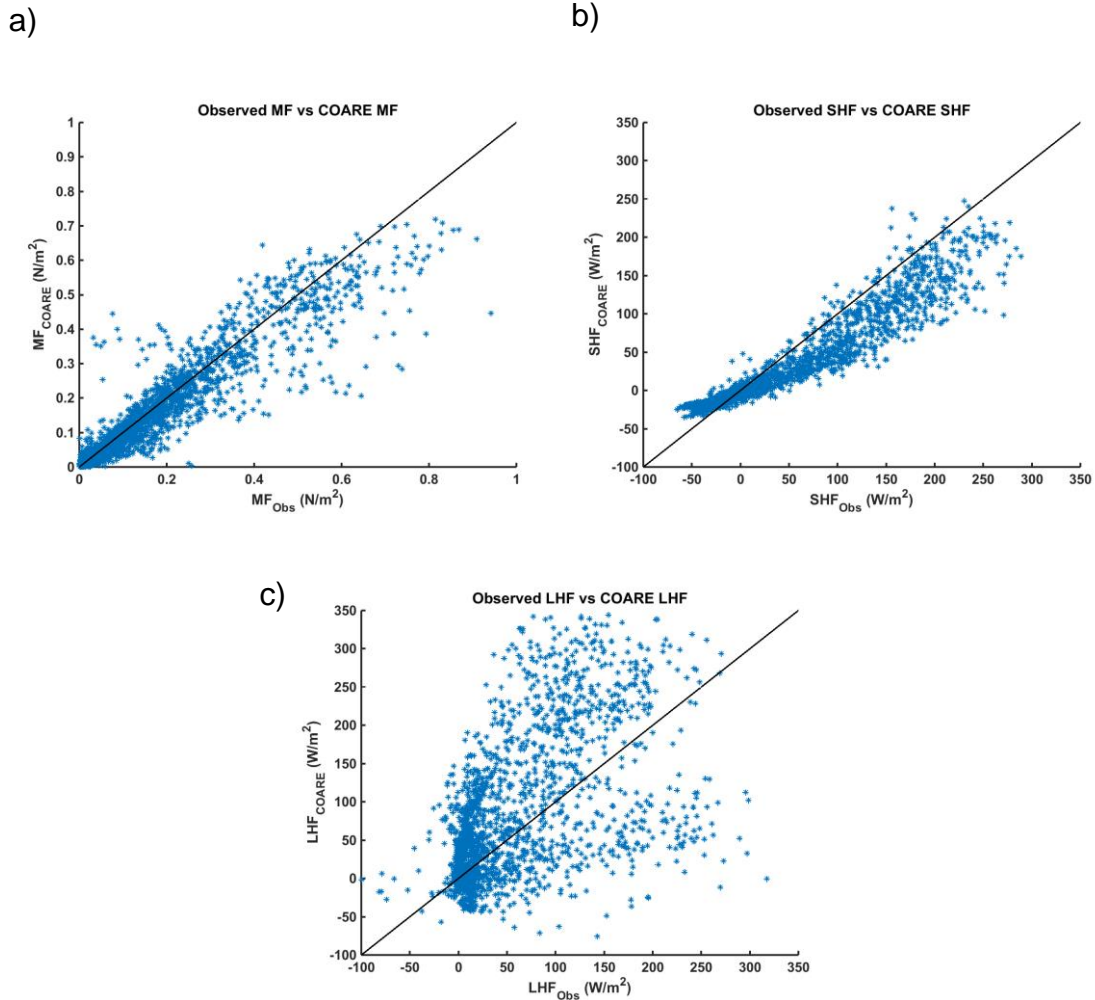
a)

b)

c)

Scatter plot evaluations of (a) momentum flux, (b) sensible heat flux and (c) latent heat flux from all cases spanning June 14 - July 15, 2015. The observed flux values are on the x-axis and the COARE algorithm on the y-axis.

Figure 44.   Scatter Plot Evaluation of COARE versus Observed Fluxes June 14 - July 15, 2015.

3.　COARE Precipitation and Cloud Comparison

An important aspect of the COARE calculations is to examine how the parametrization scheme performs during the convective events. Figure 45 shows the measured (horizontal axis) and the COARE (vertical axis) fluxes during all identified precipitation events. The perfect correlation line is drawn on the figures as well. Figure 45 shows that the magnitude of surface fluxes during the precipitation events are all rather low. In case of the momentum flux, the COARE algorithm tends to slightly underestimate in most of the cases. The comparison for both SHF and LHF seems to be consistent with those in Figure 44. No clear trend can be identified for latent heat flux
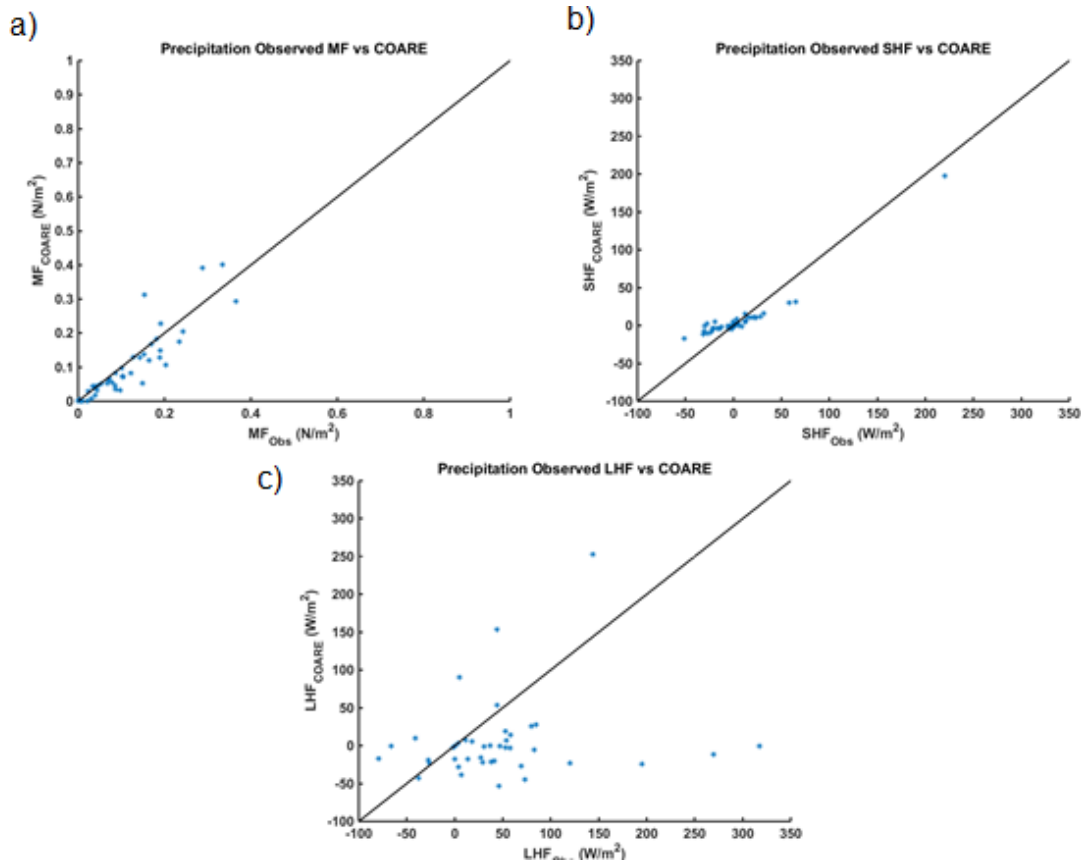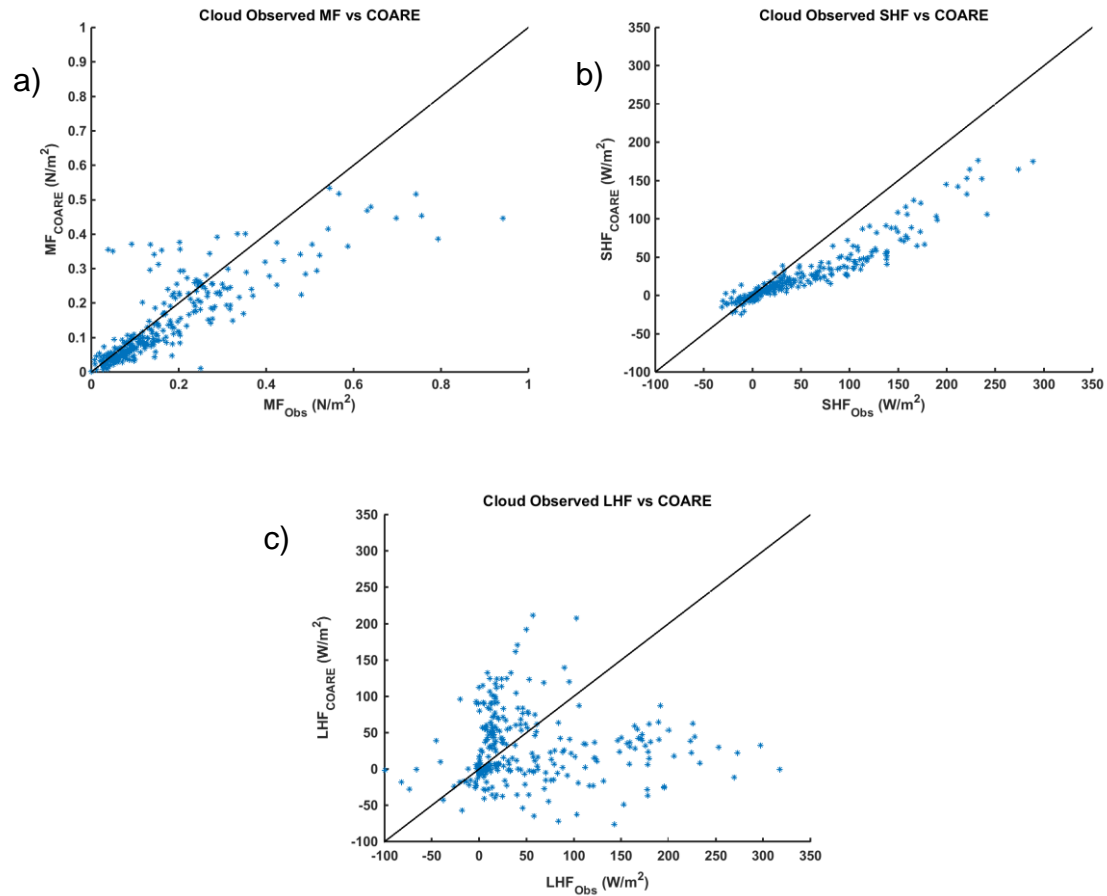

Scatter plot evaluations of (a) momentum flux, (b) sensible heat flux and (c) latent heat flux from precipitation events spanning June 14 - July 15, 2015. The observed flux values are on the x-axis and the COARE algorithm on the y-axis.

Figure 45.　Scatter Plot Evaluation of COARE versus Observed Fluxes Precipitation Events June 14 - July 15, 2015.

An important aspect of the COARE calculations is to examine how the parametrization scheme performs during the convective events. Figure 45 shows the measured (horizontal axis) and the COARE (vertical axis) fluxes during all identified precipitation events. The perfect correlation line is drawn on the figures as well. Figure 45 shows that the magnitude of surface fluxes during the precipitation events are all rather low. In case of the momentum flux, the COARE algorithm tends to slightly underestimate in most of the cases. The comparison for both SHF and LHF seems to be consistent with those in Figure 44. No clear trend can be identified for latent heat flux.

A similar comparison was also conducted with the cloud cases depicted in Figure 46. Although with more data points, similar conclusions from the previous comparison for the precipitation case can be drawn for the cloud case. The ranges of variability for the fluxes for the cloud case are much larger than those during the precipitation cases. The underestimated MF by COARE is seen for some of the larger MF. Again, COARE underestimates the magnitude of SHF in both stable and unstable conditions and the LHF comparison shows two groups as in the comparison for all LHF in Figure 44c. From these comparisons, we cannot conclude that the COARE scheme performs differently under convective conditions.

Scatter plot evaluations of (a) momentum flux, (b) sensible heat flux and (c) latent heat flux from low-cloud events spanning June 14–July 15, 2015. The observed flux values are on the x-axis and the COARE algorithm on the y-axis.

Figure 46.   Scatter Plot Evaluation of COARE versus Observed Fluxes Low-Cloud Events June 14 - July 15, 2015.

V.   SUMMARY AND CONCLUSIONS

A.   SUMMARY

This thesis work focused on the effects of convective precipitation and clouds on the afternoon-to-evening transitions (AET). Transitions under ideal conditions were first examined. The variables examined include the mean wind, temperature and moisture in the atmospheric surface layer from the tower measurements, the boundary layer wind averaged between 425 and 600 m measured from the Leosphere LIDAR, and the surface layer momentum flux, sensible heat flux and latent heat flux. The vertical profiles of boundary layer wind and vertical velocity variance and the surface layer temperature and humidity are examined together with their temporal evolution.

We selected seven precipitation events, three cloud cover events, and two events with cloud-free convective outflows as examples for detailed analyses. The direct impacts of these events on boundary layer properties were identified. Their impacts on the AET were also discussed in comparison with the ideal transition case. Table 5 summarizes the mean changes across the transition from all identified cases in each different category. In this table, the delta is defined as the measured variable at the end of the transition subtracted from its value at the beginning. Negative values reflect a decrease over the transition period.

Table 5.   Mean Changes Observed Over the Transition.

Event Type	# of occurences	ΔT	ΔRH	ΔU_{sfc}	ΔU_{427}	ΔSHF	ΔLHF	ΔMF	ΔTKE	Avg w^2	Avg SWI_{tr}	Avg SWI_{max}
Non-Convection	22	-8.75	37	-2.03	2.34	-101.23	-100.1	-0.19	-1.05	0.761	491.18	1081.09
Precipitation	7	-7.74	27.81	-1.87	-1.26	-56.85	-76.2	-0.02	-0.39	0.82	373.63	988.71
Cloud	7	-7.89	31.86	-0.9	1.23	-56.67	-97.34	-0.09	-1.01	1.5	346.77	983.29
Other	3	-9.13	23.67	-1.47	0.37	-76.67	-59.67	-0.1	-0.89	0.78	461.67	1026.33

It is recognized that the low number of occurrences for the specific convective events is not ideal for generating statistically meaningful result. However, by analyzing the average change of the different type of events through the transition, some common features can be identified. During both precipitation and cloud events, smaller decreases in temperature, wind speed, sensible heat flux, and momentum flux occurred over the transition. During precipitation events, the reduction in TKE was much smaller and there was one event that vertical velocity variance increased over the transition. Also during both events, the incoming solar irradiance was reduced both at the onset of the transition and the maximum for the day. This can be attributed to the clouds that occur during both precipitation and cloud cover events. During the low-cloud events, the transition had smaller reductions in surface wind and winds above the surface layer at 427 m above the surface, and the latent heat flux was similar to days in which there were no convective events. These average values over the transition are informative for identifying how the events impacted the transition. However, the small number of cases of the convective events makes it unfeasible to draw quantitative conclusions.

Table 6 examines how a measured variable was impacted by precipitation or clouds. Table 6 allows an overview at the convective specific events and their associated average impacts on the boundary layer. Table 6 shows that the convective precipitation and low-cloud events have many common features during the events with consistent reductions in temperature and increases in relative humidity. The reductions in sensible and latent heat fluxes and incoming solar radiation are also clear. The similarity between the two types of events is reasonable as precipitation events are always accompanied by clouds although some maybe higher than 1000 m which were not categorized as low-level clouds.

Table 6.   Mean Changes Observed Over the Convective Events.

Event Type	# of occurences	Δ T	Δ RH	Δ U$_{sfc}$	Δ U$_{427}$	Δ SHF	Δ LHF	Δ MF	Δ TKE	Δ w^2	Δ SWI
Precipitation	9	-6.48	20.61	-0.94	-2.06	-35.34	-25.88	-0.09	-0.21	0.1	-117.9
Cloud	7	-1.49	5.75	0.6	1.26	-30.61	-34.65	0.02	0.09	-0.67	-209.2
Other	3	-0.7	-1	0	2.05	-90.5	-27.5	-0.08	-0.34	-1.19	-260.5

The values in this table show the mean difference in the corresponding variable before and after each event (x_{after}-x_{before}, x being the variable in consideration).

Temperature reduction that is observed in the precipitation events is much more pronounced than the low-cloud events. This is considered reasonable due to the additional cooling by evaporation of rain. The dynamic features shows large variations and render no consistent results in surface layer and boundary layer winds, momentum flux, vertical velocity variance, and TKE. These variables are largely affected by the proximity to the storm center and the outflow boundaries and there are significant variabilities within the storm as well. For the same reason, the last category of events (other) shows different characteristics from the previous two and is less consistent within themselves. Again, as in Table 5, the results in this table should be examined qualitatively due to the small number of samples involved. In order to further draw any solid conclusions, an expanded data set and more cases will need to be analyzed. This, however, is outside the scope of this thesis.

As discussed in the results chapter, the COARE algorithm, modified for land surface application, was used to generate surface fluxes and compared to the observed fluxes collected during PECAN. Figure 47 give the difference between the two during the entire PECAN period (F_{obs}-F_{COARE}). The positive values represent areas where the algorithm underestimated the flux and vice versa. We found that the climatological value surface roughness used in COAMPS significantly overestimated the surface roughness (0.05 m vs 0.25 m) for the June/July season. Subsequent calculation using COARE were derived using the adjusted z_0. The comparison in Figure 47 thus shows the difference as a result of thermal stability function or residual bias/errors in the mean variables

as input to the COARE algorithm. A consistent feature present in all three fluxes is that the parametrization scheme overall performed much better at night as seen with the values closer to zero in the blue shaded regions in Figure 47. This result is, however, in some way misleading because the small magnitude of fluxes at night. The relative error can be significantly large. Figure 47 shows that the COARE consistently underestimates the magnitude sensible heat flux at night and during the day. The COARE estimates of the LHF varied. Where we see a general underestimate in the early part of June and overestimate for the later days. These discrepancies seem to indicate issues in the input parameters rather than the COARE stability functions. There are multiple ways to select the input of skin temperature and soil moisture content, all yield different results in the resultant LHF. This thesis provides and initial analyses of this issue. More in-depth analyses should follow to clearly identify the cause of these different discrepancies.

Observed - COARE Fluxes
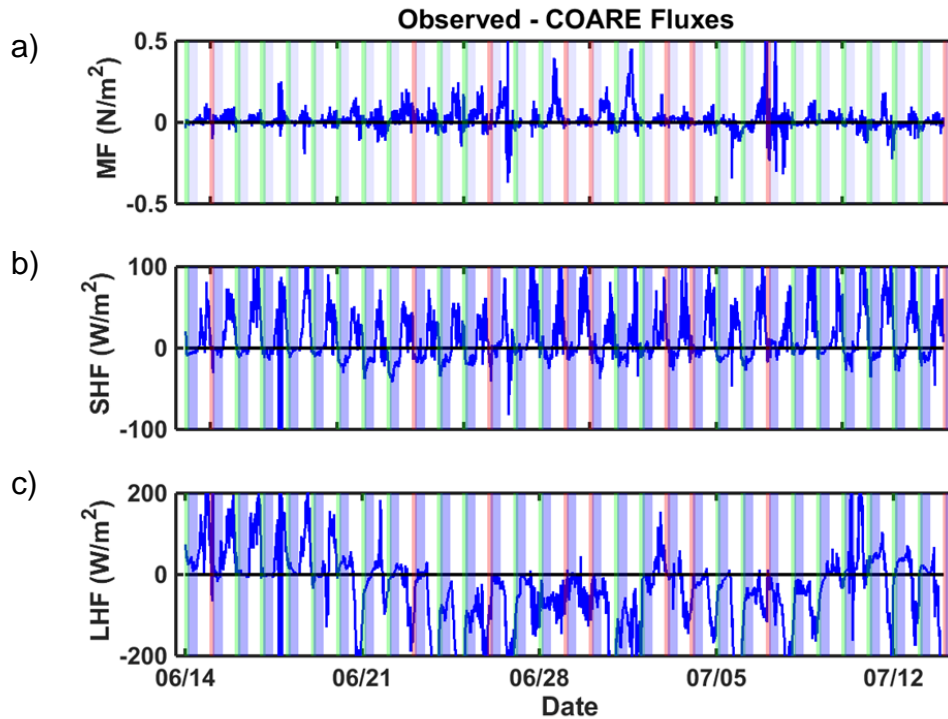
The observed surface fluxes a) momentum flux, b) sensible heat flux , and c) latent heat flux is subtracted from the COARE algorithm flux. The result is the solid blue line. The blue shaded areas are the overnight time periods, the red shaded areas are transitions in which a convective event occurred and green shaded areas are non-convective transitions.

Figure 47.   Difference in Observed Flux and COARE Algorithm.

B.   CONCLUSIONS

In summary, convective precipitation events that were examined during this thesis shared some common features, which impacted the AET. These common features included a pronounced decrease in temperature, sensible heat and latent heat fluxes, TKE, momentum flux and winds and there are increases in relative humidity after the transition. These common features occurred during the time period the precipitation also occurred. The effect on the transition is less apparent when comparing to the non-event days.

Consistent with multiple studies done in the previous research, low-level clouds prevent a clear defined AET from occurring. This is likely due to multiple physical factors that occur during this scenario. The clouds act as blanket over

the surface and modify the surface energy budget, which reduces the cooling at night compared to the ideal transition cases. Present during the cloud cases also was the change in near surface moisture. With near surface moisture remaining relatively constant on cloud cover days, the expected daytime peaks in sensible and latent heat flux were not apparent.

This thesis also examined 2 cases that involved passing of cloud-free dynamic boundaries associated with nearby storms. While one of these boundaries was convective in nature, and the other was more synoptic, both affected the AET in ways that differed from an ideal transition scenario. Common features between the two included both a spike and shift in the winds. Both events included an increase in TKE associated with the passage; however, the synoptic event had a deeper layer of wind shear, which contributed to a slightly larger increase in TKE. This increase in TKE is not expected during ideal transitions. Consistent with both boundary passages, temperature and specific humidity were affected. With the temperature, the expected rapid decay through the transition did not happen. With the specific humidity on non-convective cases, there is a consistent increase right before sunset. This feature is also present with both boundary cases this thesis examined.

LIST OF REFERENCES

Acevedo, O. C., and D. R. Fitzjarrald, 2001: The Early Evening Surface-Layer Transition: Temporal and Spatial Variability. *J Atmos Science*, 58, 2650–2667.

Atmospheric System Corporation, 2016. Atmospheric System Corporation--Setting the Standard in SODARs. Accessed 15 August 2016.[Available online at http://www.minisodar.com/sodar/.]

Beare, R. J., J. M. Edwards, and A. J. Lapworth, 2006: Simulation of the observed evening transition and nocturnal boundary layers: Large-eddy simulation. *Q J R Meteorol Soc, 132,* 81–99.

Bodine, D., P. M. Klein, S. C. Arms, and A. Shapiro, 2009: Variability of Surface Air Temperature over Gently Sloped Terrain. *J Appl Meteorol Climatol*, 48, 1117–1141.

Bonin, T., P. Chilson, B. Zielke, and E. Fedorovich, 2012: Observations of the Early Evening Boundary-Layer Transition Using a Small Unmanned Aerial System. *Boundary-Layer Meteorolo*, 146, 119–132.

Boutle, I. A., R. J. Beare, S. E. Belcher, A. R. Brown, and R. S. Plant, 2009: The Moist Boundary Layer under a Mid-latitude Weather System. *Boundary-Layer Meteorolo*, 134, 367–386.

Busse, J., and K. Knupp, 2012: Observed Characteristics of the Afternoon–Evening Boundary Layer Transition Based on Sodar and Surface Data. *J Appl Meteorol Climatol*, 51, 571–582.

Caughey, S. J., J. C. Wyngaard, and J. C. Kaimal, 1979: Turbulence in the Evolving Stable Boundary Layer. *J Atmos Science, 36,* 1041–1052.

Fairall, C.W., E.F. Bradley, D.P. Rogers, J.B. Edson, G.S. Young, 1996: Bulk Parameterization of Air-Sea Fluxes for TOGA COARE. *J. Geophys. Res.* 101, 3747–3764.

Fairall, C.W., E.F. Bradley, J.E. Hare, A.A. Grachev, J.B. Edson, 2003. Bulk Parameterization of Air–Sea Fluxes: Updates and Verification for the COARE Algorithm. *J Climate, 16, 571–591.*

Garratt, J. R., 1992: The atmospheric boundary layer. *The atmospheric boundary layer*, Cambridge University Press, Cambridge, p. 316.

Grant, A., 1997: An observational study of the evening transition boundary-layer. *Q J R Meteorol Soc*, 123, 657–677.

Grimsdell, A. W., and W. M. Angevine, 2002: Observations of the Afternoon Transition of the Convective Boundary Layer. *J Appl Meteorol*, 41, 3–11.

Kessler, E., 1986: Thunderstorm morphology and dynamics. *Thunderstorm morphology and dynamics*, University of Oklahoma Press, Norman, 81–86.

Lothon, M., and Coauthors, 2014: The BLLAST field experiment: Boundary-Layer Late Afternoon and Sunset Turbulence. *Atmos. Chem. Phys. Discuss.*, 14, 10789–10852.

Mahrt, L., 1981: The early evening boundary layer transition. *Q J R Meteorol Soc*, 107, 329–343.

National Severe Storms Laboratory, 2015. NSSL PECAN 2015 Fact Sheet. Accessed 1 June 2015. [Available online at http://www.nssl.noaa.gov/news/factsheets/PECAN_2015_NSSL_FINAL.pdf]

Stull, R. B., 1988: An introduction to boundary layer meteorology. *An introduction to boundary layer meteorology*, Kluwer Academic Publishers, Dordrecht, p. 666.

Vaisala, 2015. CL31-Datasheet-B210415EN. Accessed 16 August 2016. [Available online at http://www.vaisala.com/Vaisala%20Documents/Brochures%20and%20Datasheets/CL31-Datasheet-B210415EN.pdf]

Wingo, S. M., and K. R. Knupp, 2014: Multi-platform Observations Characterizing the Afternoon-to-Evening Transition of the Planetary Boundary Layer in Northern Alabama, USA. *Boundary-Layer Meteorolo*, 155, 29–53.

INITIAL DISTRIBUTION LIST

1.	Defense Technical Information Center
	Ft. Belvoir, Virginia

2.	Dudley Knox Library
	Naval Postgraduate School
	Monterey, California